Timber joinery in modern construction: Mechanical behavior of wood-wood connections

By

Demi L. Fang

Bachelor of Science in Engineering, Civil and Environmental Engineering
Princeton University, 2017

Submitted to the
Department of Architecture
in Partial Fulfillment of the Requirements for the Degree of

Master of Science in Building Technology

at the

Massachusetts Institute of Technology

May 2020

Signature of Author: _____
Department of Architecture
08 May 2020

Certified by: _____
Caitlin Mueller
Associate Professor, Departments of Architecture and Civil and Environmental Engineering
Thesis Supervisor

Accepted by: _____
Leslie K. Norford
Chair, Department Committee on Graduate Students

Timber joinery in modern construction: Mechanical behavior of wood-wood connections

By

Demi L. Fang

Submitted to the Department of Architecture on May 8, 2020
in Partial Fulfillment of the Requirements for the Degree of
Master of Science in Building Technology

Abstract

Timber joinery is a method of geometrically interlocking timber elements prevalent in historic cultures around the world, including North America, Europe, and East Asia. The use of joinery as structural connections faded with the development of metallic screws and nails. Two recent developments offer the opportunity to revive this historic timber connection type: 1) the increasing desire to reduce embodied carbon in buildings by replacing more components with timber as a low-carbon structural material, and 2) recent digital fabrication capabilities which enable the precise milling of complex geometries as an alternative to the time- and labor-intensive handiwork required previously.

How can joinery connections be designed in modern structural joints? Can we quantify the sustainability advantage of using these all-timber joints in lieu of the modern convention of metallic fasteners? This thesis addresses both questions as applied to the Japanese Nuki joinery type, though the workflows may be applied to any joinery geometry. First, the rotational stiffness of the Nuki joint is characterized and cross-verified using multiple methods. Second, the embodied carbon of a gravity frame using Nuki joints is compared to that of a gravity frame using conventional metallic fasteners. The use of Nuki joints not only eliminates the use of steel and aluminum but also provides rotational stiffnesses that enable smaller beam sections to be used. It is shown that gravity frames designed with Nuki joints could reduce embodied carbon by over 70% compared to gravity frames designed using conventional beam hanger connections. The findings make a case for all-timber joinery connections to be implemented as a sustainable alternative to conventional metallic connections used in modern timber construction.

Thesis Supervisor: Caitlin Mueller

Associate Professor, Departments of Architecture and Civil and Environmental Engineering

Acknowledgements

I have to begin by expressing my utmost gratitude to my adviser Prof. Caitlin Mueller for her outstanding mentorship in all these years I have been fortunate to work with her. Thank you for being endlessly supportive of my professional growth and ambitions and for always trusting in my potential as a researcher. I very much look forward to continuing to work with you in the next few years!

Much of this research could not have been possible without my collaborators for the mechanical analyses of the Nuki joint. A fortuitous encounter at IASS 2018 led to a rich collaboration with Julieta Moradei, Aliz Fischer, Nick Sherrow-Groves, and Dr. Benshun Shao at Arup San Francisco; as well as Jan Brütting and Prof. Corentin Fivet at the Structural Xploration Lab of EPFL. I thank and applaud Danny Landez, our undergraduate research assistant funded by the MIT UROP, for independently carrying out experiments during my gap year.

I am thankful to Dr. Ben Brungraber for early discussions on the topic of analyzing timber frames, as well as to Andrew Dey at Unity Homes and Tedd Benson at Bensonwood for their hospitality in showing us their facilities. Many thanks go to Nordic Structures (in particular Jean-Luc Dubois) and Bensonwood for coordinating to provide us glulam offcuts for our prototypes. Our prototypes were fabricated in the MIT N51 wood shop (thank you, Chris Dewart) and the Autodesk BUILD Space in Boston, and then tested in the Course 1 load-testing labs (thank you, Steve Rudolph). In Course 1, I additionally thank Prof. Tal Cohen for supervising my research on the dynamics of joinery connections in historic structures, as well as Prof. Josephine Carstensen for early discussions on possible applications of level-set topology optimization. I also appreciate interesting early discussions and insights shared by Dr. Felix Amtsberg.

I primarily want to thank my colleague Dr. Paul Mayencourt for sharing camaraderie, valuable engineering insights, and an enthusiasm for timber and its craft with me throughout the past three years. I am also grateful for MIT Architecture's furniture class with Chris Dewart and joinery workshops with the Suikoushya school (Kawai-sensei and Dylan Iwakuni, whose visits in early 2020 were sponsored by MISTI Japan) which have introduced me to the beauty of joinery craftsmanship.

I deeply thank Meredith and Ray Rothrock for their warm support of my endeavors during our work on the greenhouse in 2018. I am also thankful to my teammates and mentors at SOM Chicago, who graciously hosted me for a fruitful gap year internship in 2019. The opportunity to immerse in a vibrant environment of multidisciplinary design in the applied field helped me incubate several ideas that emerged in this thesis.

During both joyful and difficult times at MIT, but especially during this global pandemic, I am thankful for my support networks at MIT, in the Cambridge area, and beyond. My most heartfelt gratitude goes out to my family: to soon-to-be Dr. Billy Fang for always serving as an outstanding role model to me, and to Mom and Dad for their generous and unwavering support of my growth and abilities.

Finally, I am very grateful that my research at MIT was made possible by the MIT Presidential Graduate Fellowship and SA+P's J. A. Curtis (1953) Fund.

Table of Contents

Publications and presentations related to thesis

Fang, Demi, and Caitlin Mueller. 2018. "Joinery Connections in Timber Frames: Analytical and Experimental Explorations of Structural Behavior." In *Proceedings of the International Association for Shell and Spatial Structures (IASS) Symposium*. Cambridge, MA, USA.

Fang, Demi, Caitlin Mueller, Jan Brütting, Corentin Fivet, and Julieta Moradei. 2019. "Rotational Stiffness in Timber Joinery Connections: Analytical and Experimental Characterizations of the Nuki Joint." In *Structures and Architecture: Bridging the Gap and Crossing Borders*, edited by Paulo J.S. Cruz, 229–36. Lisbon, Portugal: CRC Press. https://doi.org/10.1201/9781315229126-28.

Fang, Demi, Julieta Moradei, Jan Brütting, Aliz Fischer, Daniel K Landez, Benshun Shao, Nick Sherrow-Groves, Corentin Fivet, and Caitlin Mueller. 2019. "Modern Timber Design Approaches for Traditional Japanese Architecture: Analytical, Experimental, and Numerical Approaches for the Nuki Joint." In *Proceedings of the International Association for Shell and Spatial Structures (IASS) Symposium*. Barcelona, Spain.

Fang, Demi, Alpha Arsano, Nathan Brown, Christoph Reinhart, and Caitlin Mueller. 2019. "Design Space Exploration for High-Performance Greenhouse Design." In *Proceedings of the International Association for Shell and Spatial Structures (IASS) Symposium*. Barcelona, Spain.

List of mathematical symbols

b	beam width (Section 5)
B_d	beam depth (Sections 3 and 4)
B_w	beam width (Sections 3 and 4)
C_d	column depth
C_w	column width
d	diameter
Δ	linear displacement
E_0	elastic modulus of a timber material parallel to grain
E_{90}	elastic modulus of a timber material perpendicular to grain
ε_y	yield strain for a timber material under compression perpendicular to grain
h	beam depth (Section 5)
I	area moment of inertia
k	rotational stiffness of joint
l	various embedment lengths
L	various lengths (Sections 3 and 4, Appendix 1); beam span (Section 5, Appendix 3)
μ	coefficient of static friction
$M(x)$	bending moment along beam's long axis x
M_{allow}	allowable moment
M_y	yield moment
N	normal contact force
PR_{90}	stiffness plastic reduction factor for compression perpendicular to grain
q	applied line load
σ	bending stress
τ	shear stress
θ	angular displacement
$V(x)$	shear of beam along beam's long axis x
$w(x)$	deflection of beam perpendicular to long axis x
Z	depth of material experiencing embedment
Z_0	initial depth of material experiencing embedment

List of figures

List of tables

1 Introduction

1.1 Motivation

In a rapidly urbanizing world where buildings contribute to 40% of global carbon emissions, structural designers are becoming increasingly conscientious of their roles and responsibilities in the profession (International Energy Agency (IEA) and Global Alliance for Buildings and Construction (GlobalABC) 2018). These responsibilities are acknowledged by professional organizations who have challenged designers to reduce and eventually eliminate embodied carbon by 2050 ("Structural Engineers 2050 Challenge" n.d.) or even 2030 ("Architecture 2030" n.d.).

One major strategy for reducing embodied carbon in buildings is to select structural materials with lower embodied carbon. As a result, structural timber is witnessing a recent revival in modern construction. "Mass timber" is the term used for engineered wood products, glued-up pieces of small timber, that have recently enabled large construction with embodied carbon at a fraction of that of a concrete or steel building of the same scale.

Because most mass timber elements, like cross-laminated timber (CLT) and glue-laminated timber (glulam), are standardized linear or planar elements, one trend in the mass timber

movement is the use of metallic fasteners to connect timber elements. These range from nails and screws to connection systems with more components and bearing plates (Figure 1, Figure 2, Figure 3, Figure 4, Figure 5).

Figure 1. Steel connections between glulam elements at the Bullitt Center (Miller Hull Partnership; Seattle, WA, USA; 2013). Left: during construction (Court 2012), photo by John Stamets; right: interior after completion (Schuchart n.d.).

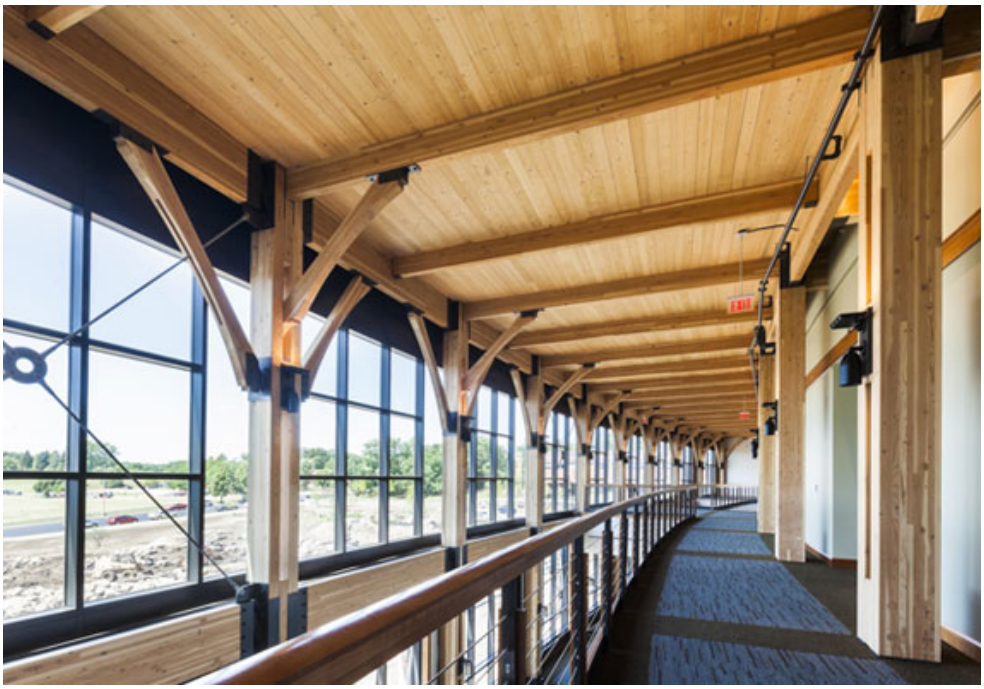

Figure 2. Interior of the Promega Feynman Center "The Crossroads" manufacturing facility (Uihlein-Wilson Architects, Inc.; Madison, WI, USA; 2013). (WoodWorks n.d.)

Figure 3. Structural connection detail at T3 (Michael Green Architecture and DLR Group; Minneapolis, MN, USA; 2016). (Brownell 2016)

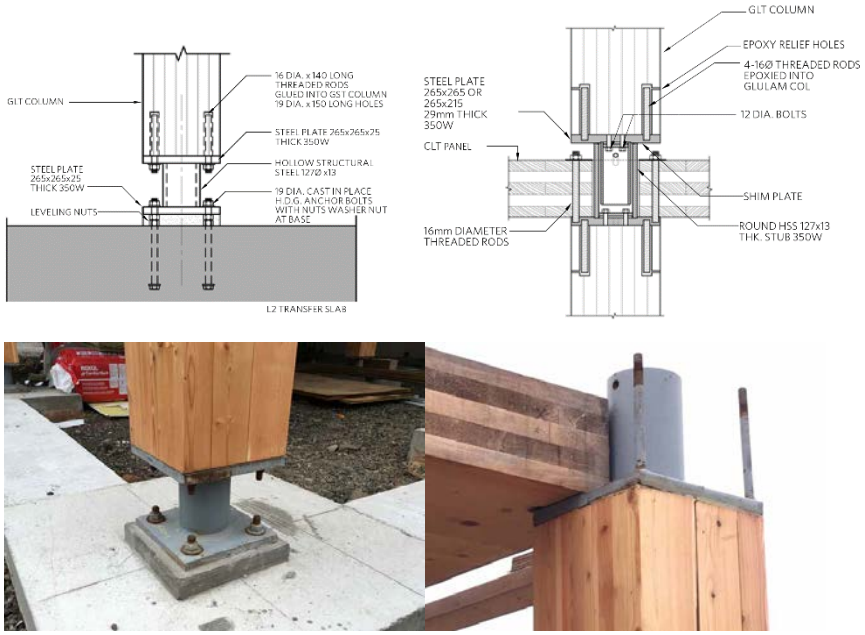

Figure 4. Structural detailing of the Brock Commons Tallwood House (Acton Ostry Architects; Vancouver, BC, Canada; 2017) at University of British Columbia. (naturally:wood 2016)

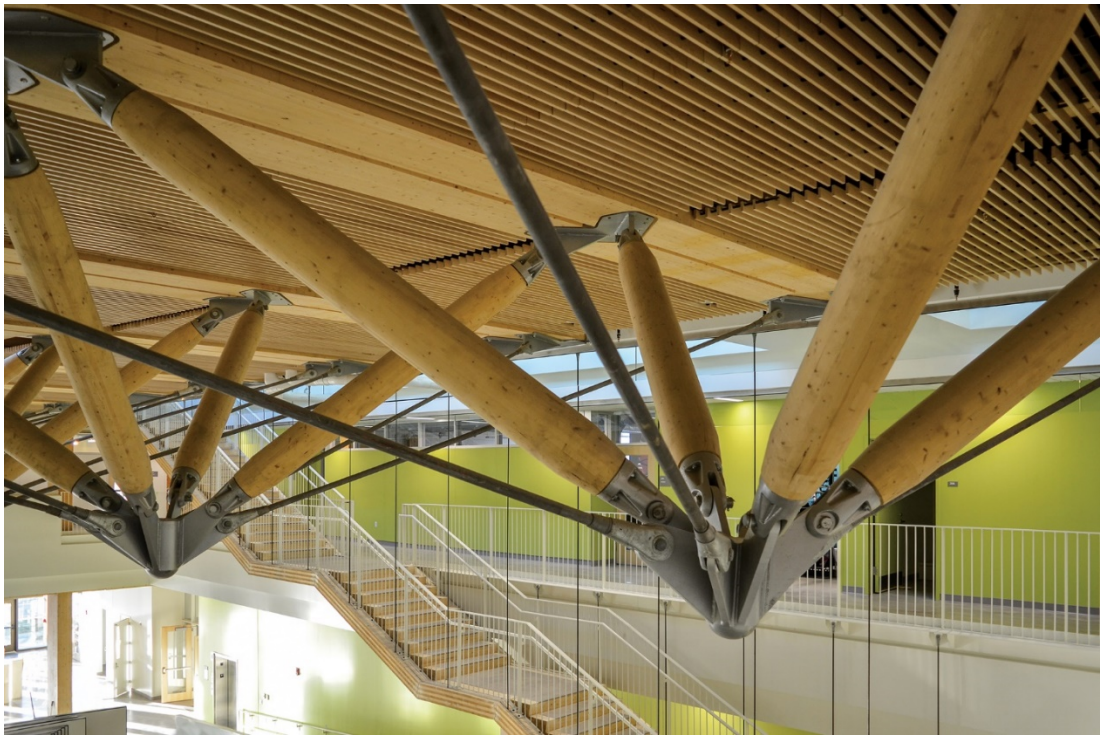

Figure 5. Connection details of zipper trusses at the John W. Olver Design Building (Leers Weinzapfel Associates; Amherst, MA, USA; 2017) at University of Massachusetts Amherst. (Miller 2017)

Even visually, these metallic connection components stand out, seemingly in contrast with the original motivations of using timber as a more sustainable structural material. Their modern-day use may have evolved out of both practicality and evolution of the screws and nails used in light-frame timber construction. However, even before the invention of screws and nails, historic timber construction across the world made use of joinery, or geometrically interlocking timber joints.

1.2 Timber joinery in history

Joinery has been known to be implemented in historic timber construction in East Asia (Figure 6 and Figure 7), North America (Figure 9 and Figure 10), present-day United Kingdom (Figure 8), Europe, and Egypt (Foliente 2000; Zwerger 2015).

Figure 6. Bracket set joinery at Nandaimon, or the Great South Gate (Nara, Japan; 12th century) of Todai-ji. Photo by Deanna MacDonald.

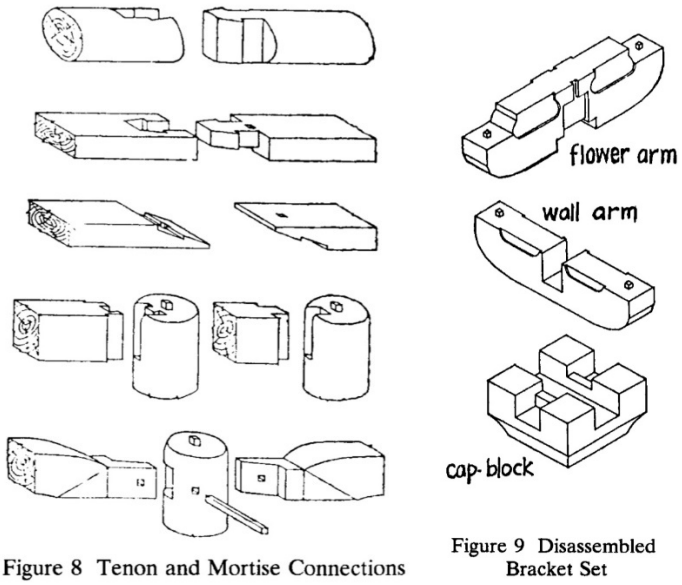

Figure 7. Joinery types in Chinese traditional timber architecture. (Shiping 1991)

Figure 8. Cruck framing, an English carpentry technique. Leigh Court Barn is the largest cruck framed structure in Britain (Worcester, England; 1325). Photo by Simon Webb.

Figure 9. A modern example of North American timber framing tradition. Photo by Vermont Timber Works Inc.

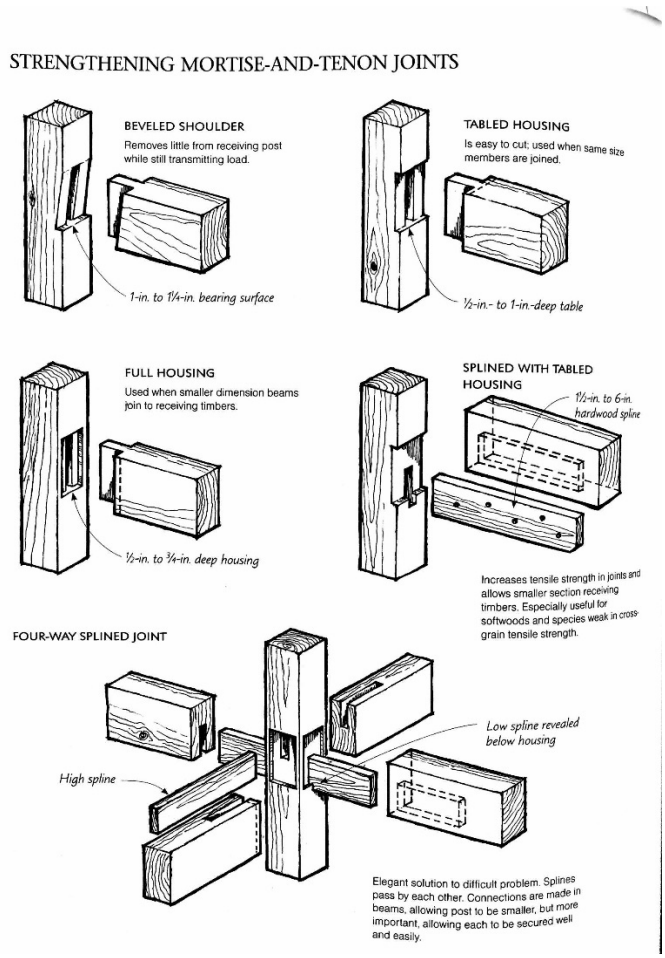

Figure 10. Example joinery from the North American timber framing tradition. (Benson 1997)

Japan's tradition of timber construction is particularly known for combining timber joinery with a "design for deconstruction" approach that enabled structures like the Ise Jingu Shrine (4 BC) to be rebuilt every 20 years as part of Shinto belief in death and renewal (Henrichsen and Bauer 2004).

1.3 Timber joinery in modern structures

As much as joinery was prevalent in historic construction, it is relatively rare in modern timber construction. With its absence in building code, it only appears in relatively boutique architectural structures. Some of these deliberately showcase and celebrate the use of the joinery (Figure 11, Figure 12, Figure 13), while others are deliberate revivals of the historic timber framing tradition at the residential scale (Figure 14).

Figure 11. Joinery detail at the Yusuhara Wooden Bridge Museum (Kengo Kuma & Associates; Yusuhara, Japan; 2011). Photo by Takumi Ota.

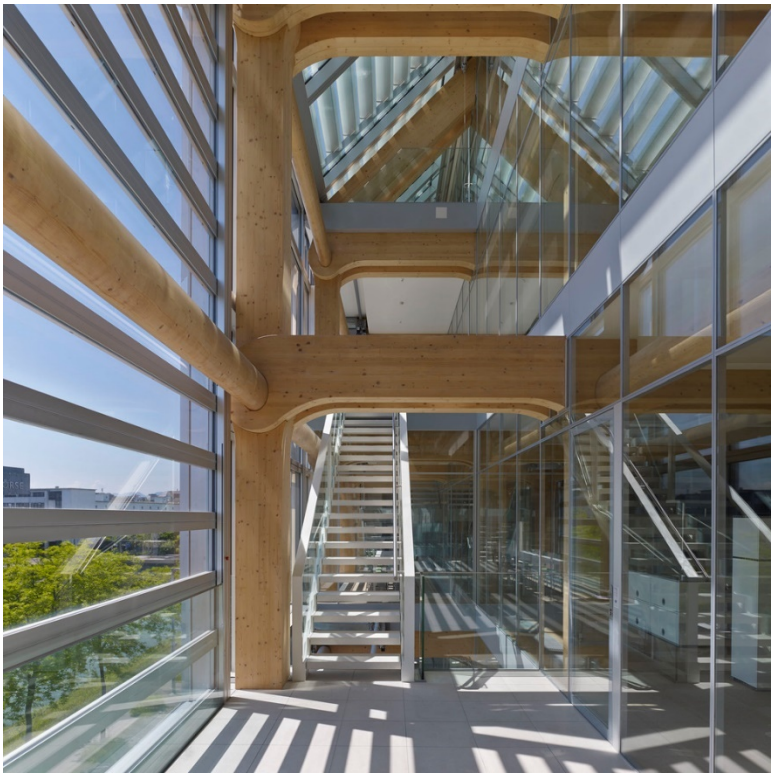

Figure 12. All-timber structural system of the Tamedia Office Building (Shigeru Ban Architects; Zurich, Switzerland; 2013). Photo by Didier Boy de la Tour.

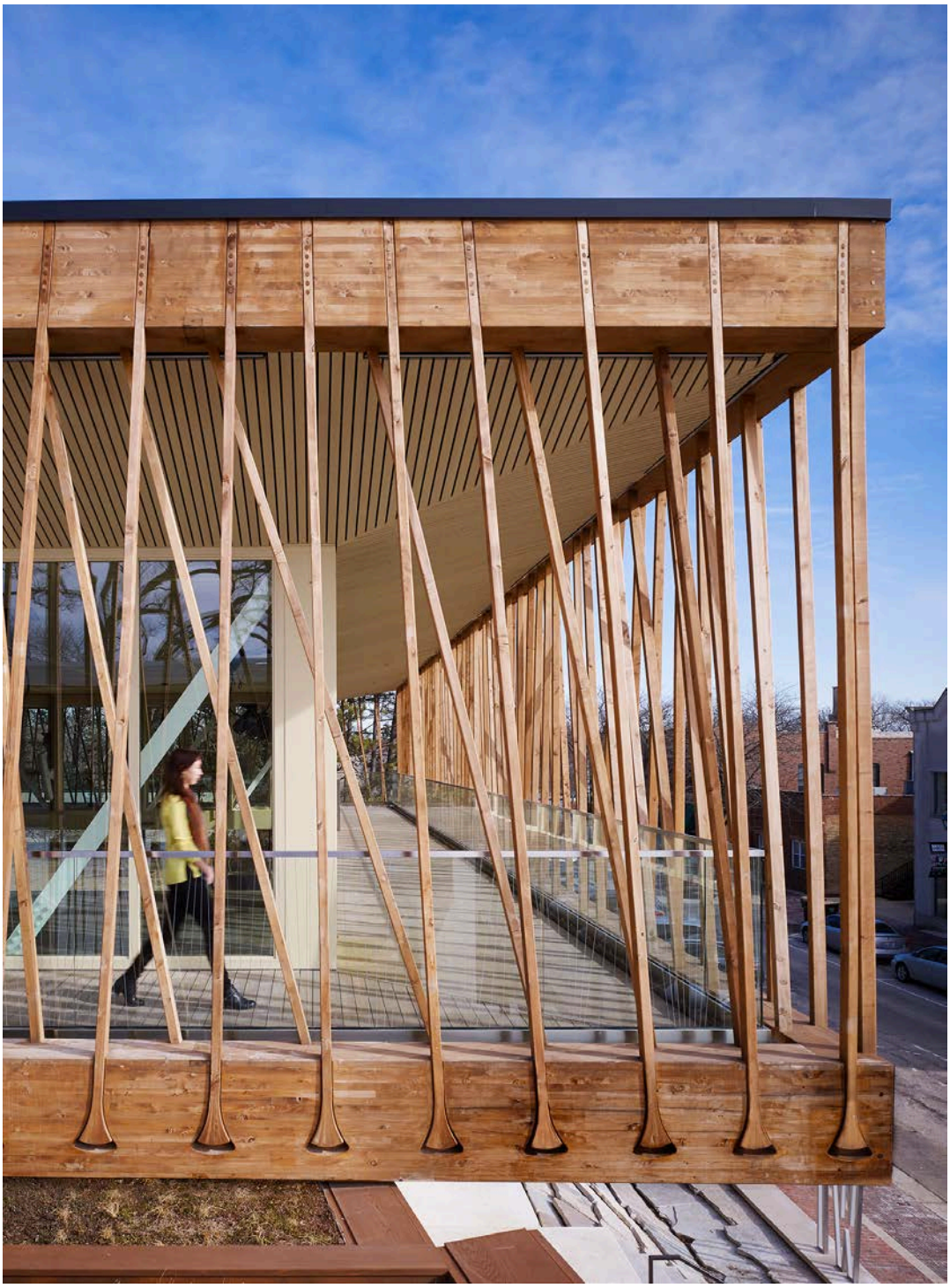

Figure 13. "Cat's paw" timber tension joinery detail at the Writers Theatre (Studio Gang; Glencoe, IL, USA; 2016). Photo by Steve Hall © Hedrich Blessing.

Figure 14. Timber construction companies like Bensonwood create modern homes, like this Vermont lake house (Ludlow, VT, USA; 2008) in the traditional style of North American timber framing. Photo by Al Karevy.

The historic transition from joinery to fasteners arose out of the efficiency afforded by fasteners to join standardized timber elements, compared to the time and labor required to carve joinery geometries out of each timber element. However, as the above projects demonstrate, the advancing role of digital fabrication in modern construction may tip the scale.

1.4 Potential benefits and opportunities

Introducing joinery into modern timber construction offers several benefits and opportunities. A few are listed below, although not all are explored in this thesis.

1.4.1 Non-destructive assembly and Design for Deconstruction

The Ise Jingu Shrine establishes a historic precedent for using joinery for a Design for Deconstruction (DfD) approach, a sustainable approach that extends the longevity of structures. Though not explicitly addressed in this thesis, there is potential for the modern-day use of joinery to reinvigorate aspects of DfD.

Admittedly, metallic fasteners that are conventionally used with timber elements in construction systems of all scales may already be deconstruction-friendly, so the relative ease for DfD of joinery connections should be evaluated.

The potential for joinery to be applied to DfD is related to its characteristic of non-destructive assembly, which is not commonly seen in the construction industry. The logic of non-destructive assembly is more frequently celebrated in products like furniture (Figure 15). On its product page, "The Bed" from Thuma lists several marketable advantages of their product: that the Japanese-

joinery-inspired design is "timeless, naturally noise-minimizing and easy to put together, while eliminating the need for excess metal hardware." Its speed of assembly is also highlighted.

Figure 15. "The Bed" from Thuma is marketed for its ease of assembly marked by an absence of metal hardware. ("The Bed" n.d.)

1.4.2 Seismic systems

Many have observed the resilience of historic East Asian timber structures to major seismic events. The structures' resilience can be broadly attributed to a combination of factors: 1) the redundancy offered by the structural configuration of stacking of multiple timber elements, 2) the energy dissipation enabled by the plastic crushing of wood fibers that gives "softness" to the global structure, and 3) the ability to replace damaged elements. While the potential for joinery in modern-day seismic systems is not explicitly addressed in this thesis, a literature review of modern analyses is provided in Section 2.2.

1.4.3 Reduced embodied carbon

By now, the sustainability benefits of timber as a structural material over conventional materials like steel and concrete are well established (Gustavsson, Pingoud, and Sathre 2006; Lenzen and Treloar 2002; Sathre and O'Connor 2010). Comparative studies like Stern 2018 account for the tradeoff between embodied carbon and material strength by selecting timber over steel in planar trusses. However, those tradeoffs have been studied on the structural design and quantification of primary elements (truss elements) rather than their connections. Extending this tradeoff analysis into the design of connection components has the potential to make the sustainability

evaluations of structural systems even more holistic. In this thesis, one such tradeoff analysis that accounts for connection components is presented in Section 5.

1.4.4 Biophilia

Biophilic design recognizes the benefits of human connection with nature. The exposure of natural materials, such as timber, in the interior of architectural spaces constitutes one attribute of biophilic design called "indirect experience of nature" (Kellert and Calabrese 2015). These visual connections can reduce stress, improve cognitive performance, and boost moods in humans working or living within those spaces (Browning, Ryan, and Clancy 2014). Depending on the structural system, the visual effect of metallic connection details can be prominent in timber structural systems (Figure 1, Figure 2, Figure 3, Figure 4, Figure 5). The principles of biophilic design suggest that single-material timber systems (such as those depicted in Figure 11, Figure 12, Figure 13, and Figure 14) may offer a physiological benefit to inhabitants.

1.4.5 Digital fabrication

The mass timber construction industry enables more pre-fabricated elements, which has also provided more opportunities for digital fabrication than traditionally used in the construction industry. Custom CNC millwork can be done at minimal additional cost, ranging from duct openings in CLT panels to milling mortises for joinery components, as modern-day timber framing companies like Bensonwood have done. These technologies can additionally be combined with other techniques like curved lamination or selective layups, challenging the conventional standardization of rectilinear elements and offering new ways to achieve material and structural efficiency. The comparative study presented in Section 5 envisions the potential of combining these digital fabrication techniques to enable low-carbon structural systems.

1.5 Thesis aims

This thesis aims to investigate the feasibility of re-introducing timber joinery into large-scale modern timber construction. How can their performance be quantified as structural joints? Can they provide adequate structural rigidity and softness by design at the appropriate scales in structural systems? Are there significant benefits in embodied carbon by using joinery connections instead of conventional metallic connections? After a review of relevant literature, a set of original contributions are set forth in this thesis to begin answering these questions.

2 Literature review

In this section, an overview of existing literature on the analysis of joinery connections in structural systems is presented.

2.1 Static analysis

Previous studies have sought to characterize the behavior of timber joinery connections under static load. Most methods can be classified under analytical, experimental, or numerical methods. *Analytical methods* use wood mechanics to develop models with parameters to calculate rotational stiffness of joinery connections. *Experimental methods* involve the creation of prototypes and recording their performance under applied static loads. *Numerical methods* involve the development of finite element analyses (FEA) where material properties and geometries are input to computationally simulate the behavior of the joinery connection. Most existing studies report and compare findings from at least two methods on a single joint type. A summary of the existing literature is provided in Table 1.

Table 1. Chronological overview of methods used in literature characterizing analysis and behavior of joinery connections under static load. Shaded cells indicate strength characterization; unshaded cells indicate stiffness characterization.

	Joint type	Analytical	Experimental	Numerical
(Brungraber 1985)	Pegged mortise-and-tenon, and full-size knee-braced timber bent frames	X	X	X
(Inayama 1991) (in Japanese)	None (theory of embedment)	X	X	-
(Schmidt and Mackay 1997)	Pegged mortise-and-tenon	X	X	-
(Erdil, Kasal, and Eckelman 2005)	Mortise and tenon (furniture scale)	X	X	-
(Erikson 2003)	Pegged mortise-and-tenon in knee-braced frames	-	X	X
(Chang, Hsu, and Komatsu 2006)	Continuous Nuki joint	X	X	-
(Chang and Hsu 2007)	Continuous Nuki joint, butted Nuki joint	X	X	-
(Lang and Fodor 2007)	Notched beams	-	X	X
(Guan, Kitamori, and Komatsu 2008)	*Nuki*: beam through column with wedges	-	X	X
(Shanks and Walker 2009)	Pegged mortise-and-tenon	X	X	X
(Kitamori, Kataoka, and Komatsu 2009) (in Japanese)	None (theory of embedment)	X	X	X
(Komatsu et al. 2009)	*Nuki:* beam through column, and mortise-and-tenon	X	-*	-*
(Sebera and Šimek 2010)	Dovetail	-	-	X

(Tannert, Lam, and Vallée 2010)	Rounded dovetail	X	X	X
(Ogawa, Sasaki, and Yamasaki 2015)	*Watari-ago*: notched beams	X	X	-
(Shope 2016)	Double birdsmouth	X	X	-
(Roche 2017)	Timber plates	X	X	X
(S.-Y. Yeo et al. 2016)	*Dieh-Dou*: stacked bracket system	X	X	-

2.1.1 Analytical methods

2.1.1.1 Wood mechanics

Wood is not an isotropic material, so when defining its stiffness, the orientation to grain is important. In this thesis, E_0 represents the material's Young's modulus parallel to grain and E_{90} represents the material's Young's modulus perpendicular to grain. If a timber material has a known E_0 and E_{90}, the Young's modulus at some angle β to the grain can be defined by Hankinson's formula:

$$E(\beta) = \frac{E_0 * E_{90}}{E_0 \cos^n \beta + E_{90} \sin^n \beta} \quad (1)$$

where $n = 2$ (Hankinson 1921).

2.1.1.2 Strength-based analyses of joinery connections

A handful of the represented literature, shaded in Table 1, test for the strength rather than for stiffness of joinery connections. Quantifying strength is most notably relevant for pegged tension joinery. The analytical method provided for the pegged mortise-and-tenon in Schmidt and Mackay (1997) uses the European Yield Model, which focuses on the failure modes of the joint under tension load, all of which involve shearing of the peg. Studies like Shanks and Walker (2009) further develop the analytical model for this pegged mortise-and-tenon tension joint by considering elasto-plastic behavior and energy dissipation of the peg. Shope (2016) uses an analytical method that is generally unique in the literature, applying the concept of stress fields to estimating the strength of a double birdsmouth joint under compressive load. Hankinson's formula is used to represent the reduction of stiffness associated with wood grain direction.

2.1.1.3 Characterizing rotational stiffness of joinery connections using the embedment model

Primarily, though, the literature presented in Table 1 seek to characterize the semi-rigid behavior of joinery connections, i.e. quantify the stiffness provided by these joint connections. The analytical method presented by Brungraber (1985) represents the joinery connection as a semi-rigid joint with three springs (one axial, one shear, and one rotational). Stiffness matrices are developed to represent the behavior of the joints under static load.

Since then, most literature rely on the theoretical framework of embedment established by Inayama (1991). While the original work is presented in Japanese, the theoretical framework can

be extrapolated from various English-language publications that apply the methods, such as Komatsu et al. (2009), Ogawa, Sasaki, and Yamasaki (2015), Yeo et al. (2016), and Tanahashi and Suzuki (2020). The theory and its methods are implemented in *Fundamental Theory of Timber Engineering* by the Architectural Institute of Japan (Architectural Institute of Japan (AIJ) 2010). The theory has been successfully implemented not only on traditional linear wood elements but also on joinery connections between timber plates: Roche (2017) implements the embedment theory in chapters 5-7 in characterizing the semi-rigidity of joinery connecting thin structural wood panels.

In considering the behavior of most joinery connections, the "triangular embedment with exponential-shaped additional length" model established by Inayama has been shown, and is often used, to capture the rotational stiffness provided by rotational partial compression of one wood element against another. For more documentation of other moment-resisting embedment models, the reader is referred to section 2.2 of Roche (2017), in addition to Tanahashi and Suzuki (2020).

The methodology from Inayama's embedment theory applied in this work is presented in Section 3.

2.1.2 Experimental methods

Nearly all of the literature summarized in Table 1 validate the presented models against experimental testing. The experimental testing usually involves applying some increasing load from one timber component on another and recording the corresponding displacement. Scopes in the literature range from material level embedment behavior to global timber frame behavior, and prototypes were usually built to the corresponding scale. For studies that examine a specific joinery type, usually prototypes of the specific joinery geometry are fabricated and tested.

2.1.3 Numerical methods

Most numerical simulations of joinery behavior included in Table 1 utilize a type of finite element analysis (FEA) called contact FEA, which accounts for the stress at contact interfaces. These interactions are important to model since they capture the local material behavior at interfaces and pose a greater technical challenge than the scope of FEA typically used in structural engineering modeling.

2.1.4 Static behavior of mortise-and-tenon-type joinery

One of the most fundamental joinery geometries is the mortise-and-tenon joint, also called the *Nuki* joint in Japanese (Figure 16).

Several pieces in literature examine the Nuki joint in different variations; North American variations typically include pegs for shear resistance, while Japanese variations sometimes include wedges to close any differential gaps between mortise and tenon.

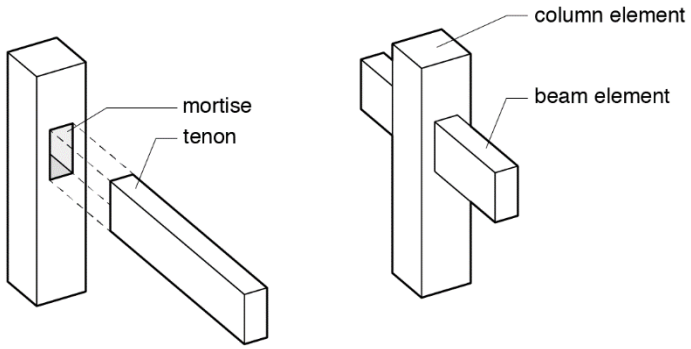

Figure 16. The traditional Japanese Nuki geometry as a mortise-and-tenon-type joinery connection for beams and columns.

For those studies that characterized the stiffness of the Nuki joint, regardless of the method used to characterize the stiffness behavior, most demonstrated or utilized a bilinear model (Komatsu et al. 2009; Guan, Kitamori, and Komatsu 2008; Chang, Hsu, and Komatsu 2006; Chang and Hsu 2007). The joint would first exhibit some initial stiffness relating load with displacement, or moment with angular displacement. After some threshold (predicted by an analytical model or numerical simulation, or observed in experimental testing), the stiffness would soften to a second plastic stiffness which occurs when the crushing of wood perpendicular to the grain enters the plastic region.

2.2 Dynamic analysis

A number of works have studied the seismic behavior joinery connections, particularly of East Asian joinery connections. These studies are dominated by quasi-static tests, both experimental and numerical (D'Ayala and Tsai 2008; Li et al. 2015; Chen Zhiyong et al. 2016; L. Chen et al. 2017; J. Chen et al. 2018; Y. Wu, Song, and Li 2018) .

Experimental dynamic testing are also common, sometimes with global scale models and shake tables (J. Chen et al. 2018; Y. J. Wu, Song, and Luo 2017; Xie et al. 2018; Suzuki and Maeno 2006; Y. Wu et al. 2018). (In one outstanding case, microtremor and free vibration tests were done on a newly built traditional pagoda in full scale (Hanazato et al. 2004).) Most works examined the dynamic properties of joints in partial context or in isolation (Li et al. 2015; L. Chen et al. 2017; Xue, Xu, and Xia 2018; Fujita et al. 2000; S. Y. Yeo et al. 2016). Most of these studies report on the hysteresis behavior, stiffness degradation, and energy dissipation of the joints. For global models, modal analyses were sometimes included (Hanazato et al. 2004; Y. Wu, Song, and Ventura 2019).

For frames with mortise-and-tenon joints and even dovetail variants, pull-out is the most common form of failure (Li et al. 2015; L. Chen et al. 2017). This failure was also observed directly in the field, in a post-disaster investigation following the Tangshan earthquake of 1976. The same study observed that in general, the timber structures in the affected area sustained much less damage and collapse than did masonry structures (Huixian et al. 2002).

With shake table tests, cyclic loading is sometimes at a slow enough scale that it is still a quasi-static test. Dynamic tests include microtremors/white noise (high frequency, small amplitude), free vibration, sine wave, and earthquake history inputs.

Aside from mortise-and-tenon and dovetail joints, the seismic behavior of stacked bracket sets on tops of columns are also of interest. These joinery connections are sometimes reported to demonstrate a higher damping than would be seen in the connections of reinforced concrete or steel structures (Xie et al. 2018; Fujita et al. 2000; S. Y. Yeo et al. 2016).

In most studies, the effect of vertical loading was examined. Depending on the joint, vertical loading could sometimes improve the joint stiffness, but increased vertical loading also meant greater mass for greater inertial effects under earthquake loading (Chang et al. 2012; Chen Zhiyong et al. 2016; S. Y. Yeo et al. 2016; J. Chen et al. 2018).

A few studies looked at the effect of tightness of the joinery connection on behavior. Generally, the looser the joint, the lower the rotational stiffness (Xue, Xu, and Xia 2018). In works like (Hanazato et al. 2004), the tightness in the joinery connections were cited as the likely reason behind a much higher observed damping than predicted. Other works like (S. Y. Yeo et al. 2016) identified friction force between contact surfaces as critical for the frame's overall structural integrity. The aforementioned common failure mode of tenon pull-out also indicates that friction and tightness in joinery connections play an important role on failure.

A few authors have recognized the importance of the semi-rigidity of joints on P-delta effects in the global structure and specifically addressed those effects (Li et al. 2015; King, Yen, and Yen 1996).

Generally, the good seismic behavior of structures with joinery connections are attributed to the plastic deformation – and resulting energy dissipation and damping – that occur at the joinery connections under seismic events (Chen Zhiyong et al. 2016; Tanabashi 1960; Que et al. 2017).

2.3 Digital fabrication and joinery

Recent developments have demonstrated the potential of robotic fabrication methods to reproduce joinery connections, ranging from specific joints like the dovetail and finger joints (Page 2017) to historic timber frame component replacement in Chile (Böhme, Zapata, and Ansaldo 2017), to a complete and faithful reproduction of a traditional Japanese pagoda (Takabayashi, Kado, and Hirasawa 2019). In practice, modern fabricators of timber frame components are already using state-of-the-art CNC machines to produce their parts.

2.4 Evaluating sustainability of early-stage structural design exploration using embodied carbon

The mitigation of carbon in the built environment is becoming more and more acknowledged as a priority, particularly the mitigation of embodied carbon. Pomponi and Moncaster 2016 have determined that pluralistic, multidisciplinary approaches are essential for conducting effective life cycle analyses (LCAs) for improved methods of designing low-carbon structures, while De Wolf 2017 identifies the two main pathways as (1) reducing structural material quantities and (2) designing with materials with lower embodied carbon. Databases such as the Database of Embodied Quantity Outputs (DEQO) represent the development of transparent, open-source, and reliable resources to assist the design of low-carbon structures (C. De Wolf et al. 2020). Other tools have arisen in industry that reflect a widespread desire to facilitate low-carbon structural design (KT Innovations, thinkstep, and Autodesk 2019; Building Transparency 2019; CORE Studio 2020).

In parallel to these efforts to collect data is the effort to develop improved methodologies for low-carbon structural design. One early study implementing LCA in early-stage structural design demonstrated a 65.1% reduction in embodied energy and 67.2% reduction in carbon dioxide emissions by selecting a cable long-span structural system over a truss system (Trussoni et al. 2015). In another study, this methodology was generalized for spanning trusses of varying geometry and material combinations, examining and optimizing the tradeoff of timber truss elements being lower in embodied carbon but also lower in strength (Stern 2018). In both of these studies, primary structural elements were considered and the material contribution of connection details were not included.

Another study assesses the feasibility of timber for structural systems of tall buildings, comparing the embodied carbon of a tall timber tower to that of a benchmark concrete building. A hybrid system is proposed where concrete joints provide rotational restraint to reduce timber floor plate material. The all-timber scheme considered in Appendix C of this report is assumed to have an all-pinned scheme and is found to be less materially efficient than the timber-concrete composite system for a tall building (Skidmore, Owings & Merrill, LLP 2013).

2.5 Problem statement

Both the literature on the dynamic performance of joinery and the digital fabrication capabilities available today clarify the potential for joinery connections to re-exist in modern timber construction. However, the sustainability benefits of re-introducing joinery connections remain unclear.

The literature sets out established methods for evaluating the stiffness of joinery connections. The Nuki joint, or mortise-and-tenon beam-through-column joint, is identified as a fundamental joinery geometry that has been evaluated and used for different structural systems.

However, the behavior of the Nuki joint has yet to be characterized in a way that is compatible with and applicable to structural design at the scale of modern mass timber projects. At this scale, it is also unclear how the Nuki joint compares to modern conventional timber connections. Both of these gaps may explain why joinery connections are largely absent from modern-day mass timber structures.

2.6 Thesis format

This thesis seeks to consolidate existing literature on characterizing the Nuki joint to improve the accessibility of joinery analysis for structural designers. A comparative study of structural design with joinery and conventional timber connections is presented to highlight the benefits of applying joinery in modern timber construction. Both approaches aim to reduce the barrier of entry of joinery to modern structural design.

First, models that have been developed in literature are reconstructed on a Nuki joint. The analytical, experimental, and numerical methodologies described in Section 3 are reproducible on other joinery geometries.

The results of applying these three analysis methods on the Nuki joint of varying beam widths is presented in Section 4. The bilinear behavior described in literature is observed, and the models are calibrated based on specific material properties of the experimental prototypes. Particular attention is given to the elastic rotational stiffness and the threshold moment before the joint exhibits plastic behavior, as those two parameters are to be applied in structural design.

Finally, the analytical model developed in Section 4 is applied to a comparative study between a beam supported by Nuki joints with a more conventional timber connection design (Section 5). In particular, the embodied carbon quantities between the systems are compared.

3 Methodology for characterizing the static mechanical behavior of the Nuki joint

In this section, the methodology for characterizing the static mechanical behavior of the Nuki joint is described. These methods are based on literature and are used to determine the results in Section 4.

3.1 Analytical method: general approach

As discussed in Section 2.1.1.3, the "triangular embedment with exponential-shaped additional length" model established by Inayama (1991) will primarily be used here to capture the rotational stiffness provided by rotational partial compression of one wood element against another. The triangular embedment refers to the compression of wood fibers perpendicular to the grain due to the contact rotation of another element. The additional indirect embedment stress is experienced by the exposed portion just outside the direct contact region. If the embedment is acting in the z-direction, this additional indirect stress can occur in both x- and y-directions of

the compressed element (Figure 17). As the name of the method suggests, the indirect embedment shapes can be approximated as an exponential function.

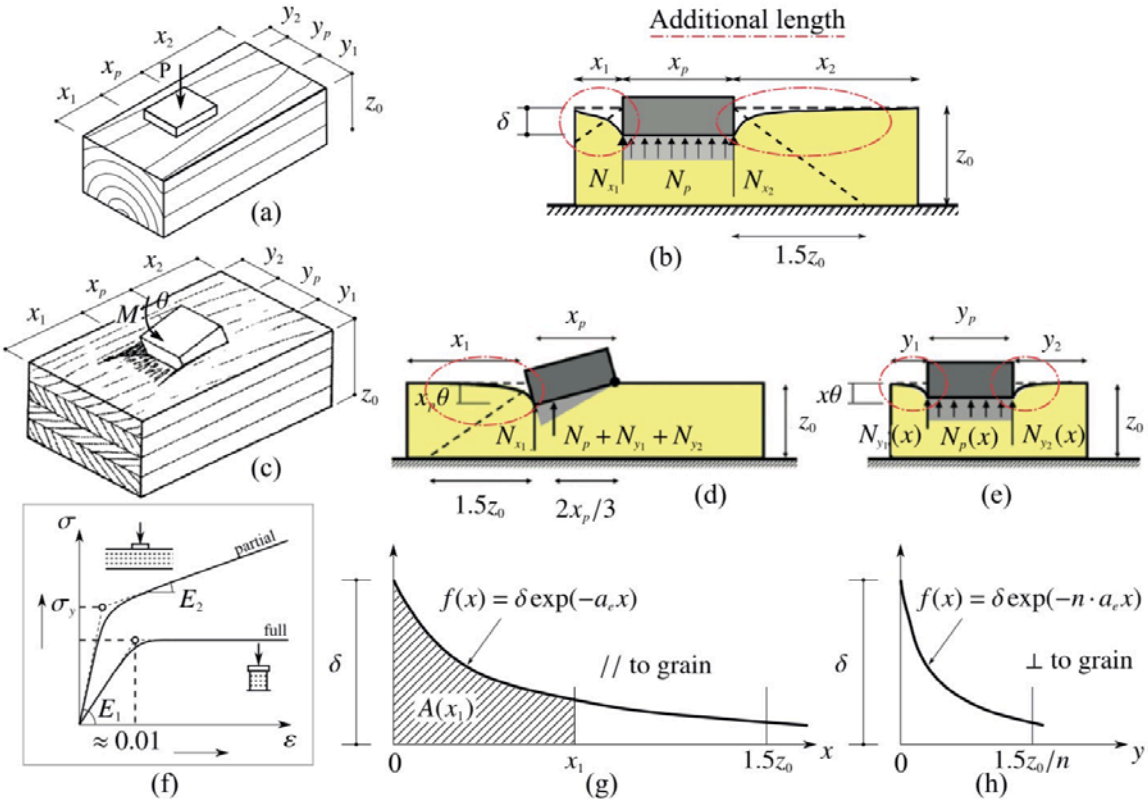

Figure 17. These illustrations show the surface deformation of the indirectly loaded area just outside of the area under direct contact with embedment. (c) through (e) illustrate the case of rotational partial compression from different angles. Figure by (Roche 2017), synthesizing images from (Inayama 1991; 1993; Architectural Institute of Japan (AIJ) 2010).

The indirect embedment shape takes the form of

$$f(x) = \Delta e^{-\alpha x} \tag{2}$$

where Δ represents the linear compression depth at the end of direct triangular embedment and α represents the decay coefficient, a value that has been tested extensively in the literature but is taken by the AIJ to be $1.5/Z_0$, where Z_0 is the initial depth of the compressed element (Figure 17). Further documentation on literature investigating decay coefficients is provided in Section 2.2 of Roche 2017 (Roche 2017) under the heading "Complementary studies on the decay coefficient a_e".

Integrating direct embedment $\Delta(x)$ and indirect embedment $f(x)$ along x- and y-axes, the values of compressed volumes V can be obtained. Using Hooke's law, compressed volumes can then be used to calculate resultant contact force N:

$$N=\sigma A=\varepsilon EA=(\varepsilon A)E=\frac{V}{Z_0}E \tag{3}$$

Rewriting the equation as a function of rotation angle θ:

$$N(\theta)=\frac{V(\theta)}{Z_0(\theta)}E(\theta) \tag{4}$$

A yield depth $\Delta_y = \varepsilon_y Z_0$ indicates that the crushing of wood has entered the plastic region, where ε_y represents the yield strain material property across the grain. For embedment depths beyond Δ_y, a reduced material Young's modulus E must be used.

Once contact forces N and the associated lever arm lengths a are determined, the relationship between moment M and rotation angle θ can be determined. Summarized for elastic and plastic regions, the relationship can be stated as:

$$M(\theta) = \sum N_i(\theta)\, a_i(\theta) \tag{5}$$

3.2 Analytical method: Nuki joint

This section details the analytical model specifically developed for the Nuki joint. The model presented in this section is based on, and updated from, work presented in Fang, Mueller, et al. 2019.

When the beam is loaded, the Nuki joint experiences rotational displacement. This causes rotational partial compression at two locations in the beam.

If the beam sufficiently pierced through the column, the behavior at both embedment locations might be equivalent due to symmetry. However, due to limitations in the experimental testing phase, this case study was asymmetric: on one end, the beam element was only inserted 1 inch past the edge of the column element. As a result, the additional embedment length on that end of the beam is limited by the amount of beam length remaining. The embedment at the two locations are thus not equivalent in this particular case study and need to be calculated separately. The subscript *e* is used to denote the ended beam end, while the subscript *c* is used to denote the continuous beam end. The following discussion of parameters apply to each embedment location.

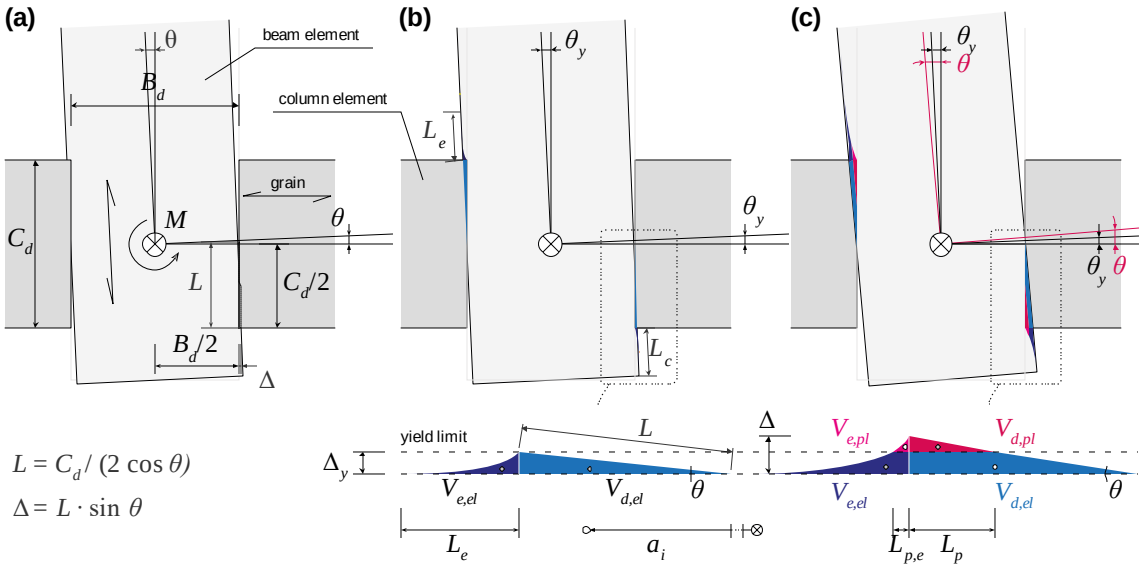

Figure 18. Analytical model (as a cut section down the middle of the prototype width): (a) joint geometry dimensions, (b) elastically compressed volumes, and (c) compressed volumes for an elastoplastic material behavior. Elastically compressed volumes are shown in blue tones; plastic volumes are given in magenta tones. The boxed diagrams in (b) and (c) represent the contact at the ended beam end and thus the subscripts e are used; the diagrams are analogous for the continuous beam end, where subscripts e would be replaced with subscripts c. Note that the formula for L has been updated since the original published study. Adapted from original illustration by collaborator Jan Brütting.

The following relationships apply for rotational displacement θ between 0 and $\frac{\pi}{2}$ radians, measured relative to the center of rotation ⊗, which is here assumed to be fixed throughout. Final results are presented only for some range of radians that approximately matches the range observed in experimental testing for this case study.

Z is used to denote the depth of material experiencing embedment; in this prototype, Z is expressed as a function of θ:

$$Z(\theta) = B_d \cos\theta \tag{6}$$

Δ represents the embedment depth, the maximum embedment which occurs at the edge of direct contact and additional embedment. It is a function of θ:

$$\Delta(\theta) = L(\theta) \sin\theta \tag{7}$$

The length L represents the beam length experiencing embedment. Initially, this value is half the column depth, or $\frac{C_d}{2}$. As rotational displacement θ increases, so does L:

$$L(\theta) = \frac{C_d/2}{\cos\theta} \tag{8}$$

Δ_y represents the embedment depth at the point of yielding, and θ_y represents the rotational displacement at the point of yielding. Given the material yield strain ε_y across the grain, Δ_y can be calculated as

$$\Delta_y = \varepsilon_y B_d \tag{9}$$

Evaluating $\Delta_y = \Delta(\theta_y)$, it follows from Equations (7) and (8) that

$$\theta_y = \tan^{-1}\left(\frac{\varepsilon_y B_d}{C_d/2}\right) \tag{10}$$

Once the yield limits Δ_y and θ_y are determined, it is possible to assign the respective elastic and plastic Young's moduli to the respective compressed volumes. The compressed volumes can in this case be calculated by calculating the area in section and multiplying by the uniform depth B_w.

3.2.1 Elastic embedment

Figure 18(b) illustrates the elastic case where $\Delta < \Delta_y$; both compressed volumes are in the elastic region, hence the blue tones. The lighter blue volume is under direct contact and is thus called $V_{d,el}$. The darker blue volume is the additional exponential-shaped length; the end that is limited by the ended beam end is called $V_{e,el}$ and the analogous compressed volume along the continuous beam end is called $V_{c,el}$.

The exponential-shaped length takes the form of

$$f(\theta, x) = \Delta(\theta) * e^{-\alpha x} \tag{11}$$

where the x-axis lies along the beam edge, starting from the edge of embedment and positive direction pointing away from direct contact. The decay coefficient α is taken to be $6.5/B_d$, a value recommended in most literature. The literature also reports recommended embedment lengths across which to integrate $f(x)$ in order to calculate the compressed volumes for additional embedment $V_{e,el}$ and $V_{c,el}$. Embedment length for the ended beam end, L_e, is taken to be 1 inch, whereas embedment length for the continuous beam end, L_e, is taken from literature to be $1.5B_d$.

All compressed volumes for the elastic case ($\Delta < \Delta_y$) can now be calculated:

$$V_{d,el}(\theta) = B_w * \frac{1}{2}\Delta(\theta) * L\cos\theta \tag{12}$$

$$V_{e,el}(\theta) = B_w * \int_{x=0}^{L_e} f(\theta, x)\, dx\,, \qquad L_e = 1 \text{ in.} \tag{13}$$

$$V_{c,el}(\theta) = B_w * \int_{x=0}^{L_c} f(\theta, x)\, dx\,, \qquad L_c = 1.5B_d \tag{14}$$

The compressed volumes can then be converted into resultant contact forces using the relationship $N(\theta)=\frac{V(\theta)}{Z(\theta)}E(\theta)$. While the compressed volume is initially being compressed precisely perpendicular to the grain, as θ increases, the wood grain becomes more and more aligned with the compression direction. E is thus taken as a function of θ using the following expression of Hankinson's formula:

$$E(\theta) = \frac{E_0 * E_{90}}{E_0 \cos^n\left(\frac{\pi}{2} - \theta\right) + E_{90} \sin^n\left(\frac{\pi}{2} - \theta\right)}, \qquad n = 2 \tag{15}$$

The resultant contact forces are:

$$N_{d,el}(\theta) = \frac{V_{d,el}(\theta)}{Z(\theta)} E(\theta) \tag{16}$$

$$N_{e,el}(\theta) = \frac{V_{e,el}(\theta)}{Z(\theta)} E(\theta) \tag{17}$$

$$N_{c,el}(\theta) = \frac{V_{c,el}(\theta)}{Z(\theta)} E(\theta) \tag{18}$$

Finally, the moment arm for each resultant force needs to be calculated to determine the rotational stiffness. The moment arm is the distance (in the direction perpendicular to the associated resultant force) between the center of rotation ⊗ and the centroid of each compressed volume.

$$a_{d,el}(\theta) = \frac{2}{3} L(\theta) * \cos\theta \tag{19}$$

Note that $L(\theta) * \cos\theta = \frac{C_d}{2}$, so $a_{d,el}$ is actually a constant and not a function of θ.

$$a_{e,el}(\theta) = \frac{C_d}{2} + \frac{1}{V_{e,el}} \int_{x=0}^{L_e} x * f(\theta, x) dx, \qquad L_e = 1 \text{ in.} \tag{20}$$

$$a_{c,el}(\theta) = \frac{C_d}{2} + \frac{1}{V_{c,el}} \int_{x=0}^{L_c} x * f(\theta, x) dx, \qquad L_c = 1.5 B_d \tag{21}$$

3.2.2 Plastic embedment

Figure 18(c) illustrates the case where $\Delta > \Delta_y$; magenta tones denote the compressed volumes that are operating in the plastic region. These volumes must be calculated separately from the elastic ones.

While calculating compressed volumes, it is helpful to define a few dimensions. First, L_p is defined as the length along the axis of the beam, between elastic and plastic compressed volumes (Figure 18):

$$L_p(\theta) = \frac{C_d}{2} * \left(1 - \frac{\Delta_y}{\Delta(\theta)}\right) \tag{22}$$

Additionally, $L_{p,e}$ and $L_{p,c}$ are defined as the lengths along the x-axis of additional embedment length (for their respective beam ends) at which the additional embedment shape matches yield embedment depth Δ_y:

$$L_{p,e} = L_{p,c} = f^{-1}(\Delta_y) \tag{23}$$

The compressed volumes can then be defined as the following, with some volumes split into two parts for ease of centroid calculation:

$$V_{d,el,1}(\theta) = B_w * \frac{1}{2}\Delta_y * \left(L(\theta) * \cos\theta - L_p(\theta)\right) \tag{24}$$

$$V_{d,el,2}(\theta) = B_w * \Delta_y L_p(\theta) \tag{25}$$

$$V_{d,pl}(\theta) = B_w * \frac{1}{2}\left(\Delta(\theta) - \Delta_y\right) L_p(\theta) \tag{26}$$

The compressed volumes at the ended beam end are:

$$V_{e,el,1} = B_w * L_{p,e}\Delta_y \tag{27}$$

$$V_{e,el,2}(\theta) = B_w * \int_{L_{p,e}}^{L_e} f(\theta, x)\, dx \tag{28}$$

$$V_{e,pl}(\theta) = B_w * \int_{0}^{L_{p,e}} f(\theta, x) - \Delta_y\, dx \tag{29}$$

Analogously, for the continuous beam end:

$$V_{c,el,1} = B_w * L_{p,c}\Delta_y \tag{30}$$

$$V_{c,el,2}(\theta) = B_w * \int_{L_{p,c}}^{L_c} f(\theta, x)\, dx \tag{31}$$

$$V_{c,pl}(\theta) = B_w * \int_{0}^{L_{p,c}} f(\theta, x) - \Delta_y\, dx \tag{32}$$

In the next step of converting the compressed volumes into resultant contact forces, again the relationship $N(\theta)=\frac{V(\theta)}{Z(\theta)}E(\theta)$ is applied. However, the Young's moduli for plastically compressed volumes must be adjusted to reflect the plastic stiffness. A bilinear material model is assumed where PR_{90} represents the factor by which the Young's modulus in the elastic region is reduced to obtain the Young's modulus in the plastic region.

$$N_{d,el,i}(\theta) = \frac{V_{d,el,i}(\theta)}{Z(\theta)}E(\theta), \qquad \text{for all i} \tag{33}$$

$$N_{d,pl}(\theta) = \frac{V_{d,pl}(\theta)}{Z(\theta)}\left(PR_{90} * E(\theta)\right) \tag{34}$$

$$N_{e,el,i}(\theta) = \frac{V_{e,el,i}(\theta)}{Z(\theta)}E(\theta), \qquad \text{for all i} \tag{35}$$

$$N_{e,pl}(\theta) = \frac{V_{e,pl}(\theta)}{Z(\theta)}\left(PR_{90} * E(\theta)\right) \tag{36}$$

$$N_{c,el,i}(\theta) = \frac{V_{c,el,i}(\theta)}{Z(\theta)}E(\theta), \qquad \text{for all i} \tag{37}$$

$$N_{c,pl}(\theta) = \frac{V_{c,pl}(\theta)}{Z(\theta)}\left(PR_{90} * E(\theta)\right) \tag{38}$$

Finally, moment arms are determined. For direct contact:

$$a_{d,el,1}(\theta) = \frac{2}{3}\left(\frac{C_d}{2} - L_p(\theta)\right) \tag{39}$$

$$a_{d,el,2}(\theta) = \frac{C_d}{2} - \frac{L_p(\theta)}{2} \tag{40}$$

$$a_{d,pl}(\theta) = \frac{C_d}{2} - \frac{L_p(\theta)}{3} \tag{41}$$

Moment arms at ended beam end:

$$a_{e,el,1} = \frac{C_d}{2} + \frac{L_{p,e}}{2} \tag{42}$$

$$a_{e,el,2}(\theta) = \frac{C_d}{2} + \frac{1}{V_{e.el,2}}\int_{L_{p,e}}^{L_e} x * f(\theta, x)\, dx \tag{43}$$

$$a_{e,pl}(\theta) = \frac{C_d}{2} + \frac{1}{V_{e,pl}}\int_{0}^{L_{p,e}} x * (f(\theta, x) - \Delta_y)\, dx \tag{44}$$

Analogously, moment arms at continuous beam end:

$$a_{c,el,1} = \frac{C_d}{2} + \frac{L_{c,e}}{2} \tag{45}$$

$$a_{c,el,2}(\theta) = \frac{C_d}{2} + \frac{1}{V_{c.el,2}} \int_{L_{p,c}}^{L_c} x * f(\theta, x)\, dx \tag{46}$$

$$a_{c,pl}(\theta) = \frac{C_d}{2} + \frac{1}{V_{c,pl}} \int_{0}^{L_{p,c}} x * (f(\theta, x) - \Delta_y)\, dx \tag{47}$$

3.2.3 Contribution of friction

Friction from wood-wood contact – that is, direct contact only – contributes to the moment experienced at the joint. This moment contribution is calculated using the material's static coefficient of friction μ. The force of friction F_f acts along the length of the beam element and arises from every normal force acting at both contact points:

$$F_f(\theta) = \mu * \sum_{\mathrm{i} \in \mathrm{d}} \mathrm{N_i}(\theta) \tag{48}$$

Note that the additional indirect embedment forces do not contribute to friction.

The associated moment arm for F_f is notated as a_f and represents the perpendicular distance between the friction forces. In this case, it is equivalent to the beam depth:

$$a_f = B_d \tag{49}$$

3.2.4 Determining rotational stiffness

Generally, the resultant forces N and associated moment arms a can be synthesized as follows to determine the relationship between moment and angular displacement:

$$M(\theta) = \sum_{i \in (d \cup e \cup c \cup f)} N_i(\theta) a_i(\theta) \tag{50}$$

where d represents direct contact, e represents additional embedment along the ended end, c represents additional embedment along the continuous end, and f represents friction.

Because the formulas for some normal forces are dependent on whether the plastic region is reached or not, details of the summations for each region are detailed below.

If the rotations are in the elastic region ($\theta < \theta_y$), the relationship can be expressed as follows:

$$M_{el}(\theta) = 2[N_{d,el}(\theta) a_{d,el}(\theta)] + N_{e,el}(\theta) a_{e,el}(\theta) + N_{c,el}(\theta) a_{c,el}(\theta) + \mu N_{d,el}(\theta) B_d \tag{51}$$

where formulas for each are detailed in Section 3.2.1.

If in the plastic region ($\theta \geq \theta_y$), the relationship in this case is:

$$\begin{aligned} M_{pl}(\theta) = 2[N_{d,el}(\theta)a_{d,el}(\theta) + N_{d,pl}(\theta)a_{d,pl}(\theta)] + N_{e,el,1}(\theta)a_{e,el,1}(\theta) \\ + N_{e,el,2}(\theta)a_{e,el,2}(\theta) + N_{c,el,1}(\theta)a_{c,el,1}(\theta) \\ + N_{c,el,2}(\theta)a_{c,el,2}(\theta) + N_{e,pl}(\theta)a_{e,pl}(\theta) + N_{c,pl}(\theta)a_{c,pl}(\theta) \\ + \mu[N_{d,el}(\theta)B_d + N_{d,pl}(\theta)B_d] \end{aligned} \quad (52)$$

where formulas for each are detailed in Section 3.2.2.

The general formula can be written as a piecewise function of the functions in each region:

$$M(\theta) = \begin{cases} M_{el}(\theta) & \text{when } \theta < \theta_y \\ M_{pl}(\theta) & \text{when } \theta \geq \theta_y \end{cases} \quad (53)$$

The resulting function can be plotted and compared to results obtained using experimental or numerical methods.

A bilinear behavior is usually observed. The two slopes representing the two rotational stiffnesses associated with each plot can be determined by calculating $\frac{\partial M}{\partial \theta}$ at a point in each region. The point in the elastic region was selected to be at $\theta = \frac{\theta_y}{2}$ and in the plastic region $\theta = 3\theta_y$.

The code used to run the analytical models are provided in Appendix 1.

3.3 Experimental methods

Prototypes of each joint are fabricated and load-tested. Two fabrication methods are used in this work; the first is hand carpentry, and the second is digital fabrication using 3-axis CNC machines.

Load-testing of the rotational stiffness of the joint is done by applying a force on the beam element while anchoring the column element, as in Figure 19. The rotation at the joint can be measured using string potentiometers.

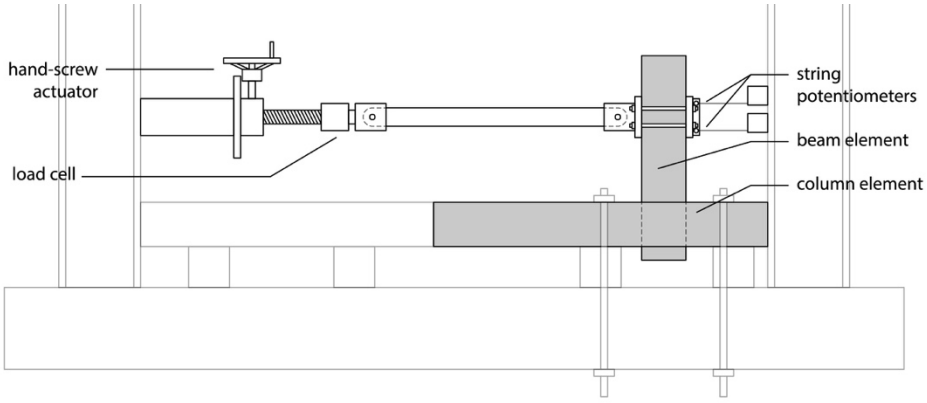

Figure 19. Setup for experimental load-testing of Nuki joint prototypes. Graphic made with collaborator Jan Brütting.

For the Douglas fir prototypes, 3 specimens for each beam width were fabricated using hand carpentry techniques. For the glulam prototypes, 6 specimens for each beam width were digitally fabricated with a robotic CNC router. The opening in the columns has rounded corners equal to the size of router ball end, i.e. 3/8 inches (Figure 20).

Figure 20. Mortise with rounded corners in the digitally fabricated prototypes.

In the test setup, which is shown in Figure 19, the column element of the joint was fixed to the table, while the beam element was attached to a hand-screw-actuated load cell of 1000 lb capacity. The beam-column connection was not press-fit, and varied in tightness. The total gap between the beam and column ranged from 0 to about 0.08 inches. A linear displacement was applied at the beam end using the load cell, and the resulting rotation at the joint was measured by two string potentiometers. Figure 21 shows example progressive frames from one prototype.

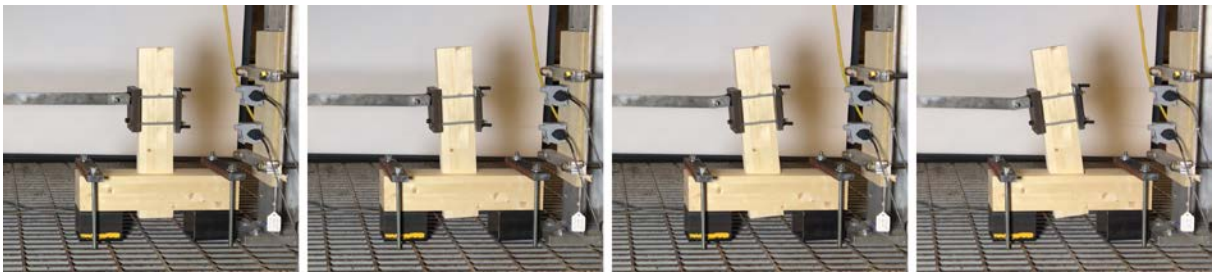

Figure 21. Progressive frames from testing rotational stiffness of glulam specimens.

3.4 Numerical methods

Any finite element analysis (FEA) program that has the capability of modeling the behavior of contact interfaces could be used to model the behavior of joinery connections. In this study, LS-DYNA was used where numerical methods were used. Equipped with material data provided by material testing at MIT, collaborators at Arup San Francisco (Aliz Fischer, Benshun Shao, Julieta

Moradei) led the effort in creating material cards and numerical simulations of the joint under the same loading conditions as in the experimental testing. A side-by-side comparison of experimental and numerical testing setups is shown in Figure 22.

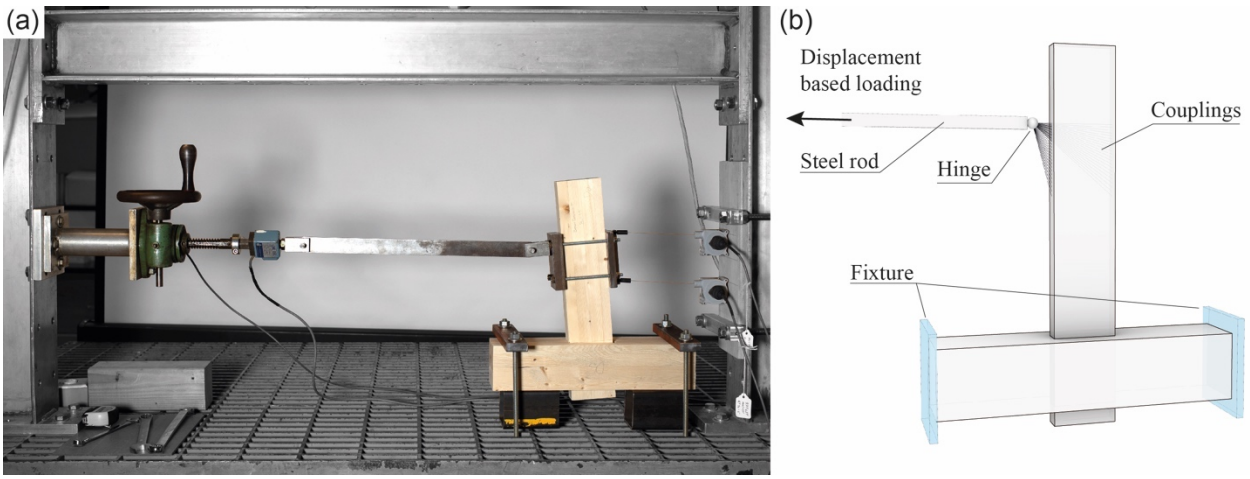

Figure 22. (a) Experimental setup for Nuki joint testing, and (b) boundary and loading conditions for numerical simulation. Figure by collaborators Aliz Fischer and Jan Brütting.

Using material testing to determine material parameters of the glulam (Table 5), a numerical model was built for the glulam prototypes by collaborators at Arup San Francisco. Other values, such as Poisson ratio $\upsilon = 0.39$, were estimated from literature (Forest Products Laboratory 2010). Contact between beam and column is defined by numerical parameters representing the contact stiffness, the friction between surfaces, and the initial gap size. In the model, the gap size between the beam and the column was set up based on observation of the fabrication, with 0.5 mm gap each side of the beam. At the top and bottom faces the gap was smaller, 0.025 mm, to ensure numerical stability. The analysis assumed no initial stress from joining the two pieces.

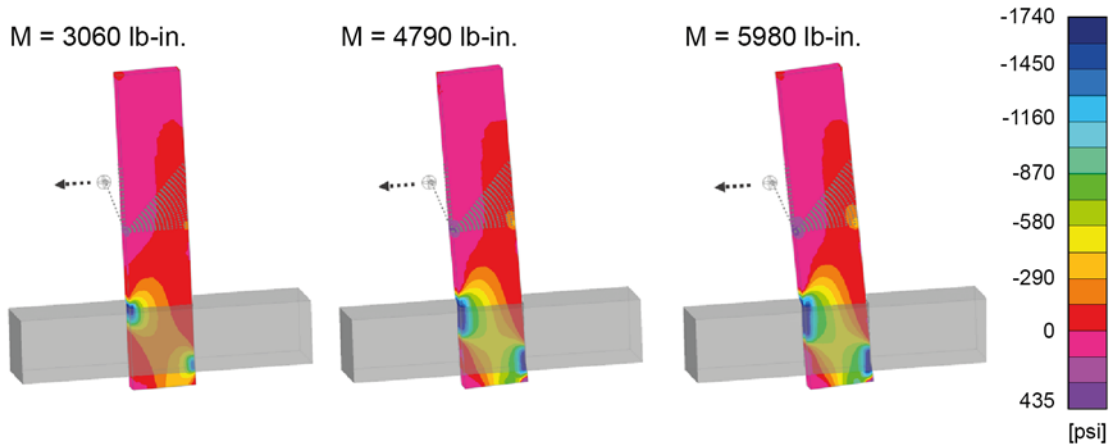

Figure 23. Stress in the beam perpendicular to grain (psi) throughout the numerical simulation for the B_w = 1 in. specimen. Analysis performed by Aliz Fischer, Benshun Shao, and Nick Sherrow-Groves of Arup San Francisco.

Selected images of the progression of the numerical simulation are shown in Figure 23. The contour plot shows the stresses perpendicular to the grain of the beam. The simulation was stopped when the analysis showed numerical instabilities as the damage at the contact became excessive.

For more details on the FEA methods, the reader is referred to Shao et al. 2019 and Fang, Moradei, et al. 2019.

3.5 Statement of contributions

While final findings and interpretations were synthesized by the author, parts of the methodologies and results presented in Section 4 were made possible by a number of collaborators.

Collaborators from the Arup San Francisco team (Aliz Fischer, Benshun Shao, Julieta Moradei, Nick Sherrow-Groves) developed and ran numerical simulations (Section 4.3.3).

Collaborators from EPFL (Jan Brütting, Corentin Fivet) helped develop the theory (Section 3.2) and code (Appendix 1) for the analytical model.

MIT undergraduate researcher Danny Landez carried out digital fabrication and experimental testing of the glulam prototypes (Section 4.3.2) under conditions as close as possible to those carried out by the author for the Douglas fir prototypes.

3.6 Summary

In this chapter, the analytical, experimental, and numerical approaches for characterizing the rotational stiffness of the Nuki joint are synthesized and presented based on existing literature. These methods are applied in Section 4 to characterize the rotational stiffness of a Nuki joint across varying beam widths. The methodology outlined may be adapted to other joinery geometries. A catalog detailing the rotational stiffnesses of different joinery geometries validated by these methods may be instrumental in promoting the use of joinery in modern structural design.

4 Static mechanical behavior of the Nuki joint

In this chapter, three methods for determining the mechanical behavior of the Nuki joint is described, and their results compared. The mechanical behavior studied is the rotational stiffness of the joint, a property that could determine how important a role this joint might play as a boundary condition in structural design.

Two sets of studies were done for the Nuki, differing in materials used and method of fabricating prototypes. These studies and their respective analysis methods are summarized in Table 2.

Table 2. Summary of Nuki joint case studies conducted.

Nuki joint case studies	Analytical	Experimental	Numerical
Douglas fir	X	X (hand carpentry)	-
Glulam	X	X (CNC)	X

The geometry of the Nuki joint is illustrated in Figure 24. The joint consists of a beam element acting as a tenon piercing through a fully mortised column element. The beam element will be loaded on one side to test the rotational stiffness of the joint. This loading condition will create double-contact rotational partial compression.

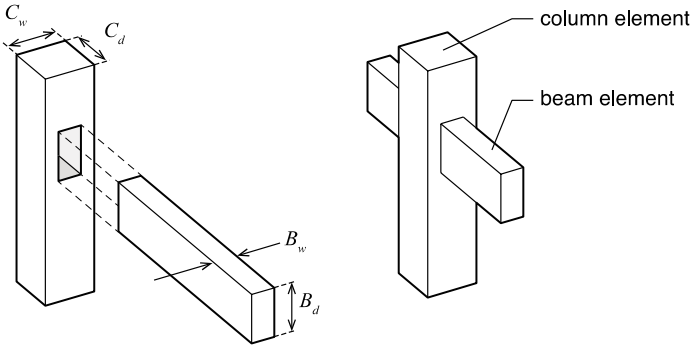

Figure 24. Nuki joint and associated dimensions examined in the case study.

The specific dimensions selected for the case study are summarized in Table 3. Two beam width values were investigated.

Table 3. Nuki joint dimensions used in the case study.

Column width	$C_w = 3\frac{1}{4}$ in.
Column depth	$C_d = 3\frac{1}{4}$ in.
Beam depth	$B_d = 3\frac{1}{4}$ in.
Beam width	$B_w = 1$ in. and $B_w = 1.5$ in.

4.1 Material properties

Where possible, standards defined by ASTM D143-14 (ASTM International 2014) were followed as closely as possible to test for material properties of the timber.

For Douglas fir, E_0 and E_{90} moduli were determined by taking the slopes of 5 specimens for each modulus, prepared according to ASTM D143-14 (ASTM International 2014). Because the test described for compression perpendicular to grain did not represent a pure E_{90} value, the true E_{90} value was estimated to be 90% the tested average value. Yield strain ε_y was determined by examining the testing data for compression perpendicular to grain and taking an average (Figure 25). The value for the coefficient of friction μ was selected according to typical values found in literature. A summary of the material properties used for analysis of the Douglas fir prototypes is provided in Table 4.

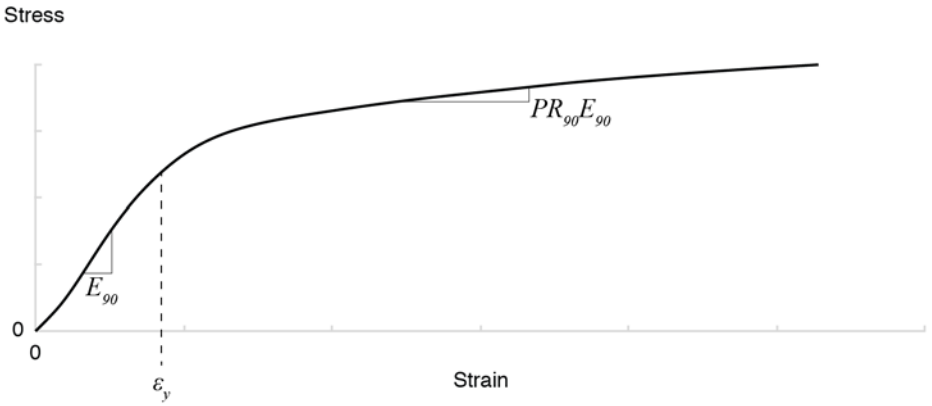

Figure 25. Generalized stress-strain behavior of timber under compression perpendicular to grain, and associated material values.

Table 4. Material properties used for Douglas fir prototypes.

Property	Value	Source
Stiffness (Young's modulus) parallel to grain	$E_0 = 1.57 \times 10^6$ lb/in.^{2}	Average of stress-strain slopes recorded from 5 specimens
Stiffness (Young's modulus) perpendicular to grain	$E_{90} = 36{,}500$ lb/in.^{2}	90% of average of stress-strain slopes recorded from 5 specimens
Yield strain compression perpendicular to grain	$\varepsilon_y = 0.018$	Average value observed from 5 specimens
Stiffness plastic reduction factor	$PR_{90} = 0.07$	Average value observed from 5 specimens
Static coefficient of friction	$\mu = 0.2$	Typical value found in literature

For the glulam, E_0 and E_{90} moduli were also determined by taking the slopes of 8 specimens for each modulus, prepared according to ASTM D143-14 (ASTM International 2014). To determine the pure E_{90} value, the compression-perpendicular-to-grain test was simulated in an FEA model and the E_{90} value tuned to match the experimental testing results (in this case, a 70% reduction of the tested value). Yield strain ε_y was determined by examining the testing data for compression perpendicular to grain and taking an average. The value for the coefficient of friction μ was selected according to typical values found in literature. A summary of the material properties used for analysis of the glulam prototypes is provided in Table 5.

Table 5. Material properties used for glue-laminated timber prototypes.

Property	Value	Source
Stiffness (Young's modulus) parallel to grain	$E_0 = 1.96 \times 10^6$ lb/in.^{2}	Average of stress-strain slopes recorded from 5 specimens
Stiffness (Young's modulus) perpendicular to grain	$E_{90} = 55{,}800$ lb/in.^{2}	70% of average of stress-strain slopes recorded from 5 specimens
Yield strain	$\varepsilon_y = 0.017$	Average value observed from 5 specimens
Stiffness plastic reduction factor	$PR_{90} = 0.118$	Average value observed from 5 specimens
Static coefficient of friction	$\mu = 0.2$	Typical value found in literature

4.2 Results: Douglas fir prototypes

The results for the prototypes made with Douglas fir are summarized below.

4.2.1 Analytical results

The $M(\theta)$ plots as determined by the analytical model of the Douglas fir Nuki joint are charted in Figure 26.

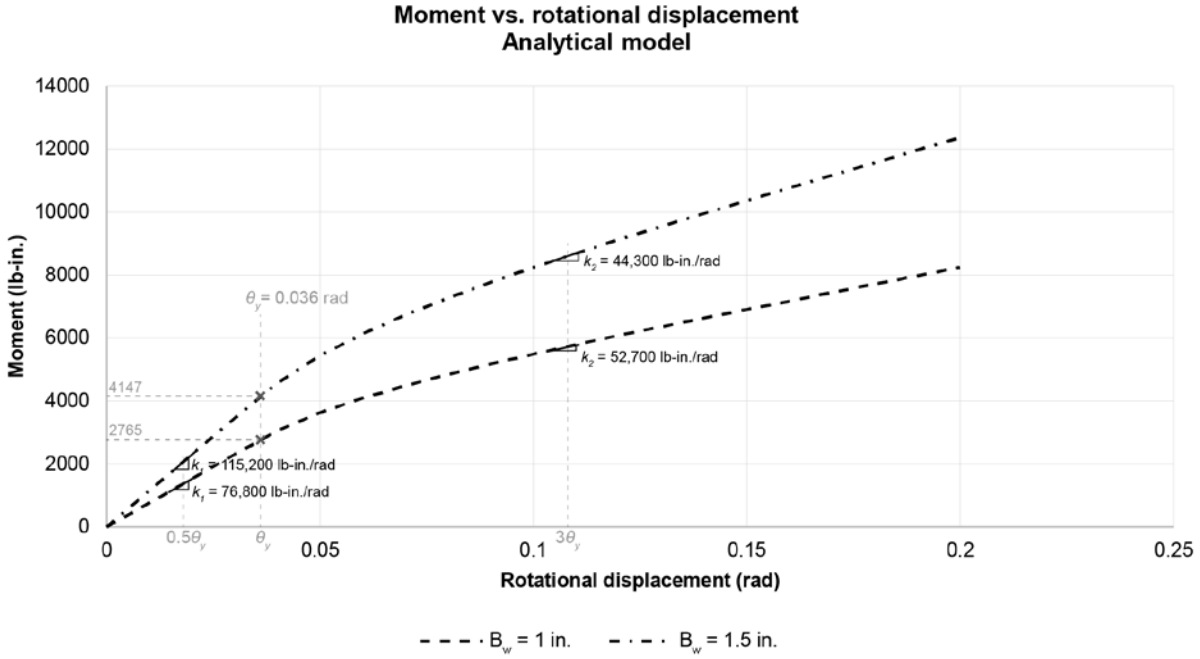

Figure 26. Moment-rotational-displacement curve for the Douglas fir Nuki joint determined by the analytical model.

The slopes in each linear region of elastic and plastic behavior are extracted and summarized in Table 6.

Table 6. Summary of rotational stiffnesses for the Douglas fir Nuki joint as determined by the analytical model.

	Elastic stiffness	Plastic stiffness
$B_w = 1$ in.	76,800 lb-in./rad	29,500 lb-in./rad
$B_w = 1.5$ in.	115,200 lb-in./rad	44,300 lb-in./rad
% increase in stiffness from $B_w = 1$ in. to $B_w = 1.5$ in.	50%	50%

Yield angle can be computed as $\theta_y = \tan^{-1}\left(\frac{\varepsilon_y B_d}{C_d/2}\right)$ according to the model established in Section 3.2, and yield moment M_y is the corresponding moment at $\theta = \theta_y$. Yield moment is 2765 lb-in. and 4147 lb-in. for $B_w = 1$ in. and $B_w = 1.5$ in., respectively.

4.2.2 Experimental results

Scans of the tested beam elements showing embedment are provided in Appendix 2.

The plots of moment against rotational displacement as extracted from experimental testing of all 3 prototypes of the Douglas fir Nuki joint, $B_w = 1$ in., are plotted in Figure 27.

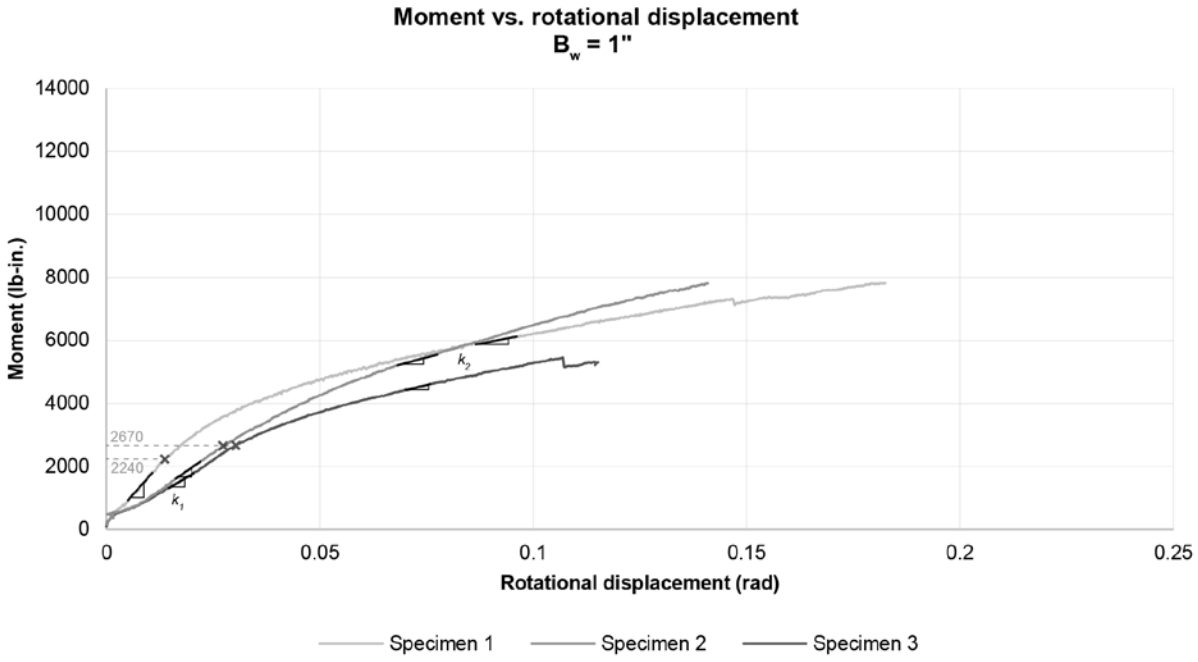

Figure 27. Moment-rotational-displacement curves for the Douglas fir Nuki joint with B_w of 1", as determined by experimental testing.

The slopes in each linear region of elastic and plastic behavior for all prototypes with $B_w = 1$ in. are summarized in Figure 28.

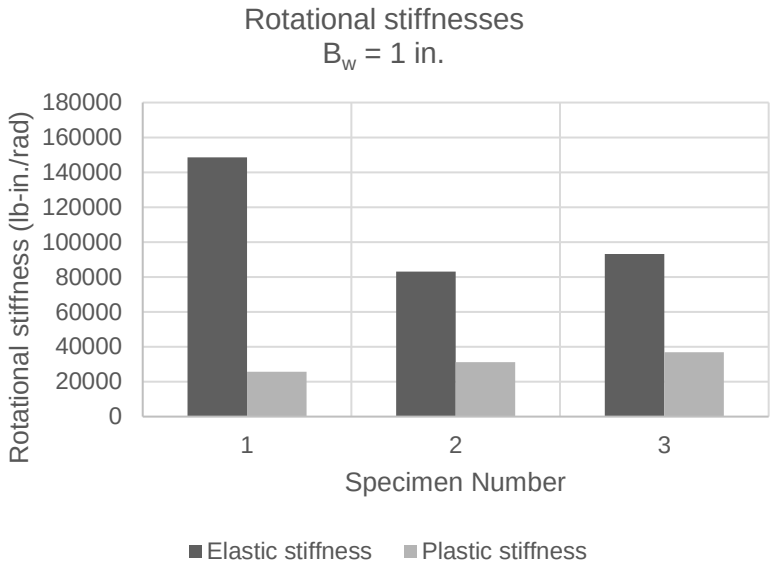

Figure 28. Summary of rotational stiffnesses of all prototypes of the Douglas fir Nuki joint with B_w of 1", as determined by experimental testing.

The elastic stiffness of Specimen 1 is considered an outlier and is not included in future calculations and averages.

Yield moment M_y is approximated for each specimen by observation as the moment at which the elastic stiffness begins to soften, rounded to the nearest 10 lb-in. (Figure 27). Specimen 1 is estimated to have a M_y of 2240 lb-in., while Specimens 2 and 3 are estimated to have a M_y of 2670 lb-in. The M_y of Specimen 1 is discarded as an outlier.

Next, the plots of moment against rotational displacement as extracted from experimental testing of all 3 prototypes of the Douglas fir Nuki joint, $B_w = 1.5$ in., are plotted in Figure 28.

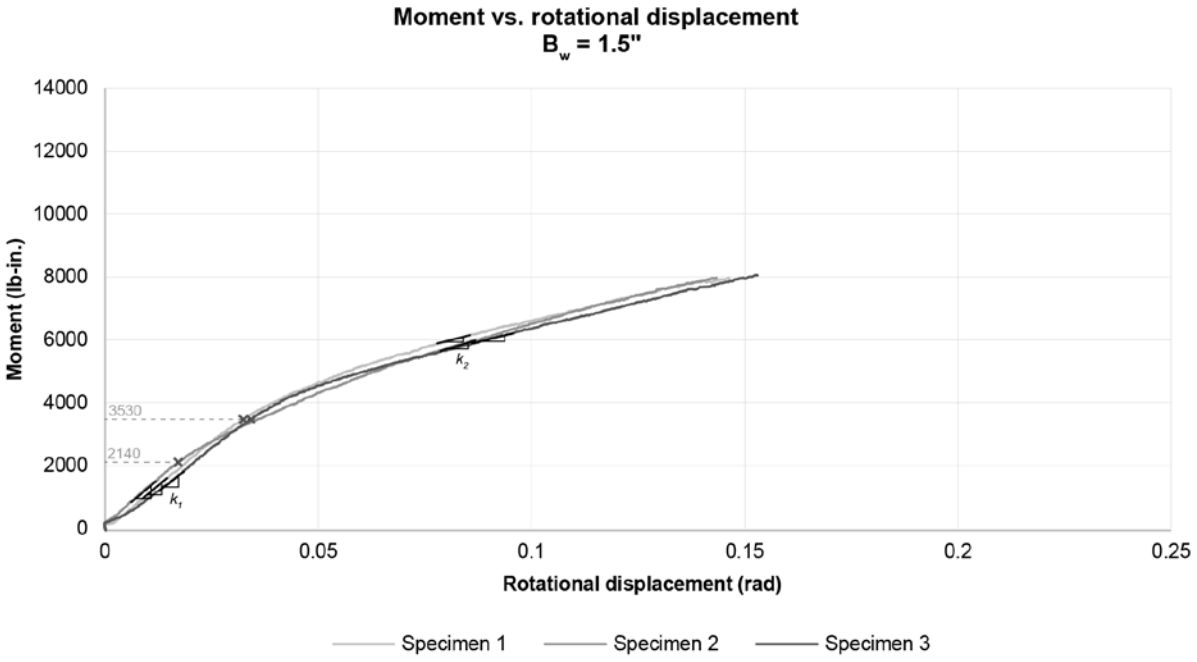

Figure 29. Moment-rotational-displacement curves for the Douglas fir Nuki joint with B_w of 1.5", as determined by experimental testing.

The slopes in each linear region of elastic and plastic behavior for all prototypes with $B_w = 1.5$ in. are summarized in Figure 30.

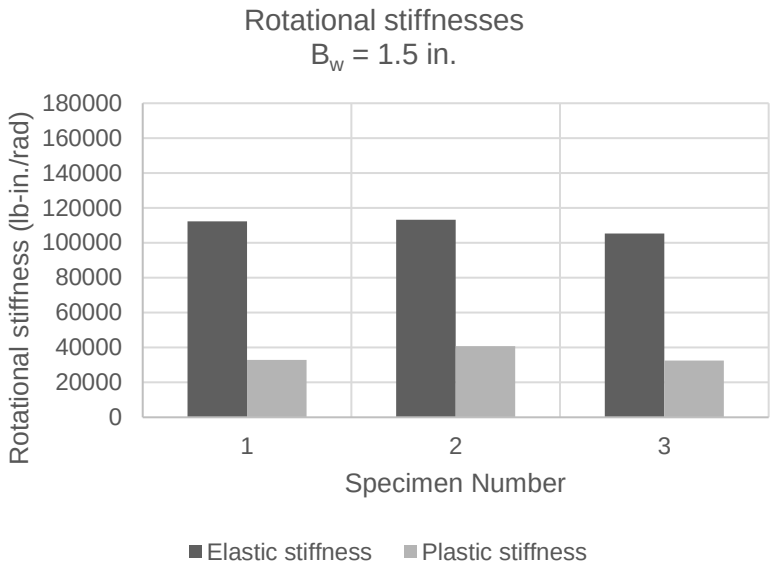

Figure 30. Summary of rotational stiffnesses of all prototypes of the Douglas fir Nuki joint with B_w of 1.5", as determined by experimental testing.

Yield moment M_y is approximated for each specimen by observation as the moment at which the elastic stiffness begins to soften, rounded to the nearest 10 lb-in. (Figure 28). Specimens 1 and 3 are estimated to have a M_y of 3530 lb-in., while Specimen 2 is estimated to have a M_y of 2140 lb-in. The M_y of Specimen 2 is discarded as an outlier.

The plots for moment against rotational displacement for all prototypes are combined in Figure 31.

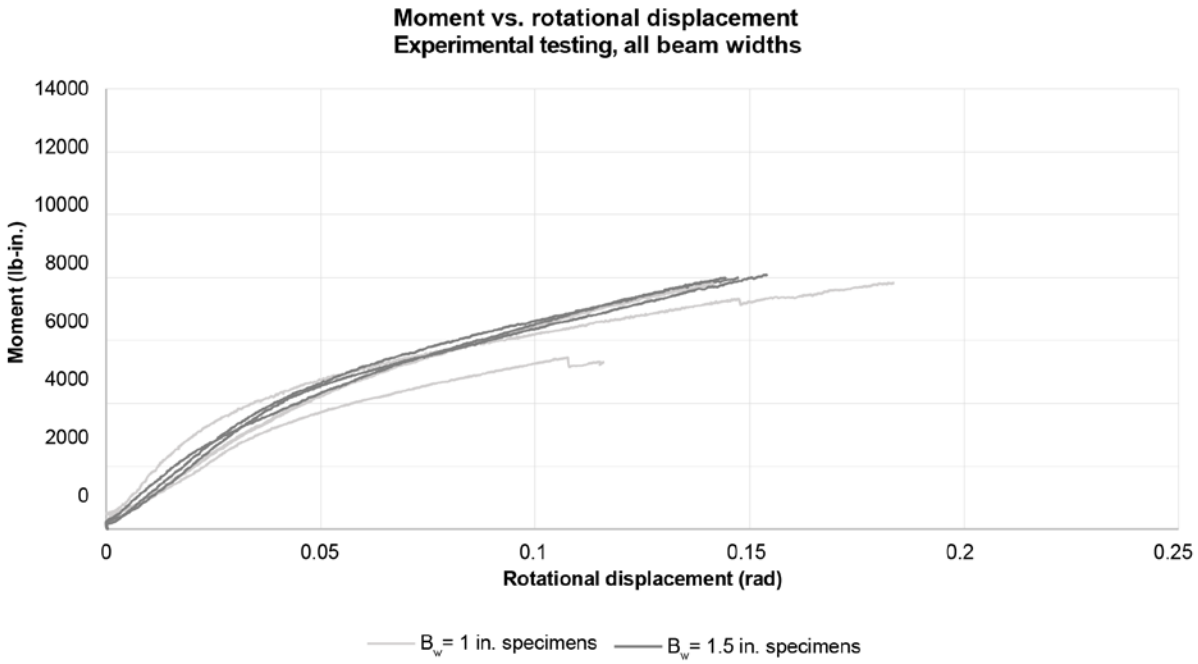

Figure 31. Moment-rotational-displacement curves for the Douglas fir Nuki joint for all beam widths, as determined by experimental testing.

Finally, averages of rotational stiffness values for both beam width dimensions are summarized in Table 7.

Table 7. Summary of mean rotational stiffnesses for the Douglas fir Nuki joint as determined by experimental testing, with outliers removed.

	Elastic stiffness	Plastic stiffness
$B_w = 1$ in.	Mean = 88,100 lb-in./rad (Std dev = 7200 lb-in./rad) Specimens 2, 3 of $B_w = 1$ in.	Mean = 31,300 lb-in./rad (Std dev = 5600 lb-in./rad) Specimens 1, 2, 3 of $B_w = 1$ in.
$B_w = 1.5$ in.	Mean = 110,300 lb-in./rad (Std dev = 4200 lb-in./rad) Specimens 2, 3, 6 of $B_w = 1.5$ in.	35,400 lb-in./rad (Std dev = 4700 lb-in./rad) Specimens 2, 6 of $B_w = 1.5$ in.
% increase in stiffness from $B_w = 1$ in. to $B_w = 1.5$ in.	25%	13%

4.2.3 Comparison of results

The plots of moment against rotational displacement as determined by both analytical and experimental methods for the Douglas fir Nuki joint are plotted in Figure 32 for $B_w = 1$ in. and in Figure 33 for $B_w = 1.5$ in.

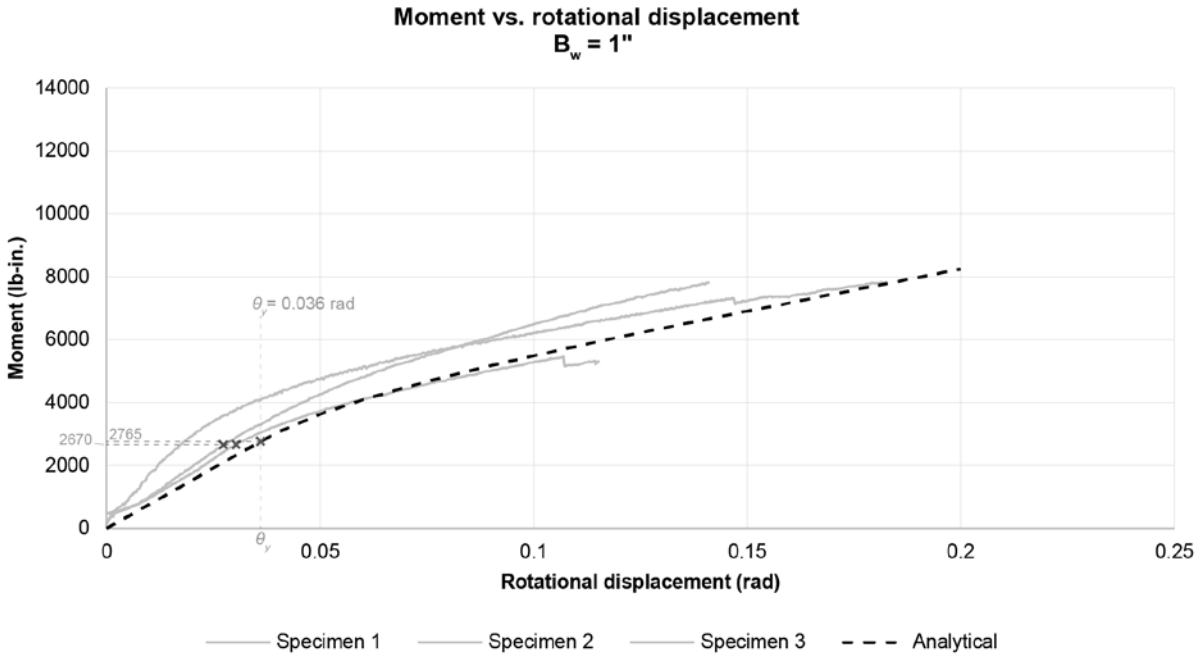

Figure 32. Comparison of moment-rotational-displacement curves using different methods for the Douglas fir Nuki joint with a B_w of 1".

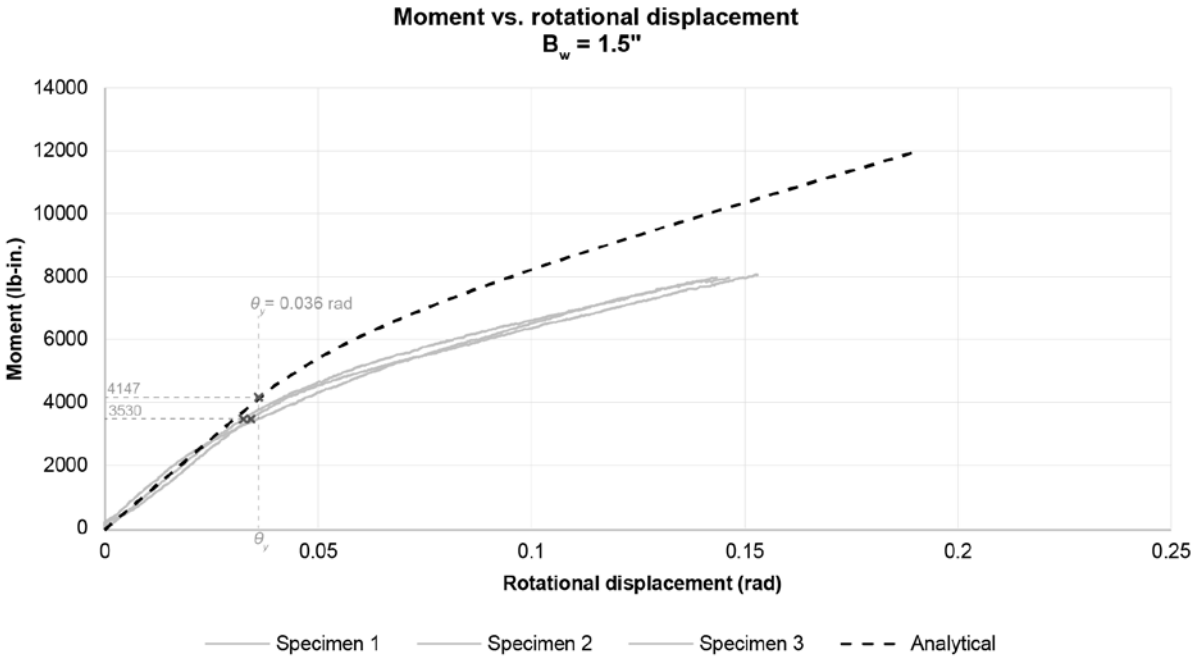

Figure 33. Comparison of moment-rotational-displacement curves using different methods for the Douglas fir Nuki joint with a B_w of 1.5".

A comparison of the slopes in each linear region of elastic and plastic behavior is plotted in Figure 34.

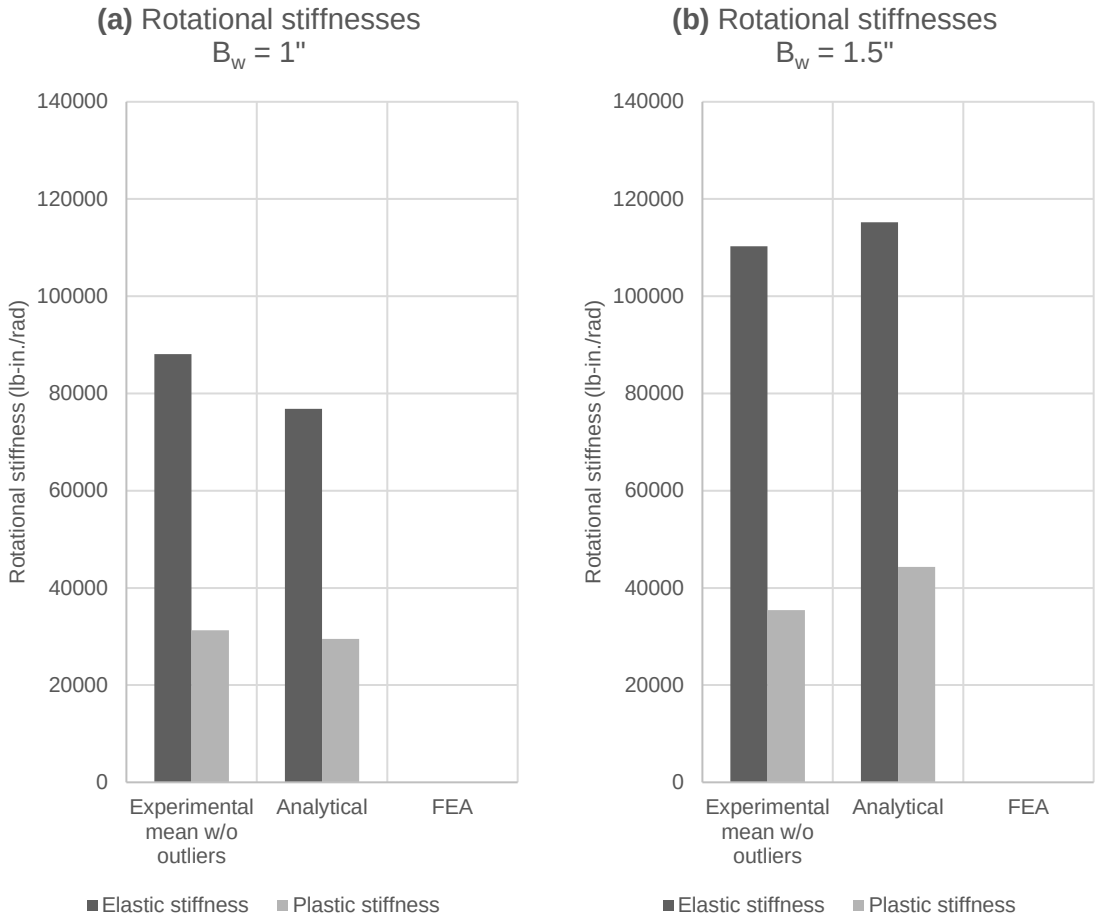

Figure 34. Comparison of rotational stiffnesses of the Douglas fir Nuki joint as determined by different methods, with (a) B_w of 1" and (b) B_w of 1.5". FEA was not carried out for these Douglas fir prototypes.

A numerical tabulation of these stiffnesses is presented in Table 8.

Table 8. Comparison of rotational stiffnesses of the Douglas fir Nuki joint as determined by different methods.

	$B_w = 1$ in.		$B_w = 1.5$ in.	
	Elastic stiffness [lb-in./rad]	Plastic stiffness [lb-in./rad]	Elastic stiffness [lb-in./rad]	Plastic stiffness [lb-in./rad]
Experimental mean, outliers removed	88,100	31,300	110,300	35,400
Analytical model	76,800 [-13%]	29,500 [-6%]	115,200 [+4%]	44,300 [+25%]

[%] = % difference from experimental mean

A comparison of the percentage increases in stiffness from increasing beam width is presented in Table 9.

Table 9. Comparison of percentage increases in stiffness between B_w of 1" and B_w of 1.5" of the Douglas fir Nuki joint as determined by different methods.

	Elastic stiffness	Plastic stiffness
Experimental model	25%	13%
Analytical model	50%	50%

Finally, a comparison of My values is presented in Table 10.

Table 10. Comparison of yield moment between models of the Douglas fir Nuki joint.

	$B_w = 1$ in.	$B_w = 1.5$ in.
Experimental mean, outliers removed	2670 lb-in.	3530 lb-in.
Analytical model	2765 lb-in. [+4%]	4147 lb-in. [+17%]

[%] = % difference from experimental mean

4.3 Results: glulam prototypes

The results for the prototypes made with glulam are summarized below.

4.3.1 Analytical results

The $M(\theta)$ plots as determined by the analytical model of the glulam Nuki joint are charted in Figure 35.

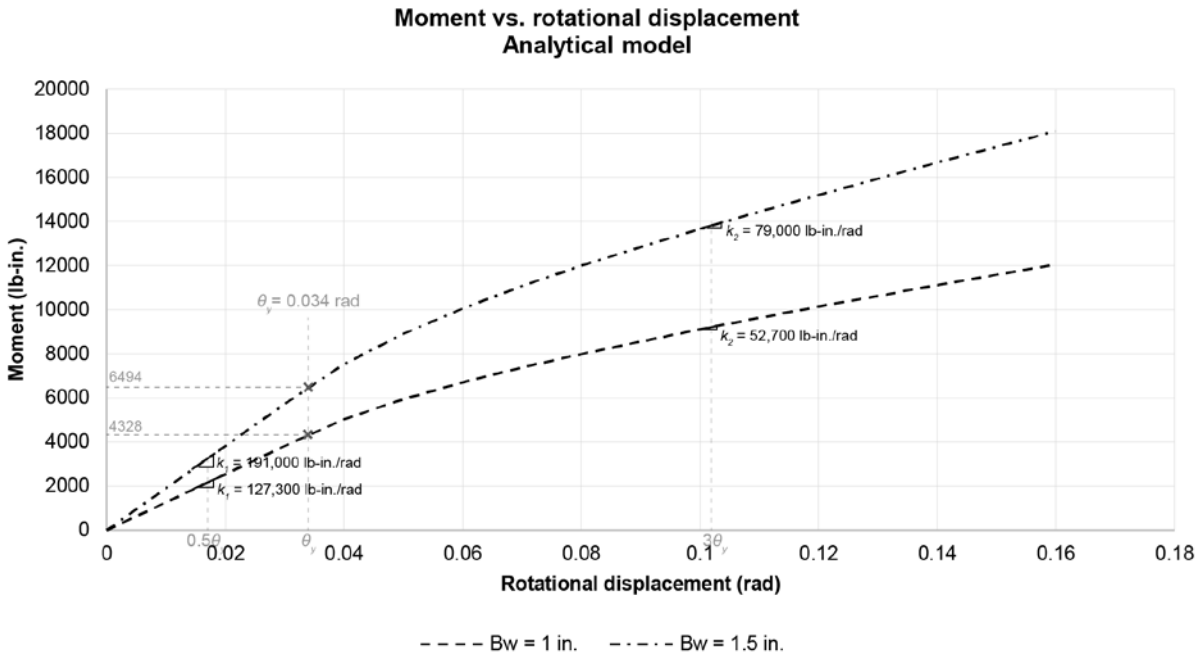

Figure 35. Moment-rotational-displacement curve for the glulam Nuki joint determined by the analytical model.

The slopes in each linear region of elastic and plastic behavior are extracted and summarized in Table 11.

Table 11. Summary of rotational stiffnesses for the glulam Nuki joint as determined by the analytical model.

	Elastic stiffness	Plastic stiffness
$B_w = 1$ in.	127,300 lb-in./rad	52,700 lb-in./rad
$B_w = 1.5$ in.	191,000 lb-in./rad	79,000 lb-in./rad
% increase in stiffness from $B_w = 1$ in. to $B_w = 1.5$ in.	50%	50%

Yield angle can be computed as $\theta_y = \tan^{-1}\left(\frac{\varepsilon_y B_d}{C_d/2}\right)$ according to the model established in Section 3.2, and yield moment M_y is the corresponding moment at $\theta = \theta_y$. Yield moment is 4328 lb-in. and 6494 lb-in. for $B_w = 1$ in. and $B_w = 1.5$ in., respectively.

4.3.2 Experimental results

Scans of the tested beam elements showing embedment are provided in Appendix 2.

The plots of moment against rotational displacement as extracted from experimental testing of all 6 prototypes of the glulam Nuki joint, $B_w = 1$ in., are plotted in Figure 36.

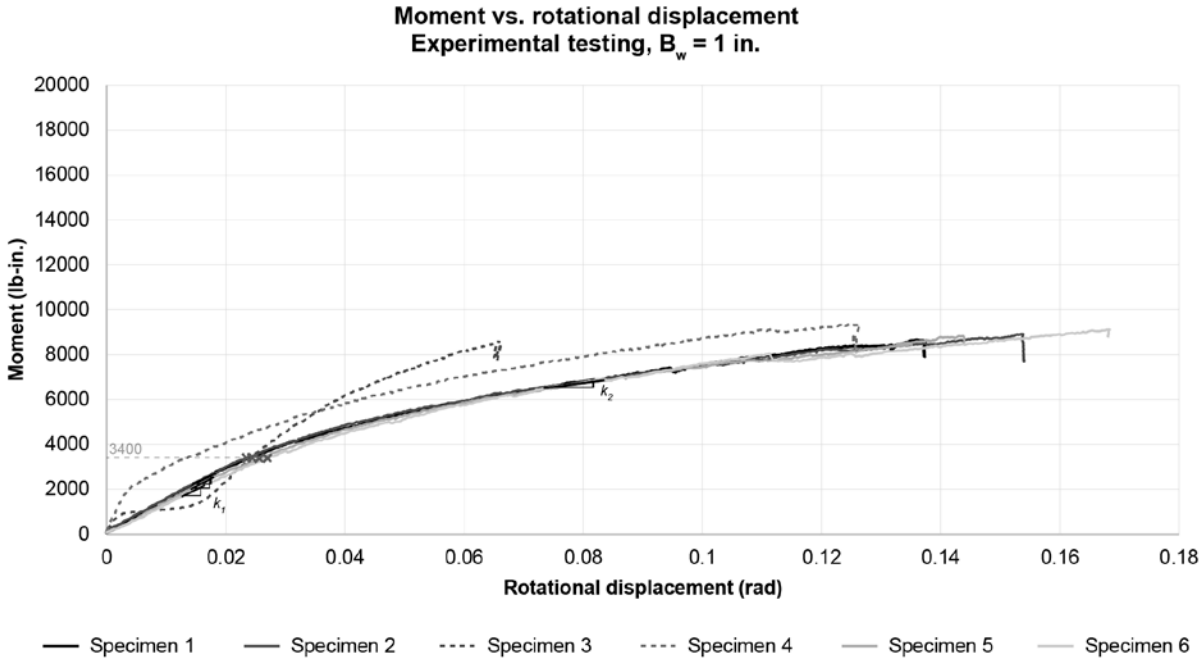

Figure 36. Moment-rotational-displacement curves for the glulam Nuki joint with B_w of 1", as determined by experimental testing.

The slopes in each linear region of elastic and plastic behavior for all prototypes with $B_w = 1$ in. are summarized in Figure 37.

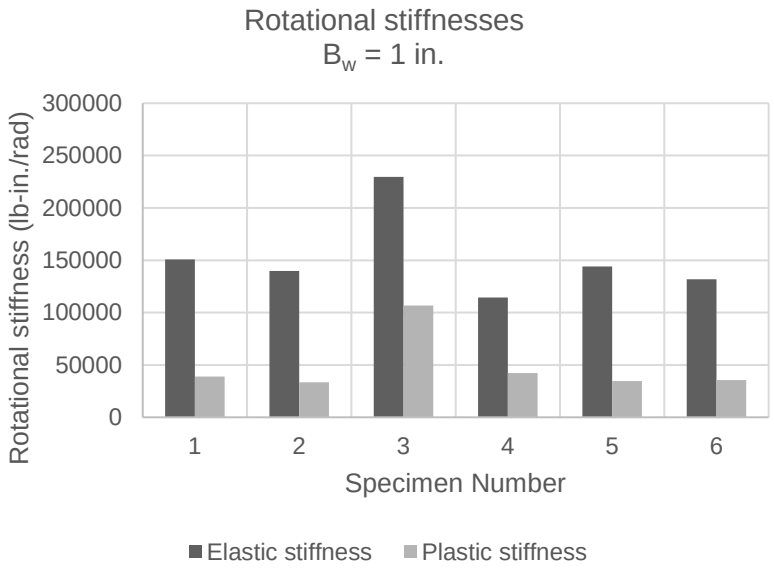

Figure 37. Summary of rotational stiffnesses of all prototypes of the glulam Nuki joint with B_w of 1", as determined by experimental testing.

Specimens 3 and 4 (dashed lines in Figure 36) exhibit abnormal behavior. They are considered outliers and are not considered for the rest of the study.

Yield moment M_y is approximated for each specimen by observation as the moment at which the elastic stiffness begins to soften, rounded to the nearest 10 lb-in. (Figure 36). All specimens remaining after removing outliers (Specimens 1, 2, 5, 6) are estimated to have a M_y of 3400 lb-in.

The plots of moment against rotational displacement as extracted from experimental testing of all 6 prototypes of the glulam Nuki joint, $B_w = 1.5$ in., are plotted in Figure 38.

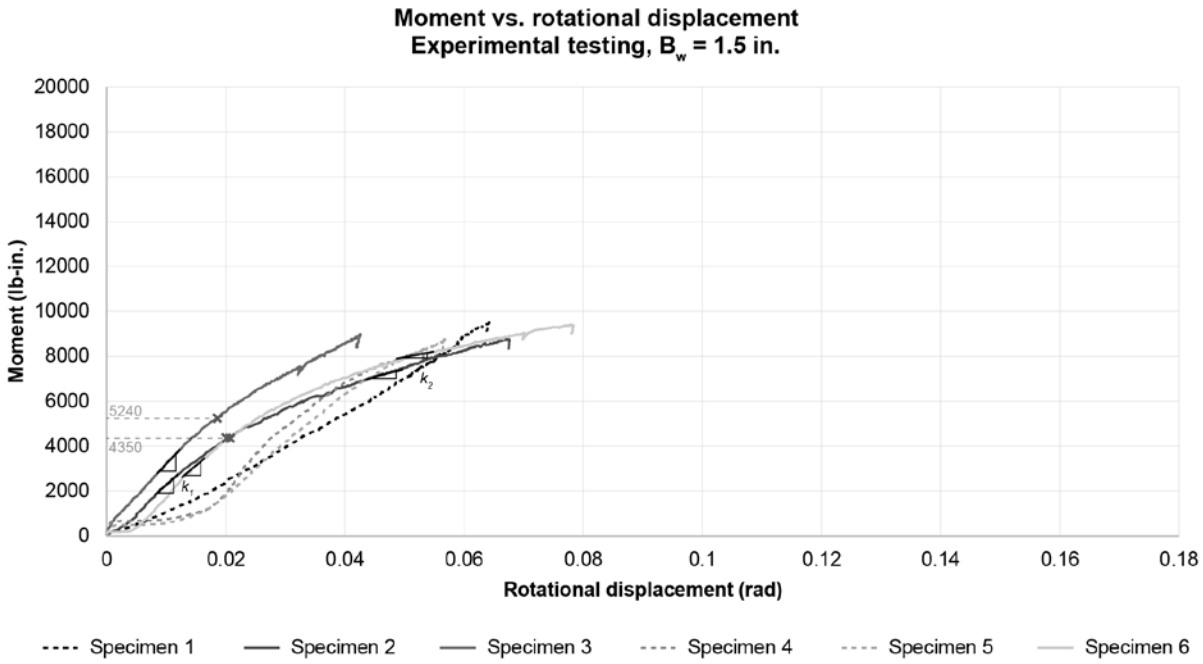

Figure 38. Moment-rotational-displacement curves for the glulam Nuki joint with B_w of 1.5", as determined by experimental testing.

The slopes in each linear region of elastic and plastic behavior for all prototypes with $B_w = 1.5$ in. are summarized in Figure 39.

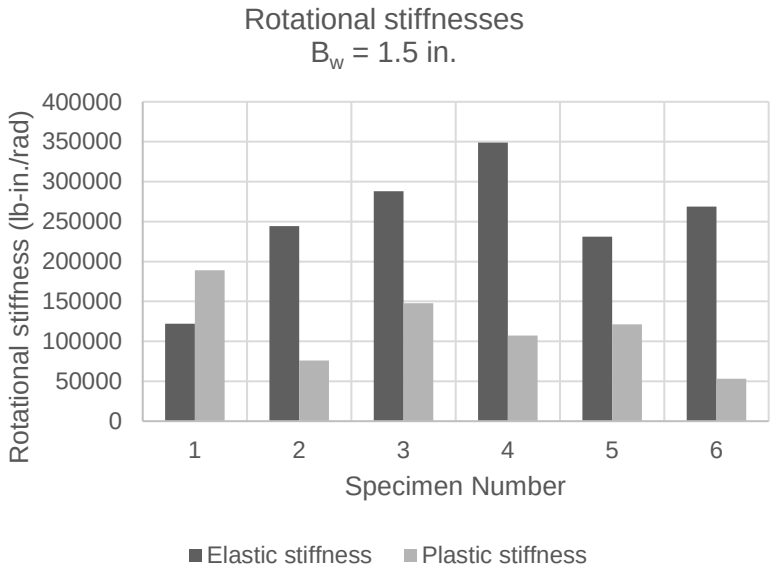

Figure 39. Summary of rotational stiffnesses of all prototypes of the glulam Nuki joint with B_w of 1.5", as determined by experimental testing.

Specimens 1, 4, and 5 qualitatively exhibit abnormal behavior (dashed lines in Figure 38). They are considered outliers and are not considered for the rest of the study. Furthermore, it can be seen that the loading of Specimen 3 was stopped before reaching a secondary stiffness, so its initially reported Stiffness 2 value is not used.

Yield moment M_y is approximated for each specimen by observation as the moment at which the elastic stiffness begins to soften, rounded to the nearest 10 lb-in. (Figure 38). Specimens 2 and 6 are estimated to have a M_y of 4350 lb-in., and Specimen 3 is estimated to have a M_y of 5240 lb-in. The average M_y of these specimens is 4650 lb-in.

The plots for moment against rotational displacement for all beam widths are combined in Figure 40.

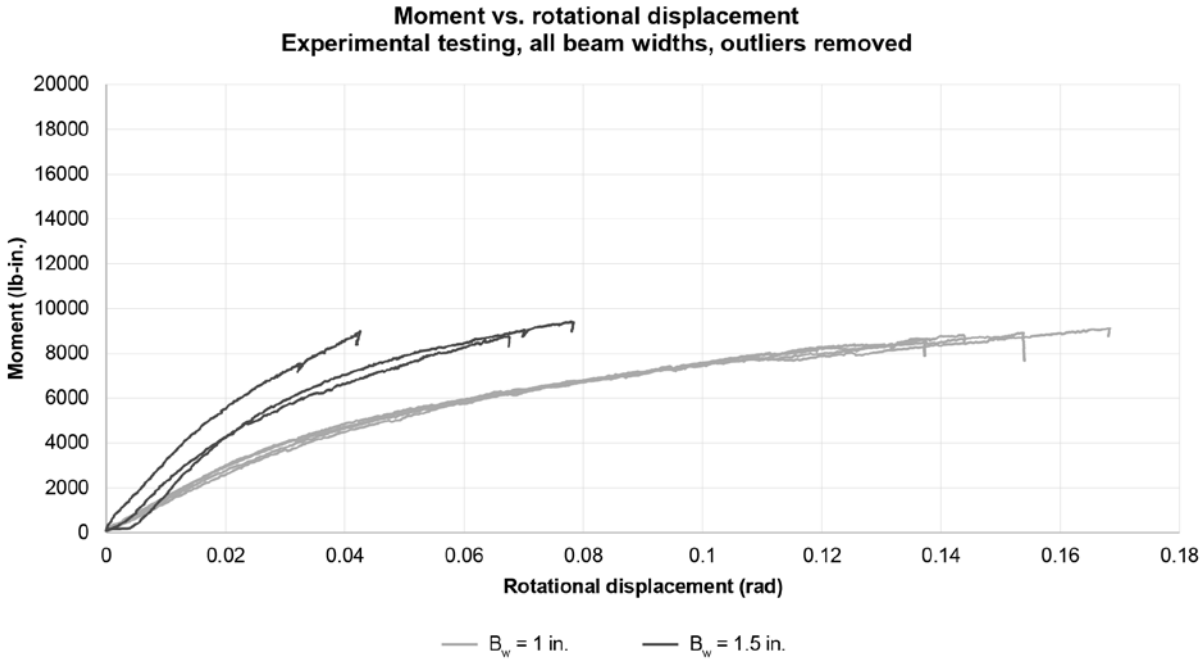

Figure 40. Moment-rotational-displacement curves for the glulam Nuki joint for all beam widths, as determined by experimental testing, with outliers removed.

Finally, averages of rotational stiffness values for both beam width dimensions are summarized in Table 12.

Table 12. Summary of mean rotational stiffnesses for the glulam Nuki joint as determined by experimental testing, with outliers removed.

	Elastic stiffness	Plastic stiffness
$B_w = 1$ in.	Mean = 141,600 lb-in./rad (Std dev = 7900 lb-in./rad) Specimens 1, 2, 5, 6 of $B_w = 1$ in.	35,500 lb-in./rad (Std dev = 2400 lb-in./rad) Specimens 1, 2, 5, 6 of $B_w = 1$ in.
$B_w = 1.5$ in.	267,100 lb-in./rad (Std dev = 21,900 lb-in./rad) Specimens 2, 3, 6 of $B_w = 1.5$ in.	64,400 lb-in./rad (Std dev = 16,100 lb-in./rad) Specimens 2, 6 of $B_w = 1.5$ in.
% increase in stiffness from $B_w = 1$ in. to $B_w = 1.5$ in.	89%	81%

4.3.3 Numerical results

The $M(\theta)$ plots as determined by the FEA model of the glulam Nuki joint are charted in Figure 41.

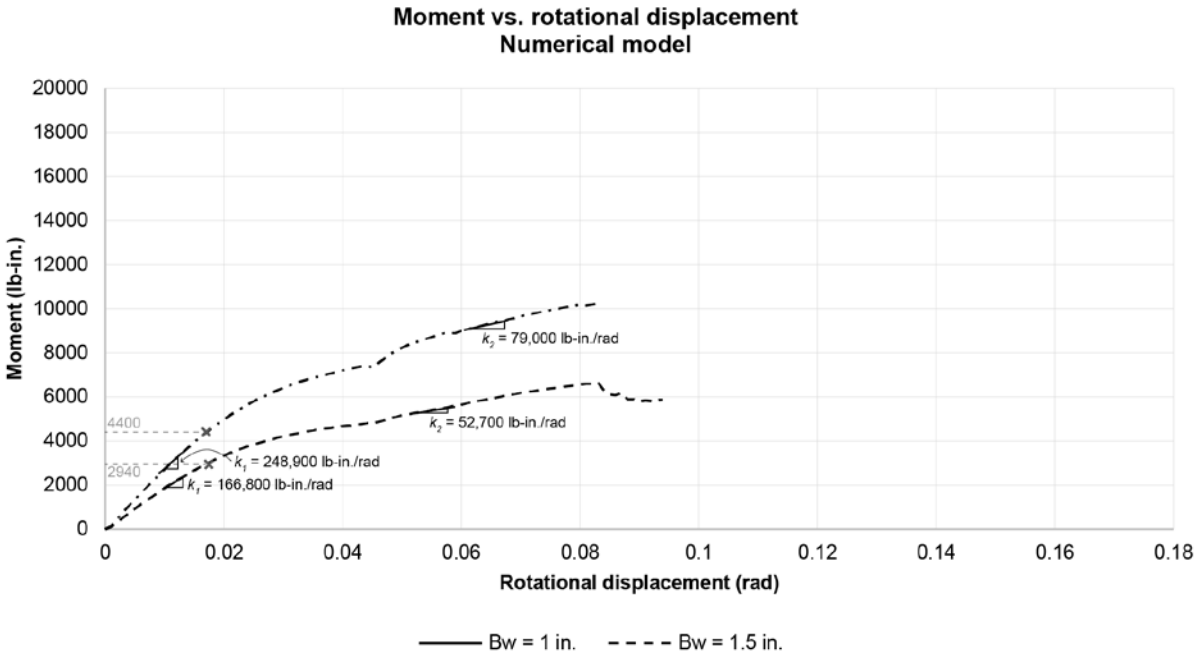

Figure 41. Moment-rotational-displacement curve for the glulam Nuki joint determined by the FEA model.

The slopes in each linear region of elastic and plastic behavior are extracted and summarized in Table 13.

Table 13. Summary of rotational stiffnesses for the glulam Nuki joint as determined by the FEA model.

	Elastic stiffness	Plastic stiffness
$B_w = 1$ in.	166,800 lb-in./rad	45,200 lb-in./rad
$B_w = 1.5$ in.	248,900 lb-in./rad	59,700 lb-in./rad
% increase in stiffness from $B_w = 1$ in. to $B_w = 1.5$ in.	49%	32%

Yield moment M_y is approximated by observation as the moment at which the elastic stiffness begins to soften, rounded to the nearest 10 lb-in. (Figure 41). M_y is estimated to be 2940 lb-in. and 4400 lb-in. for $B_w = 1$ in. and $B_w = 1.5$ in., respectively.

4.3.4 Comparison of results

The plots of moment against rotational displacement as determined by both analytical and experimental methods for the glulam Nuki joint are plotted in Figure 42 for $B_w = 1$ in. and in Figure 43 for $B_w = 1.5$ in.

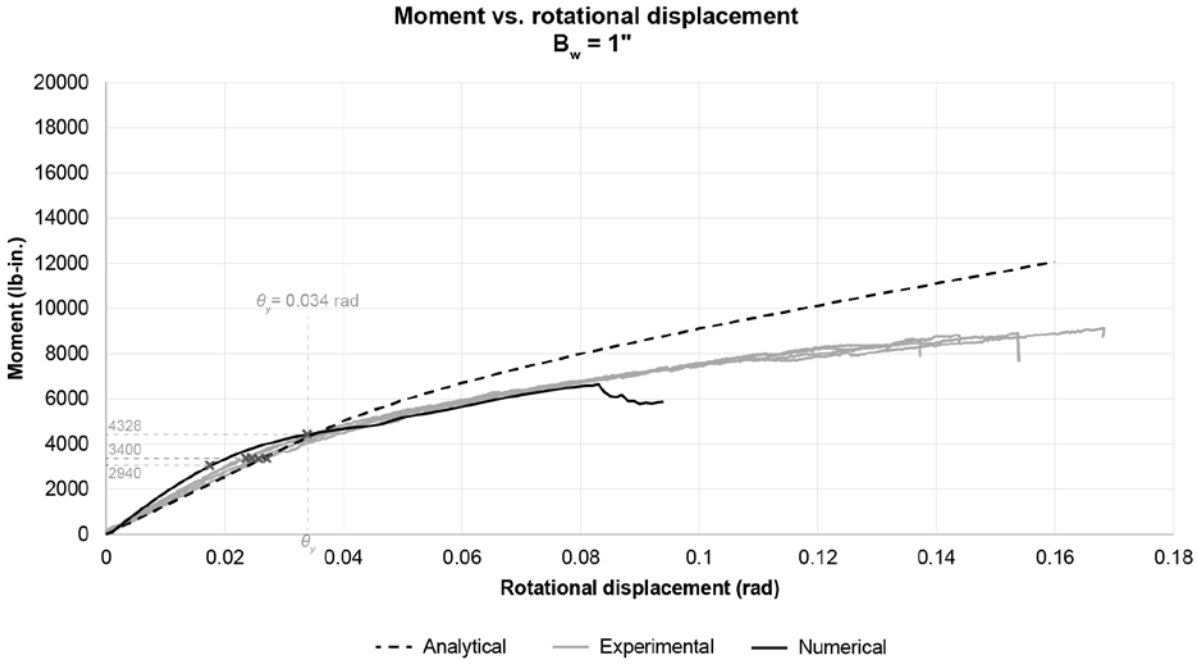

Figure 42. Comparison of moment-rotational-displacement curves using different methods for the glulam Nuki joint with a B_w of 1".

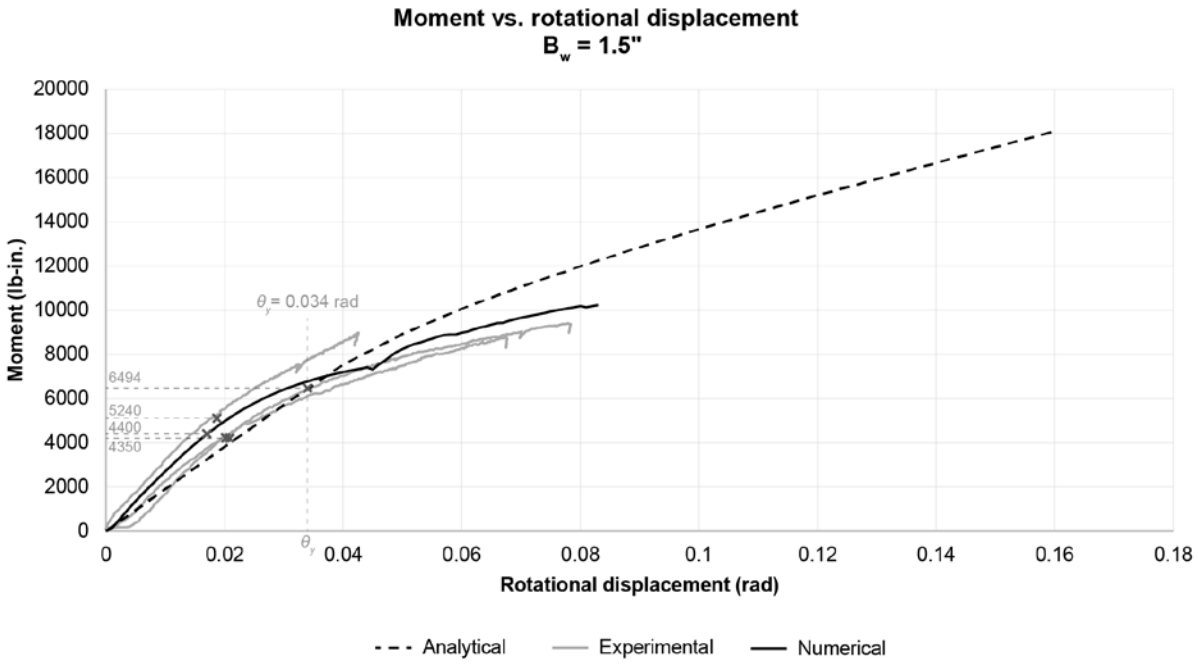

Figure 43. Comparison of moment-rotational-displacement curves using different methods for the glulam Nuki joint with a B_w of 1.5".

A comparison of the slopes in each linear region of elastic and plastic behavior is plotted in Figure 44.

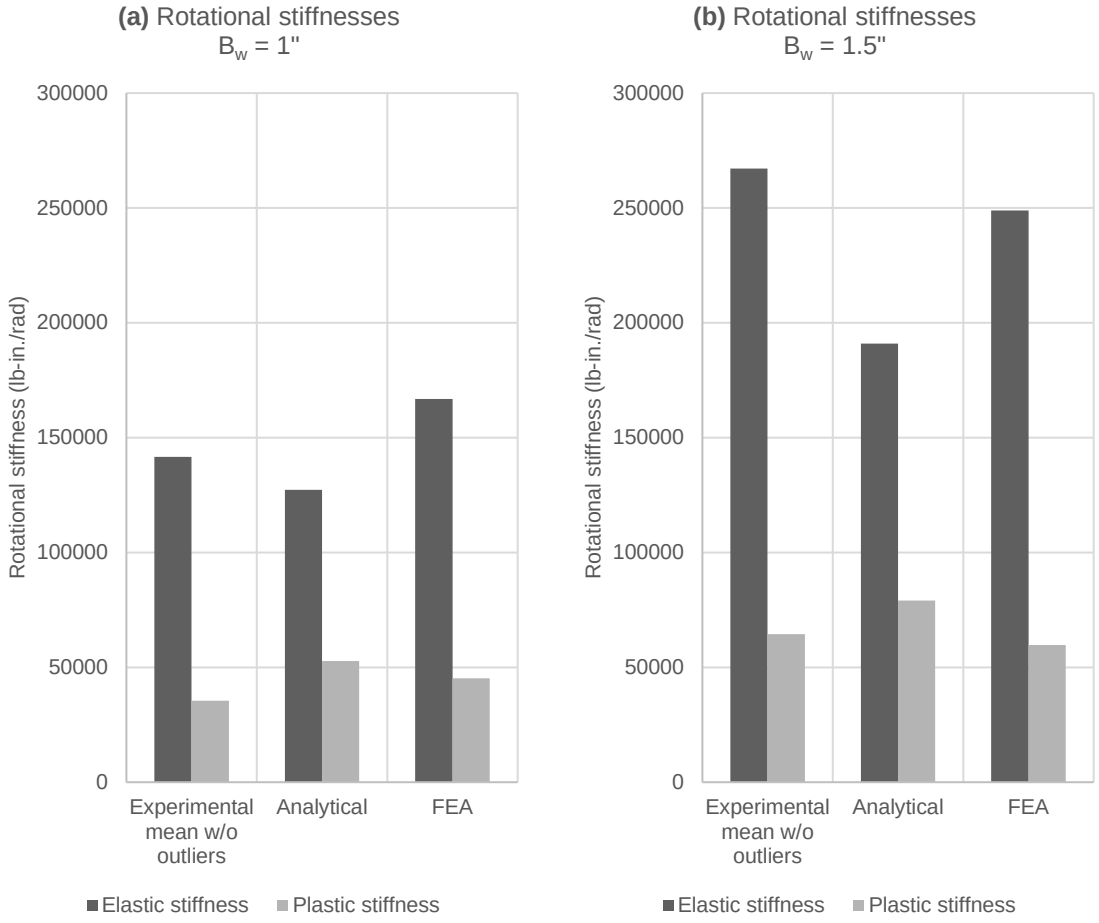

Figure 44. Comparison of rotational stiffnesses of the glulam Nuki joint as determined by different methods, with (a) B_w of 1" and (b) B_w of 1.5".

A numerical tabulation of these stiffnesses is presented in Table 14.

Table 14. Comparison of rotational stiffnesses of the glulam Nuki joint as determined by different methods.

	$B_w = 1$ in.		$B_w = 1.5$ in.	
	Elastic stiffness [lb-in./rad]	Plastic stiffness [lb-in./rad]	Elastic stiffness [lb-in./rad]	Plastic stiffness [lb-in./rad]
Experimental mean, outliers removed	141,600	35,500	267,100	64,400
Analytical model	127,300 [-10%]	52,700 [+48%]	191,000 [-29%]	79,000 [+23%]
Numerical model	166,800 [+18%]	45,200 [+27%]	248,900 [-7%]	59,700 [-7%]

[%] = % difference from experimental mean

A comparison of the percentage increases in stiffness from increasing beam width is presented in Table 15.

Table 15. Comparison of percentage increases in stiffness between B_w of 1" and B_w of 1.5" of the glulam Nuki joint as determined by different methods.

	Elastic stiffness	Plastic stiffness
Experimental model	89%	81%
Analytical model	50%	50%
Numerical model	49%	32%

A comparison of M_y values is presented in Table 16.

Table 16. Comparison of yield moment between models of the glulam Nuki joint.

	$B_w = 1$ in.	$B_w = 1.5$ in.
Experimental mean, outliers removed	3400 lb-in.	4647 lb-in.
Analytical model	4328 lb-in. [+27%]	6494 lb-in. [+40%]
Numerical model	2940 lb-in. [-14%]	4400 lb-in. [-5%]

[%] = % difference from experimental mean

A qualitative comparison of embedment among all three methods for the glulam Nuki joint is shown in Figure 45.

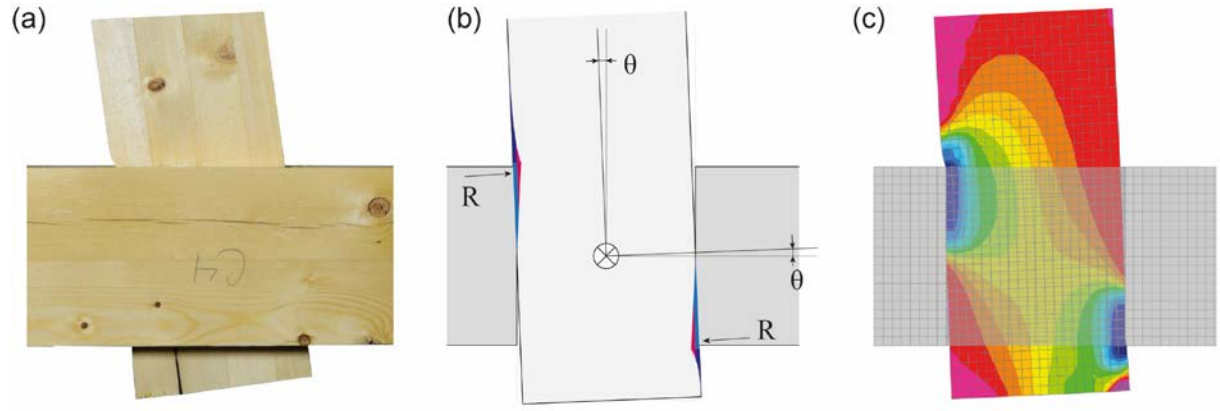

Figure 45. Comparison of embedment in the glulam Nuki joint as determined by (a) experimental testing, (b) analytical model, and (c) FEA model. Images by Daniel Landez, Jan Brütting, and Aliz Fischer; figure assembled by Aliz Fischer.

4.4 Discussion

4.4.1 Comparison of overall moment-rotational-displacement behavior

With the exception of outlier experimental prototypes which were not considered, the results from all models generally demonstrated the expected bilinear behavior: an initial elastic stiffness followed by a softening to a secondary stiffness in their plots of moment against rotational displacement (Figure 32, Figure 33, Figure 42, Figure 43).

In Figure 43, the numerical model shows an unexpected kink in the plastic region around a rotational displacement of about 0.045 radians. Collaborator Benshun Shao reasons that this kink occurs when the governing normal contact force shifts from the beam element against the inside face of the mortise to the beam element against the outside face of the column; in other words, it occurs when the beam element rotates enough to "turn the corner" of the mortise. One possible explanation for why the transition is not smoother might be that the mesh size is not fine enough.

The analytical model was deliberately selected to capture embedment with additional exponential-shaped length as shown in Figure 45 (b). This behavior was evident in both experimental testing and FEA testing (Figure 45 (a) and (c), respectively).

4.4.2 Comparison of stiffness values

Table 8 and Table 14 show the quantitative comparisons of stiffness across different methods. In the Douglas fir models (Table 8), the analytical model usually predicted within 20% of experimental values, except for plastic stiffness for $B_w = 1.5$ in. which would not typically be used in design. In the glulam models (Table 14), the analytical model tended to underestimate the elastic stiffness demonstrated in the experimental models and overestimate the plastic stiffness demonstrated in the experimental models. The numerical model's stiffness values were within 30% of experimental stiffness values.

Possible explanations for the higher discrepancies due to limitations in experimental testing are also discussed in Section 4.4.5.

4.4.3 Comparison of relative increases in rotational stiffness from increasing beam width

Table 9 and Table 15 show the percentage increases in stiffness demonstrated by increasing beam width by 50% (from 1 in. to 1.5 in.). The expected value, 50%, is reflected in the analytical model.

The experimental prototypes in Douglas fir do not show as much of a stiffness increase (Table 9), but this phenomenon is an acknowledged limitation of the experimental testing results and is discussed more in Section 4.4.5.

On the other hand, in the glulam experimental prototypes (Table 15), the mean elastic stiffness and mean plastic stiffness increase by 80-90%. This is an unexpectedly high increase and suggest that experimental testing could be improved by implementing the suggestions discussed in Section 4.4.5.

The FEA models for the glulam prototypes demonstrate an increase in stiffness of 49% for elastic stiffness but only an increase of 32% for plastic stiffness due to an increase in beam width (Table 15). The kink mentioned in Section 4.4.1 may have affected the perceived measure of the plastic stiffness; improving the model to smooth out the kink might produce a relationship between plastic stiffness and beam width closer to expected.

4.4.4 Comparison of yield moment values

In the Douglas fir joints, the analytical model predicted a yield moment within 20% of the experimental values (Table 10). In the glulam joints, the analytical model's predictions were farther off, over-predicting the yield moment by 30-40% of the experimental values (Table 16). Because M_y predictions from the analytical model would be used for design, it is important to note this pattern of over-prediction to apply adequate safety factors.

4.4.5 Limitations in experimental testing

The most evident limiting factor was the quantity and quality of specimens examined for experimental testing. For example, in the Douglas fir prototypes (for which 3 prototypes were fabricated and tested for each beam width), it is difficult to identify the differences between beam widths when all moment-rotational-displacement curves are plotted together as in Figure 31. After throwing out outliers, only two prototypes were considered for some stiffness values, which may have contributed to a high standard deviation for elastic stiffness of $B_w = 1\ \text{in.}$ (Table 7).

For the glulam studies, twice as many prototypes for each beam width were fabricated and tested (6 each), but again unexpected testing behavior resulted in necessarily removing several outlier specimens for each beam width. After removing outliers, the behavior and stiffnesses of the remaining $B_w = 1\ \text{in.}$ prototypes seemed to be fairly consistent (Table 12), but the behavior and stiffnesses for the remaining $B_w = 1.5\ \text{in.}$ prototypes were more sparse and varied (Table 12).

The quantity of specimens produced and tested were limited by time and resources.

Possible explanations for abnormal testing behavior include 1) variations in the material as timber is a heterogeneous material, 2) changes in humidity and temperature between fabrication and testing that may have changed the moisture content in the timber. Both possibilities can lead to

variations in tightness of fit between beam and column elements. Based on the presence of outlier behavior in both the hand-crafted Douglas fir prototypes and CNC-ed glulam prototypes, it is likely that these variations in fit may not necessarily be alleviated by digital fabrication. It is worth noting that a variation of the Nuki joint includes a hardwood wedge driven in to improve the tightness of fit between beam and column elements; this additional component might offer a more normalized tightness of fit across prototypes.

4.5 Conclusions

The rotational stiffness of the Nuki joint was determined using analytical, experimental, and numerical methods. Two types of materials (Douglas fir and glulam) and two types of fabrication methods (hand carpentry and digital fabrication) were used for experimental prototypes.

The moment-rotational-displacement plots for all models demonstrated bilinear behavior; an initial elastic region was observed before wood crushing perpendicular to the grain caused the joint to enter a plastic region of reduced stiffness. The analytical model tended to under-predict elastic stiffness values while over-predicting plastic stiffness values and yield moments. The numerical model for the glulam prototypes predicted absolute stiffness values within 30% of experimental values. The expected relationship between beam width and rotational stiffness as predicted by the analytical model was not ideally observed in the experimental prototypes; the Douglas fir prototypes did not exhibit as much increase in rotational stiffness from beam width as expected, while the glulam prototypes exhibited a larger increase than expected. The numerical simulations were more successful at capturing the expected relationship between beam width and rotational stiffness.

While the overall bilinear behavior may emerge as the only consistent match among the three models, it is important to note the difficulty of simultaneously tuning all three models to each other while also acknowledging the limitations and inconsistencies faced in experimental testing. Given the unpredictable behavior that resulted from the small sample size of experimental prototypes, the sensitivity to material properties, wood imprefections, and fabrication tolerances was a clear takeaway from the comparisons between models. The ability to adopt large-scale statistical models, such as probability distributions of material imperfections, would be important before the rotational stiffness could be implemented into building codes. As a result, it is recommended that future work expands the scope of testing for more statistical certainty and consistency given the variations inherent in both the timber material and the fabrication methods.

To demonstrate the possible benefits of being able to design with the rotational stiffness provided by the Nuki joint, the following chapters outline example procedures of designing with the Nuki joint for gravity and lateral systems. The analytical model developed in this chapter is used for design.

5 Nuki joint in modern timber construction

In the previous chapter, the rotational stiffness of the Nuki joint was characterized using three methods. This chapter uses the analytical model from the previous chapter to characterize the rotational stiffness of Nuki joints on beams with varying dimensions, enabling the Nuki joint to be used in structural design of gravity systems.

A gravity frame design problem is presented for varying spans. Gravity frame designs for 3 different systems are compared: 1) steel beam, 2) glulam beam supported by beam hangers, and 3) glulam beam supported by Nuki joints.

5.1 Modern mass timber connections

A variety of connection details are available in the present-day mass timber market. For example, the NDS 2018, the structural code for timber in the United States, lists dowel-type fasteners, split ring and shear plate connectors, and timber rivets as the three main types of mechanical connections (American Wood Council 2017).

In modern mass timber construction, larger scale buildings sometimes demand more custom variations of these connections. Usually, these connections use metallic connection components to join timber elements (Figure 1, Figure 2, Figure 3, Figure 4, Figure 5).

Rather than design a mechanical connection from scratch, in this chapter a pre-engineered beam hanger is used to represent an example conventional metallic connection for timber systems. Several pre-engineered beam hanger system products are available in the market. These products are typically considered nominally pinned and are designed using shear capacity. For this particular study, the beam hanger catalog from Mass Timber Connections (MTC) is used as a reference for selecting beam hanger products (MTC Solutions 2020).

5.2 Structural assumptions

A single beam spanning between two columns is considered. The beam section and its connections at each end to the supporting column are designed. Table 17 summarizes the constraints assumed.

Table 17. Assumptions for comparative study.

Glulam properties*	Modulus of elasticity parallel to grain E_0	1,960,000 psi
	Maximum flexural stress $\sigma_{max,mat}$	4400 psi
	Maximum shear stress $\tau_{max,mat}$	320 psi
	Yield strain ε_y	0.017
Loading conditions	Spans L (center-to-center)	10 ft, 15 ft, 20 ft, 25 ft
	Tributary width b_{trib}	$L/2$
	Dead load D	20 psf
	Live load L	40 psf
	Self-weight neglected.	
Dimensions	Column size	20 in. x 20 in.

*Modulus of elasticity parallel to grain value set to match the value used for glulam prototypes in Section 4. Maximum flexural and shear stress values are rounded from Nordic Lam Beams and Headers product catalog (Nordic Engineered Wood 2013).

To calculate the demand on beams supporting the area loads for both service and strength checks, the linear loads $q_{unfactored}$ and $q_{factored}$ are converted to linear loads accordingly:

$$q_{unfactored} = b_{trib}(D + L) \quad (54)$$

$$q_{factored} = b_{trib}(1.2D + 1.6L) \quad (55)$$

5.3 Beam design

The comparative results for frames designed with beam hangers and frames designed with Nuki joints are summarized in Figure 46. As will be discussed in greater detail, the rotational restraint provided by the Nuki joints enable lower midspan moment and subsequently smaller material quantities. Details on the design method for each are provided in the following subsections.

a) Beam hangers

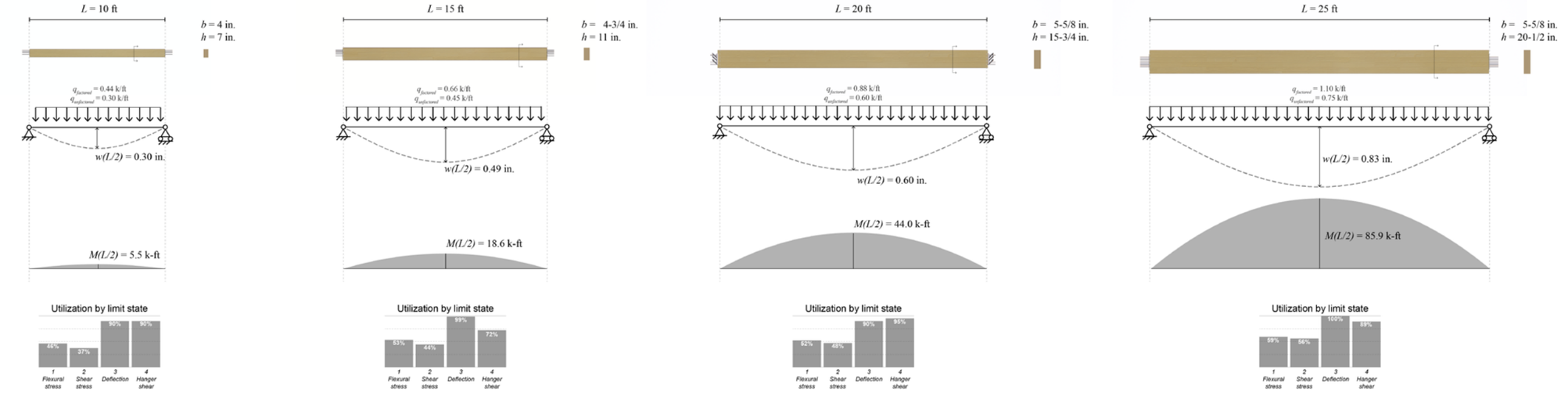

b) Nuki joints

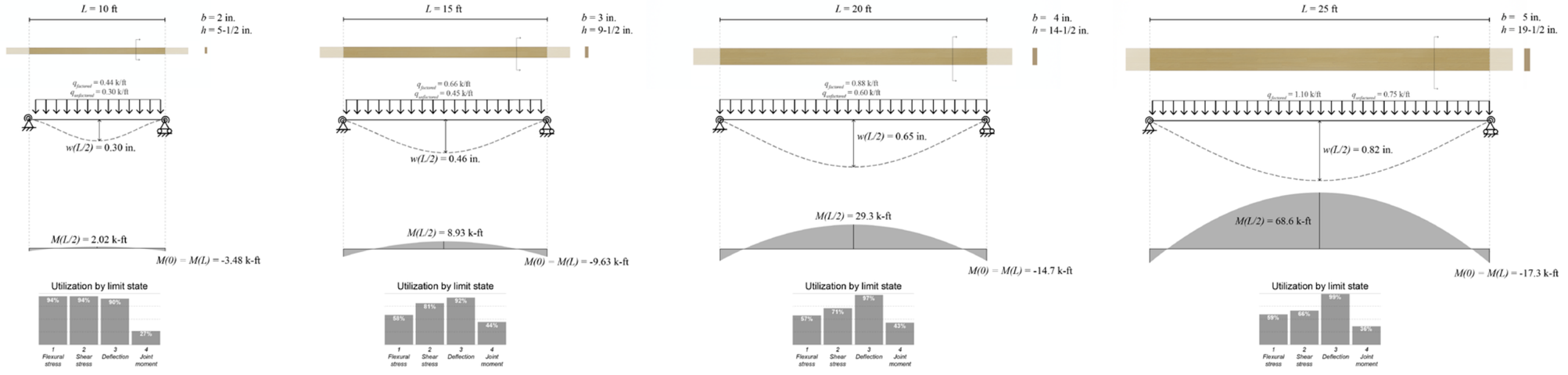

Figure 46. Final beam designs for varying spans using different connection types.

5.3.1 Steel beam design

As a benchmark comparison, steel beam sections for each span were designed with shear connections (nominally pinned) using the Cross Section Optimizer in Karamba3D (Presinger and Bollinger+Grohmann 2018). The sizes are provided in Table 18.

Table 18. Steel profiles selected for each span.

Span $\boldsymbol{L}$	Steel profile	Area
10 ft	W4x13	3.83 in.^{2}
15 ft	W6x20	5.87 in.^{2}
20 ft	W8x40	11.7 in.^{2}
25 ft	W10x68	20.0 in.^{2}

5.3.2 Beam design with beam hangers

The beam hanger is nominally pinned on each end. The limit states for beam design are set out in Table 19.

Table 19. Limit states for the design of a timber beam supported at both ends with a connection of shear capacity V_{allow}.

	Limit state	Condition
1	Maximum flexural stress	$\sigma_{max,beam} < \sigma_{max,mat}$
2	Maximum shear stress	$\tau_{max,beam} < \tau_{max,mat}$
3	Maximum deflection	$w_{max} < \frac{L}{360}$
4	Joint shear reaction	$V_{max} < V_{allow}$

$\sigma_{max,mat}$ and $\tau_{max,mat}$ are glulam material properties listed in Table 17, L is the span, and V_{allow} is a property of the beam hanger product. All other values are determined through beam analysis as follows.

Due to the loading conditions, maximum shear is known to occur at the supports. Thus, for limit state 4, we have

$$V_{max} = V(0) = V(L) = \frac{q_{factored} L}{2} \tag{56}$$

Due to the loading conditions, the maximum bending moment is known to occur at midspan:

$$M_{max} = M\left(\frac{L}{2}\right) = \frac{q_{factored} L^2}{8} \tag{57}$$

The expressions for V_{max} and M_{max} can be used to determine $\sigma_{max,beam}$ and $\tau_{max,beam}$ to check the limit states 1 and 2.

For limit state 1: substituting M_{max} from equation (57), $y = \frac{h}{2}$, and $I = \frac{1}{12}bh^3$ (from assuming a rectangular cross-section) into $\sigma = \frac{My}{I}$, we have

$$\sigma_{max,beam} = \frac{\frac{q_{factored}L^2}{8} \times \frac{h}{2}}{\frac{1}{12}bh^3} = \frac{3q_{factored}L^2}{4bh^2} \quad (58)$$

For limit state 2: substituting $V = V_{max} = \frac{q_{factored}L}{2}$, $Q = \frac{bh}{2} * \frac{h}{4}$, $I = \frac{1}{12}bh^3$, and $t = b$ into $\tau = \frac{VQ}{It}$, we have

$$\tau_{max,beam} = \frac{q_{factored}L}{2} \times \frac{bh^2}{8} \times \frac{1}{\frac{1}{12}b^2h^3} = \frac{3q_{factored}L}{4bh} \quad (59)$$

Finally, for limit state 3: due to the loading conditions, maximum displacement is known to occur at midspan:

$$w_{max} = w\left(\frac{L}{2}\right) = \frac{5q_{unfactored}L^4}{384E_0I} \quad (60)$$

To design the beam, first a beam hanger product was selected for the beam based on the magnitude of shear reaction. The shear reactions and selected beam hanger products determined for each span and associated load are summarized in Table 20.

Table 20. Beam hangers selected for each span based on shear demand. Beam hanger product design values provided in MTC Solutions catalog (MTC Solutions 2020), and S-P-F glulam was assumed.

Span L	Shear demand V_{max}	MTC beam hanger product	Fasteners per connector	Shear capacity V_{allow}
10 ft	2.20 k	Ricon S VS 140x60	7 (primary member) + 7 (secondary member)	2.44 k
15 ft	4.95 k	Ricon S VS 200x80	16 (primary member) + 16 (secondary member)	6.89 k
20 ft	8.80 k	Megant 310x100	34	9.28 k
25 ft	13.8 k	Ricon XL 390x80	30 (primary member) + 30 (secondary member)	15.5 k

Each beam hanger product has a minimum beam section associated with it. This minimum section is initially selected as the beam dimensions and the other limit states checked (Table 21). If needed, the section size is increased slightly to meet the other limit state criteria.

Table 21. Selected beam sections for each span based on beam hanger selection.

Span L	Beam section width b	Beam section depth h
10 ft	4 in.	7 in.
15 ft	4-3/4 in.	11 in.*
20 ft	5-5/8 in.	15-3/4 in.
25 ft	5-5/8 in.**	20-1/2 in.**

*Increased from Ricon S VS 200x60 h_{min} of 9-1/2 in. to meet other limit state criteria.

**Increased from Ricon XL 390x80 b_{min} of 4-3/4 in. and h_{min} of 17 in. to meet other limit state criteria.

Key values for the design criteria of each span from the cross-section selections are provided in Table 22. Moment, displacement, and utilization are also diagrammed in Figure 46(a).

Table 22. Key values for beam design of varying spans supported by beam hangers.

Limit state	Value	Span L			
		10 ft	15 ft	20 ft	25 ft
1 Maximum flexural stress	$\sigma_{max,beam}$	2020 psi	2325 psi	2270 psi	2618 psi
	$\sigma_{max,mat}$	4400 psi	4400 psi	4400 psi	4400 psi
	Utilization	46 %	53 %	52 %	59 %
2 Maximum shear stress	$\tau_{max,beam}$	118 psi	142 psi	149 psi	179 psi
	$\tau_{max,mat}$	320 psi	320 psi	320 psi	320 psi
	Utilization	37 %	44 %	47 %	56 %
3 Maximum deflection	w_{max}	0.30 in.	0.49 in.	0.60 in.	0.83 in.
	$\frac{L}{360}$	0.33 in.	0.50 in.	0.67 in.	0.83 in.
	Utilization	90 %	99 %	90 %	100 %
4 Joint shear reaction	V_{max}	2.20 k	4.95 k	8.80 k	13.8 k
	V_{allow}	2.44 k	5.89 k	9.28 k	15.5 k
	Utilization	90 %	72 %	95 %	89 %

In all spans, either deflection or joint shear reaction (limit states 3 or 4) govern the design of the beam section. For 15 ft and 25 ft spans, the beam section had to be increased from the minimum required by the selected beam hanger in order to meet the deflection limit. The 15 ft span has a relatively low utilization because it happens to have a shear demand that falls in an intermediate range between shear capacities of beam hanger products for S-P-F glulam.

5.3.3 Beam design with Nuki joints

The rotational stiffness of the Nuki joint depends on the dimensions of the timber elements, so the timber beam must be designed in parallel with the rotational stiffness. In this chapter, the rotational stiffness of the Nuki joint in the elastic region is called k, and the width and depth of the beam are called b and h, respectively. A summary of the limit states for beam design are provided in Table 23.

Table 23. Limit states for the design of a timber beam supported at both ends with a Nuki joint of known rotational stiffness k.

Limit state	Condition
1 Maximum flexural stress	$\sigma_{max,beam} < \sigma_{max,mat}$
2 Maximum shear stress	$\tau_{max,beam} < \tau_{max,mat}$
3 Maximum deflection	$w_{max} < \frac{L}{360}$
4 Joint moment reaction	$M_R < M_{allow}$ where $M_{allow} = k\theta_y$ and $\theta_y = \tan^{-1}\left(\frac{\varepsilon_y h}{C_d/2}\right)$

$\sigma_{max,mat}$ and $\tau_{max,mat}$ are glulam material properties listed in Table 17.

k is determined by the analytical model of the Nuki joint presented in Section 3.2. The model as originally presented assumes some "ended embedment length" representing the length past which the beam pierces through the far face of the column. For this case study, it is assumed that the beam stops at the far face of the column, meaning an "ended embedment length" of 0. All terms related to ended embedment (subscript *e*) presented in Section 3.2 are taken as 0.

Because of the iterative nature of the design process, it was more convenient to generate a reference to look up rotational stiffnesses associated with different section sizes. These values were generated using a variation of the script presented in Appendix 1 (where ended embedment terms are eliminated and beam dimensions b and h are input for B_w and B_d, respectively) and is provided in Figure 47. The values are valid for a column depth C_d of 20 inches. (C_d is the column dimension parallel to the main axis of the beam; see Figure 18).

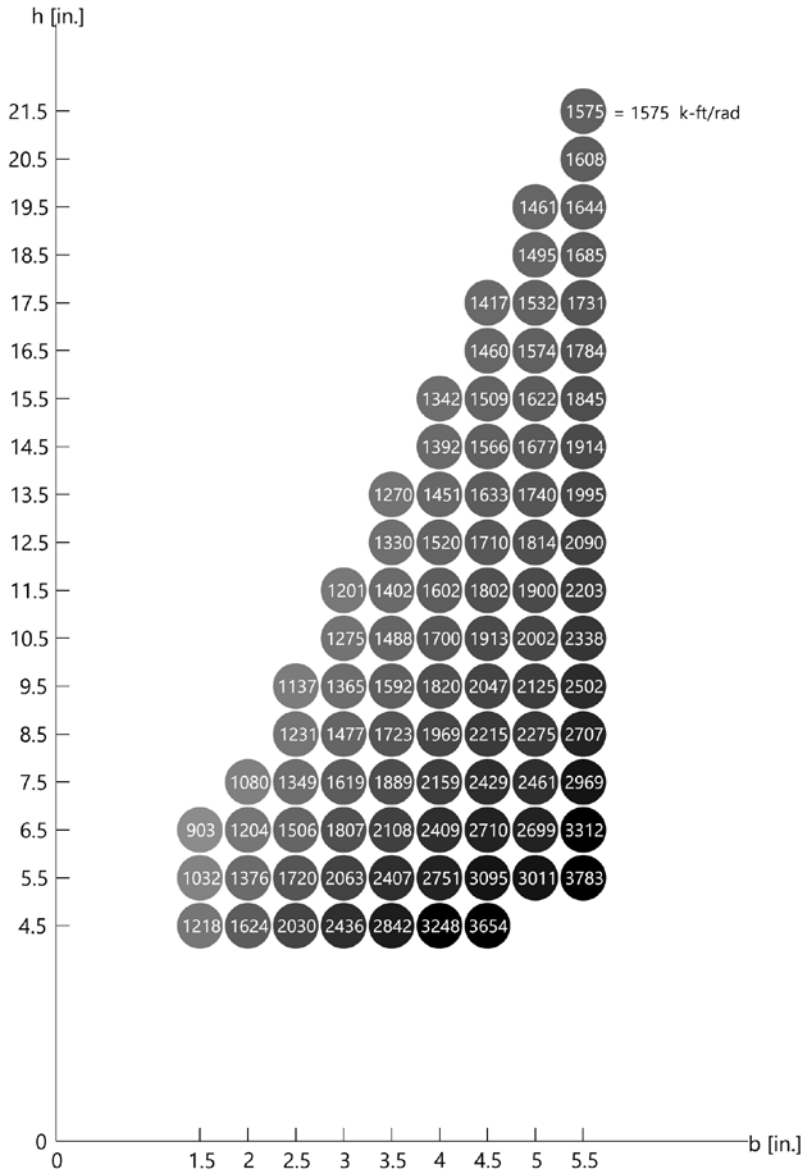

Figure 47. Graphic to assist with Nuki beam and joint design, charting the rotational stiffness of Nuki joints of varying widths b and depths h in the range $1 \leq h/b < 4$. These values are calculated for a column depth (dimension $C_{d,}$ based on terminology of Section 3) of 20 inches.

To design the beam section, an initial size is selected, and k is determined by looking up the value in Figure 47. Unlike the beam hanger design process in Section 5.3.2, the beam supported by Nuki joints cannot be designed using the governing design values for a simply supported beam. With a known elastic rotational stiffness k supporting the beam and the loading conditions set out in Table 17, the moment reactions and midspan deflection of the beam supported on

both ends with a Nuki joint can be derived; details of these calculations are set out in Appendix 3. For ease of reference, the expressions for moment reaction magnitude M_R and midspan deflection $w\left(\frac{L}{2}\right)$ are repeated here, with a substitution of $E = E_0$ to indicate the stiffness parallel to grain as the relevant bending stiffness in glulam:

$$M_R = \frac{qL^3}{24\left(\frac{E_0 I}{k} + \frac{L}{2}\right)} \tag{61}$$

$$w\left(\frac{L}{2}\right) = \frac{L}{E_0 I}\left(-E_0 I\frac{M_R}{2k} - \frac{M_R L}{8} + \frac{qL^3}{128}\right) \tag{62}$$

Since it is known that $w_{max} = w\left(\frac{L}{2}\right)$ under these loading conditions, these expressions can be directly used to evaluate limit states 3 and 4 from Table 23.

Due to the loading conditions, maximum shear is known to occur at the supports with $V(0) = V(L) = \frac{q_{factored}L}{2}$, and the maximum bending moment is known to occur either at the supports or the midpoint: $M_{max} = \max\left(M_R, M\left(\frac{L}{2}\right)\right)$.

These expressions for V_{max} and M_{max} can be used to determine $\sigma_{max,beam}$ and $\tau_{max,beam}$ to check the limit states 1 and 2 from Table 23.

For limit state 1: substituting $M = M_{max} = \max\left(M_R, M\left(\frac{L}{2}\right)\right)$, $y = \frac{h}{2}$, and $I = \frac{1}{12}bh^3$ assuming a rectangular cross-section into $\sigma = \frac{My}{I}$, we have

$$\sigma_{max,beam} = \frac{\max\left(M_R, M\left(\frac{L}{2}\right)\right) \times \frac{h}{2}}{\frac{1}{12}bh^3} = \frac{\max\left(M_R, M\left(\frac{L}{2}\right)\right) \times 6}{bh^2} \tag{63}$$

For limit state 2: substituting $V = \frac{q_{factored}L}{2}$, $Q = \frac{bh}{2} * \frac{h}{4}$, $I = \frac{1}{12}bh^3$, and $t = b$ into $\tau = \frac{VQ}{It}$, we have

$$\tau_{max,beam} = \frac{q_{factored}L}{2} \times \frac{bh^2}{8} \times \frac{1}{\frac{1}{12}b^2h^3} = \frac{3q_{factored}L}{4bh} \tag{64}$$

For a given span, a range of cross-sections (i.e. combinations of b and h) can be determined. This set of cross-sections can be generated by finding the minimum h for several values of b that satisfies all limit states. A set of cross-sections that meet all limit states for each span, within the range $1 \leq h/b < 4$ and at the increments provided in Figure 47, are listed in Table 24.

Table 24. Beam cross sections satisfying all limit states when supported by Nuki joints. Cross sections are selected by picking a width b and finding the minimum depth h that satisfies all limit states, within the range $1 \leq h/b < 4$.

Span $\boldsymbol{L}$	Beam section width $\boldsymbol{b}$	Beam section depth $\boldsymbol{h}$	Beam section area $\boldsymbol{bh}$	Beam section ratio $\boldsymbol{h/b}$
10 ft	2 in.	5-1/2 in.	11.0 $in.^2$	2.75
	3 in.	4-1/2 in.	13.5 $in.^2$	1.50
15 ft	3 in.	9-1/2 in.	28.5 $in.^2$	3.17
	3-1/2 in.	8-1/2 in.	29.8 $in.^2$	2.43
	4-1/2 in.	7-1/2 in.	33.8 $in.^2$	1.67
20 ft	4 in.	14-1/2 in.	58.0 $in.^2$	3.63
	4-1/2 in.	13-1/2 in.	60.8 $in.^2$	3.00
	5-1/2 in.	12-1/2 in.	68.8 $in.^2$	2.27
25 ft	5 in.	19-1/2 in.	97.5 $in.^2$	3.9

The data displayed in Table 24 make it clear that for each span, the most materially efficient sections (lowest section area bh) are the narrow and tall sections (high h/b). However, there is a practical limit on how narrow a section can be due to lateral torsional buckling concerns, which is why a maximum h/b of 4 was set using engineering judgment when selecting cross-sections for each span.

Table 25 lists the cross-section dimensions ultimately selected for each span supported by Nuki joints, along with the section's rotational stiffness.

Table 25. Selected beam sections for each span based on limit states for beams supported by Nuki joints, and associated rotational stiffness in the elastic region.

Span $\boldsymbol{L}$	Beam section width $\boldsymbol{b}$	Beam section depth $\boldsymbol{h}$	Rotational stiffness $\boldsymbol{k}$
10 ft	2 in.	5-1/2 in.	1376 k-ft/rad
15 ft	3 in.	9-1/2 in.	1365 k-ft/rad
20 ft	4 in.	14-1/2 in.	1392 k-ft/rad
25 ft	5 in.	19-1/2 in.	1461 k-ft/rad

Key values for the design criteria of each span from the cross-section selections are provided in Table 26. Moment, displacement, and utilization are also diagrammed in Figure 46(b).

Table 26. Key values for beam design of varying spans supported by Nuki joints.

Limit state	Value	Span $\boldsymbol{L}$			
		10 ft	15 ft	20 ft	25 ft
1 Maximum flexural stress	$\sigma_{max,beam}$	4137 psi	2561 psi	2507 psi	2598 psi
	$\sigma_{max,mat}$	4400 psi	4400 psi	4400 psi	4400 psi
	Utilization	94 %	58 %	57 %	59 %
2 Maximum shear stress	$\tau_{max,beam}$	300 psi	261 psi	228 psi	212 psi
	$\tau_{max,mat}$	320 psi	320 psi	320 psi	320 psi
	Utilization	94 %	81 %	71 %	66 %
3 Maximum deflection	w_{max}	0.30 in.	0.46 in.	0.65 in.	0.82 in.
	$\frac{L}{360}$	0.33 in.	0.50 in.	0.67 in.	0.83 in.
	Utilization	90 %	92 %	97 %	99 %
4 Joint moment reaction	M_R	3.48 k-ft	9.63 k-ft	14.7 k-ft	17.4 k-ft
	M_{allow}	12.9 k-ft	22.0 k-ft	34.3 k-ft	48.4 k-ft
	Utilization	27 %	44 %	43 %	36 %

For all spans above 10 ft, deflection (limit state 3) definitively governs the design of the beam section. For the 10 ft span, maximum flexural stress and maximum shear stress (limit states 1 and 2) govern slightly more than deflection.

5.4 Comparing embodied carbon for all gravity frame design methods

In the previous section, varying design methods were used to design a gravity frame for the same span and loading conditions. This section quantifies and compares the embodied carbon of each system.

5.4.1 Assumptions

To calculate the associated embodied carbon for each system, material densities and embodied carbon coefficients must be assumed. The assumed values for respective frame components are provided in Table 27.

Table 27. Material assumptions for calculation of embodied carbon. Embodied carbon coefficients were obtained from Jones and Hammond 2019.

Component	Material	Density	Embodied carbon coefficient
Steel beam profiles	Steel, section (world average)	0.132 kg/in.^{3}	1.55 kg CO2e / kg
Beam hanger fasteners	Steel, wire rod (world average)	0.132 kg/in.^{3}	2.27 kg CO2e / kg
RICON S VS beam hangers	Steel, plate (world average)	0.132 kg/in.^{3}	2.46 kg CO2e / kg
MEGANT beam hangers	Aluminum (world average)	0.0442 kg/in.^{3}	13.1 kg CO2e / kg
Beams	Timber, glulam (no carbon storage)	0.00688 kg/in.^{3}	0.512 kg CO2e / kg

The same column size was used for each gravity frame, so column volumes were omitted. In the Nuki joint systems, the columns are mortised to insert the beams; the volumes of timber beam intersecting the column were excluded from volume calculations.

For the steel beam profiles, volumes of shear connectors were omitted because the amount of additional metallic material was negligible relative to the volume of steel section with a comparable EC coefficient.

For the beam hangers, volumes of hex nuts and washers were omitted.

Volumes for the beam hanger products were not provided by the manufacturer, but sufficient dimensions were presented in the product design guide to estimate volume quantities. Details on these volume estimates of beam hanger products are provided in Appendix 4.

5.4.2 Quantities

Volume and embodied carbon quantities for the 10 ft, 15 ft, 20 ft, and 25 ft spans are presented in Table 28, Table 29, Table 30, and Table 31, respectively. Embodied carbon quantities are shown with perspective renders of each frame design in Figure 48.

Table 28. Quantities of different gravity frame designs for a 10 ft span.

10 ft span	Steel	Beam hanger	Nuki, full section
Beam section	W6x20	4 in. x 7 in.	2 in. x 5-1/2 in.
Timber, glulam area	0 $in.^2$	28 $in.^2$	11 $in.^2$
Steel, section area	3.83 $in.^2$	0 $in.^2$	0 $in.^2$
Steel, section	459.6 $in.^3$	0 $in.^3$	0 $in.^3$
Steel, wire rod	0 $in.^3$	10.5 $in.^3$	0 $in.^3$
Steel, plate	0 $in.^3$	9.8 $in.^3$	0 $in.^3$
Aluminum	0 $in.^3$	0 $in.^3$	0 $in.^3$
Timber, glulam	0 $in.^3$	3360 $in.^3$	1320 $in.^3$
Steel, section	94.0 kg CO2e	0 kg CO2e	0 kg CO2e
Steel, wire rod	0 kg CO2e	2.65 kg CO2e	0 kg CO2e
Steel, plate	0 kg CO2e	3.18 kg CO2e	0 kg CO2e
Aluminum	0 kg CO2e	0 kg CO2e	0 kg CO2e
Timber, glulam	0 kg CO2e	11.8 kg CO2e	4.65 kg CO2e
TOTAL EC	**94.0 kg CO2e**	**18.2 kg CO2e**	**4.65 kg CO2e**

Table 29. Quantities of different gravity frame designs for a 15 ft span.

15 ft span	Steel	Beam hanger	Nuki, full section
Beam section	W4x13	4-3/4 in. x 11 in.	3 in. x 9-1/2 in.
Timber, glulam area	0 $in.^2$	52.25 $in.^2$	28.5 $in.^2$
Steel, section area	5.87 $in.^2$	0 $in.^2$	0 $in.^2$
Steel, section	1057 $in.^3$	0 $in.^3$	0 $in.^3$
Steel, wire rod	0 $in.^3$	46.4 $in.^3$	0 $in.^3$
Steel, plate	0 $in.^3$	18.5 $in.^3$	0 $in.^3$
Aluminum	0 $in.^3$	0 $in.^3$	0 $in.^3$
Timber, glulam	0 $in.^3$	9405 $in.^3$	5130 $in.^3$
Steel, section	216.2 kg CO2e	0 kg CO2e	0 kg CO2e
Steel, wire rod	0 kg CO2e	13.9 kg CO2e	0 kg CO2e
Steel, plate	0 kg CO2e	5.99 kg CO2e	0 kg CO2e
Aluminum	0 kg CO2e	0 kg CO2e	0 kg CO2e
Timber, glulam	0 kg CO2e	33.1 kg CO2e	18.1 kg CO2e
TOTAL EC	**216.2 kg CO2e**	**53.0 kg CO2e**	**18.1 kg CO2e**

Table 30. Quantities of different gravity frame designs for a 20 ft span.

20 ft span	Steel	Beam hanger	Nuki, full section
Beam section	W8x40	5-5/8 in. x 15-3/4 in.	4 in. x 14-1/2 in.
Timber, glulam area	0 $in.^2$	88.6 $in.^2$	58 $in.^2$
Steel, section area	11.7 $in.^2$	0 $in.^2$	0 $in.^2$
Steel, section	2808 $in.^3$	0 $in.^3$	0 $in.^3$
Steel, wire rod	0 $in.^3$	57.3 $in.^3$	0 $in.^3$
Steel, plate	0 $in.^3$	0 $in.^3$	0 $in.^3$
Aluminum	0 $in.^3$	161.0 $in.^3$	0 $in.^3$
Timber, glulam	0 $in.^3$	21,263 $in.^3$	13,920 $in.^3$
Steel, section	574.5 kg CO2e	0 kg CO2e	0 kg CO2e
Steel, wire rod	0 kg CO2e	17.2 kg CO2e	0 kg CO2e
Steel, plate	0 kg CO2e	0 kg CO2e	0 kg CO2e
Aluminum	0 kg CO2e	93.2 kg CO2e	0 kg CO2e
Timber, glulam	0 kg CO2e	74.9 kg CO2e	49.0 kg CO2e
TOTAL EC	**574.5 kg CO2e**	**185.3 kg CO2e**	**49.0 kg CO2e**

Table 31. Quantities of different gravity frame designs for a 25 ft span.

25 ft span	Steel	Beam hanger	Nuki, full section
Beam section	W10x68	5-5/8 in. x 20-1/2 in.	5 in. x 19-1/2 in.
Timber, glulam area	0 $in.^2$	115.3 $in.^2$	97.5 $in.^2$
Steel, section area	20.0 $in.^2$	0 $in.^2$	0 $in.^2$
Steel, section	6000 $in.^3$	0 $in.^3$	0 $in.^3$
Steel, wire rod	0 $in.^3$	87.0 $in.^3$	0 $in.^3$
Steel, plate	0 $in.^3$	56.3 $in.^3$	0 $in.^3$
Aluminum	0 $in.^3$	0 $in.^3$	0 $in.^3$
Timber, glulam	0 $in.^3$	34,594 $in.^3$	29,250 $in.^3$
Steel, section	1228 kg CO2e	0 kg CO2e	0 kg CO2e
Steel, wire rod	0 kg CO2e	26.1 kg CO2e	0 kg CO2e
Steel, plate	0 kg CO2e	18.3 kg CO2e	0 kg CO2e
Aluminum	0 kg CO2e	0 kg CO2e	0 kg CO2e
Timber, glulam	0 kg CO2e	121.9 kg CO2e	103.0 kg CO2e
TOTAL EC	**1228 kg CO2e**	**166.2 kg CO2e**	**103.0 kg CO2e**

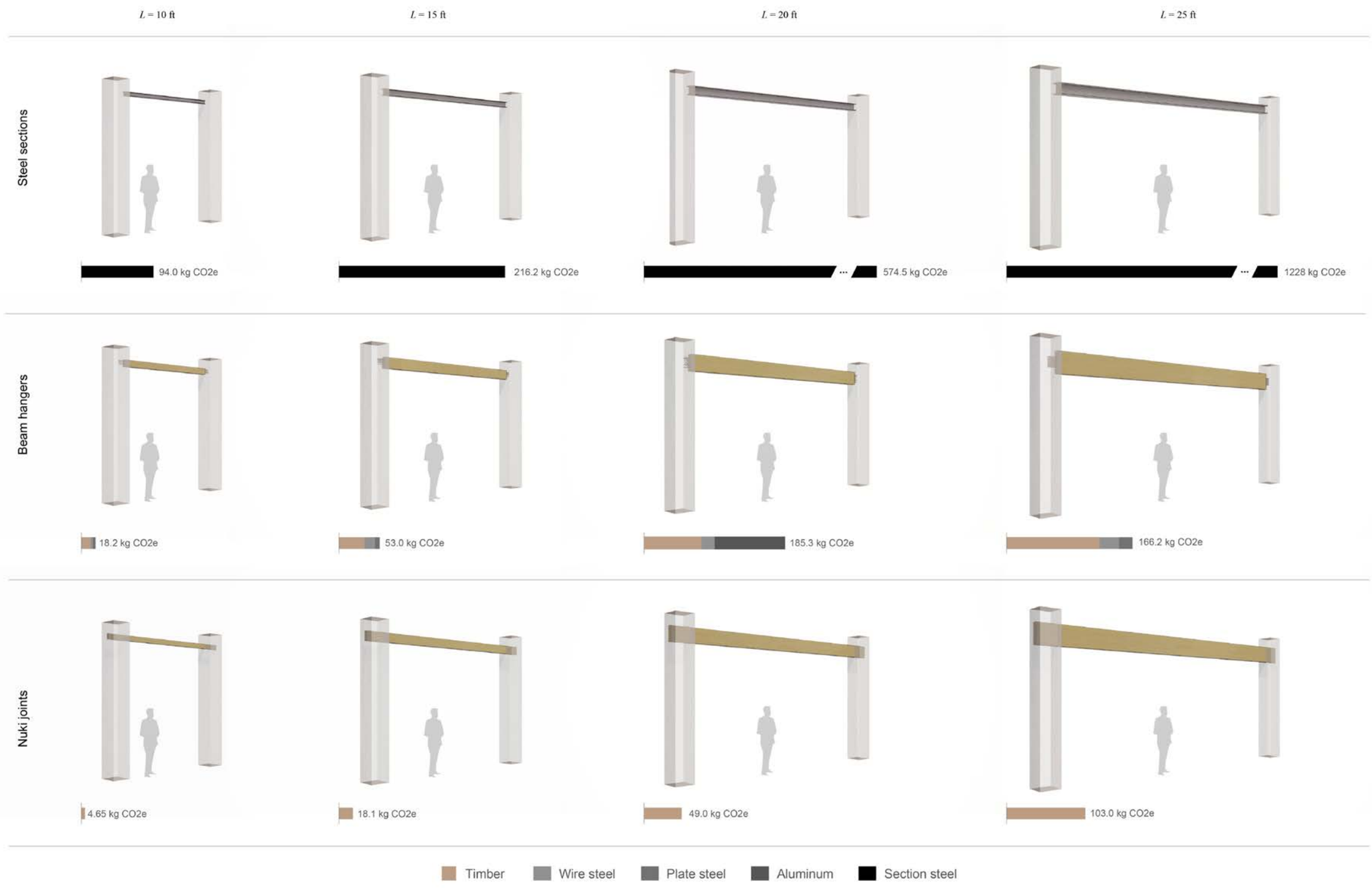

Figure 48. Embodied carbon comparison between gravity frame design methods. Embodied carbon scales for steel sections are abbreviated in order to keep scales practical for other methods. For beam hangers, only fasteners into the primary member are illustrated; fasteners into the secondary member are still included in quantities calculations and are reflected in the displayed embodied carbon quantities.

The embodied carbon values are also plotted against span in Figure 49.

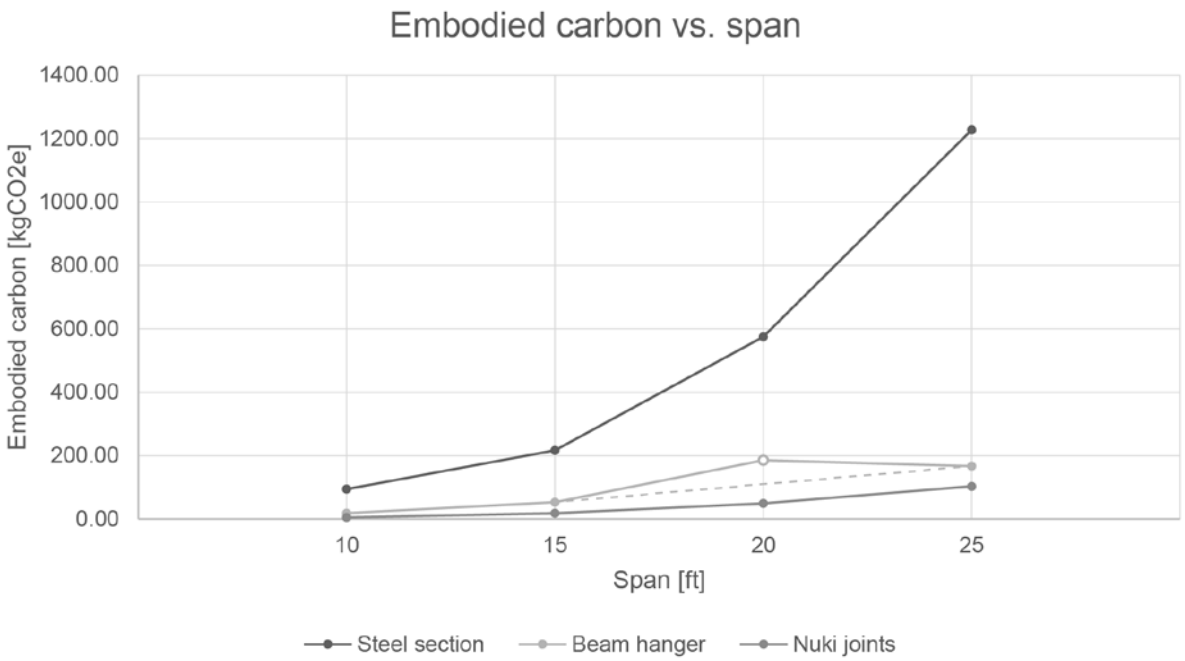

Figure 49. Embodied carbon against span for different design methods. The open dot acknowledges that a beam hanger product from a different line, the MEGANT series with more aluminum than the Ricon series, was used for the 20 ft span.

To aid with discussion, ratios between embodied carbon values from different design methods are calculated and provided in Table 32.

Table 32. Ratios between embodied carbon values for different spans and methods.

Span [ft]	EC MTC / EC Steel	EC Nuki / EC Beam hangers
10	0.19	0.26
15	0.25	0.34
20	0.32	0.26
25	0.14	0.62

5.5 Discussion: comparing quantities across frame designs

The use of timber for the beam element is indisputably an advantage from an embodied carbon perspective; comparing the steel beams to the timber beams supported by beam hangers, embodied carbon values were improved by as much as 86% in the 25 ft span scenario (Table 32). Furthermore, the rate of increase in embodied carbon when designing with steel sections appears to be much higher than for either timber system (Figure 49).

The rotational stiffness provided by the Nuki joints resulted in a reduced midspan moment (Figure 46). Given most of the beams were governed by deflection limits, a reduced midspan moment meant that the beams designed with the Nuki joints could have smaller cross-sections. Between the two connection types, the Nuki joint enabled volume reduction in timber elements through joint stiffness alone. Furthermore, the Nuki joint involves no metallic parts, meaning that it could further outcompete the beam hangers in embodied carbon quantities. These benefits added up to 38% to 74% improvement in embodied carbon quantities (Table 32).

A few assumptions were made in this comparative study that are acknowledged to influence the results. Reflections on the effects of those assumptions are provided below:

- M_{allow} of each beam section depended on the θ_y value associated with each beam section. The selection of θ_y was based on the hard limitation that it would not be tolerable for the joint to enter the plastic region. There was also no safety factor applied to the rotational stiffness k in this study (i.e. $M_{allow} = 1.0M_y$). More experimental testing to calibrate the models in Section 4 are needed to determine an appropriate safety factor. The analytical model used to design the Nuki joints were found in Section 4 to be conservative in stiffness k but unconservative in yield moment M_{allow}.
- The rotational stiffness k of each beam section provided by the Nuki joint depended on the column dimension parallel to the beam axis, C_d, which was fixed at 20 inches for all spans in this study. If C_d was set to vary linearly with span, there might be increasing end rigidity benefits at increasing spans than observed in these results. However, there is likely a practical limit on how column size varies with span. Moreover, this relationship between C_d and k is specific to the Nuki joint; other joinery geometries may not derive as much stiffness from column dimensions.
- Due to the particular geometry of the Nuki joint, the construction sequence for gravity frames using the Nuki joint may not be immediately compatible with modern methods of timber construction. However, the methods may be applied to other joinery connections whose rotational stiffnesses could be characterized in a similar way.
- Self-weight was neglected in this study. Accounting for the self-weight of the beam in the clear span would likely increase the section size needed to meet the limit states, but it is not immediately clear how it might change the comparative results between design methods.
- The tributary width was set to increase linearly with span, but the ratio of span to tributary width may depend on the flooring system.
- Embodied carbon values do not necessarily reflect time or labor costs.
- The pre-engineered beam hanger was assumed to represent a conventional fastener connection. This methodology may be repeated on other types of fastener connections.
- The scope of this LCA is cradle-to-gate.
- The effects of continuous spans and lateral loads have yet to be evaluated in detail. A preliminary assessment on the use of the Nuki joint in a lateral system with the beam and joint sizes designed in this section is illustrated in Figure 50. Drift governs and is dependent on the number of continuous spans and the number of floors. The beam designed under gravity loads was adequate for the illustrated number of bays and floors under unfactored gravity loads and wind loads while reaching only about 50% of joint moment capacity. Larger beam sizes could be used for structures with higher slenderness ratios to meet drift limits.

- The comparison does not reflect more qualitative characteristics, such as the architectural asset of creating more clear space achieved by reduced beam depth, the benefits of a non-destructive assembly, the visual continuity of a single-material system, and other opportunities mentioned in Section 1.4.

beam section: 4" x 14.5"
beam span: 20 ft
story height: 15 ft
end joint rotational stiffness: 1392 k-ft/rad
maximum drift: 4.1 in.
allowable drift (H/250): 4.3 in.
maximum joint moment: 15.6 k-ft
allowable joint moment: 34.3 k-ft

Figure 50. Preliminary assessment on the use of Nuki joints with rotational restraint for lateral systems, elevation view. 30 psf wind loads were applied as point loads assuming a 10 ft tributary width, as well as unfactored gravity loads outlined in Section 5.2. Timber columns measuring 20" x 20" were modeled.

5.6 Conclusions

The sustainability benefits of using timber over conventional carbon-intensive building materials such as steel as primary elements in structural systems are relatively well established (Section 1.4.3). However, studies seldom examine the embodied carbon implications of using the metallic fasteners conventionally used in modern timber construction in contrast to all-timber joinery connections used in more historic timber traditions.

To make these comparisons, gravity frames were designed using different beam and connection approaches for the same loading conditions across varying single spans. The quantity of embodied carbon required for each design method was compared.

As discussed in Section 2.4, two main pathways for the design of low-carbon structures are (1) reducing structural material quantities and (2) designing with materials with lower embodied

carbon (De Wolf 2017). In line with pathway (2), in this chapter, the benefit of using steel over timber as a beam element was confirmed. The strategy for introducing Nuki joints followed pathway (1) in that the added rotational stiffness allowed for a smaller cross-section of timber for those beams supported by Nuki joints. Combined with the lack of metallic fasteners in the system, the Nuki joint frames demonstrated decisive improvements in embodied carbon from the beam hangers – up to 74% improvement in some spans.

The results of this comparative study imply that joinery connections could represent a sustainable alternative to conventional metallic fastener connections used in modern timber construction. Moreover, the results indicate that structural connection quantities might represent an important consideration in evaluating the sustainability of different structural systems. The methodology of the comparative study can be repeated on other joinery geometries and other fastener connections, setting a precedent as a workflow for evaluating the sustainability of connections in structural design.

6 Conclusions

6.1 Summary of contributions

This thesis revisits the timber joinery traditions of global history through a lens of modern structural analysis. Models for the rotational stiffness of the Japanese Nuki joint, a mortise-and-tenon-type joinery, were developed based on literature (Section 3) and their results compared on varying beam widths (Section 4). All exhibited the expected bilinear stiffness behavior due to the unique properties of wood crushed perpendicular to the grain. The accuracy of absolute and relative stiffness values and yield moment across models was more difficult to verify due to limitations in experimental testing. In order to proceed with structural design using the Nuki joint, it was noted that the analytical model tended to under-predict the elastic rotational stiffness of the joint (k_1) and over-predict the moment at which the joint would yield to plastic behavior (M_y).

The analytical model was then used to design a gravity frame under loading across varying spans, representing a new contribution to literature in evaluating the effect of structural all-timber connections on sustainability in early-stage structural design (Section 5). The quantities of

material required for each gravity frame was compared to an analogous frame supported by beam hangers, a conventional structural connection in modern timber construction. The rotational stiffness provided by the Nuki joint reduces the midspan moment, enabling a smaller timber section to be selected for the beam supported by Nuki joints than for the beam supported by nominally pinned beam hangers. Combined with the absence of metallic parts in the Nuki joint, the embodied carbon savings from using Nuki joints ranged from 38% to 76%.

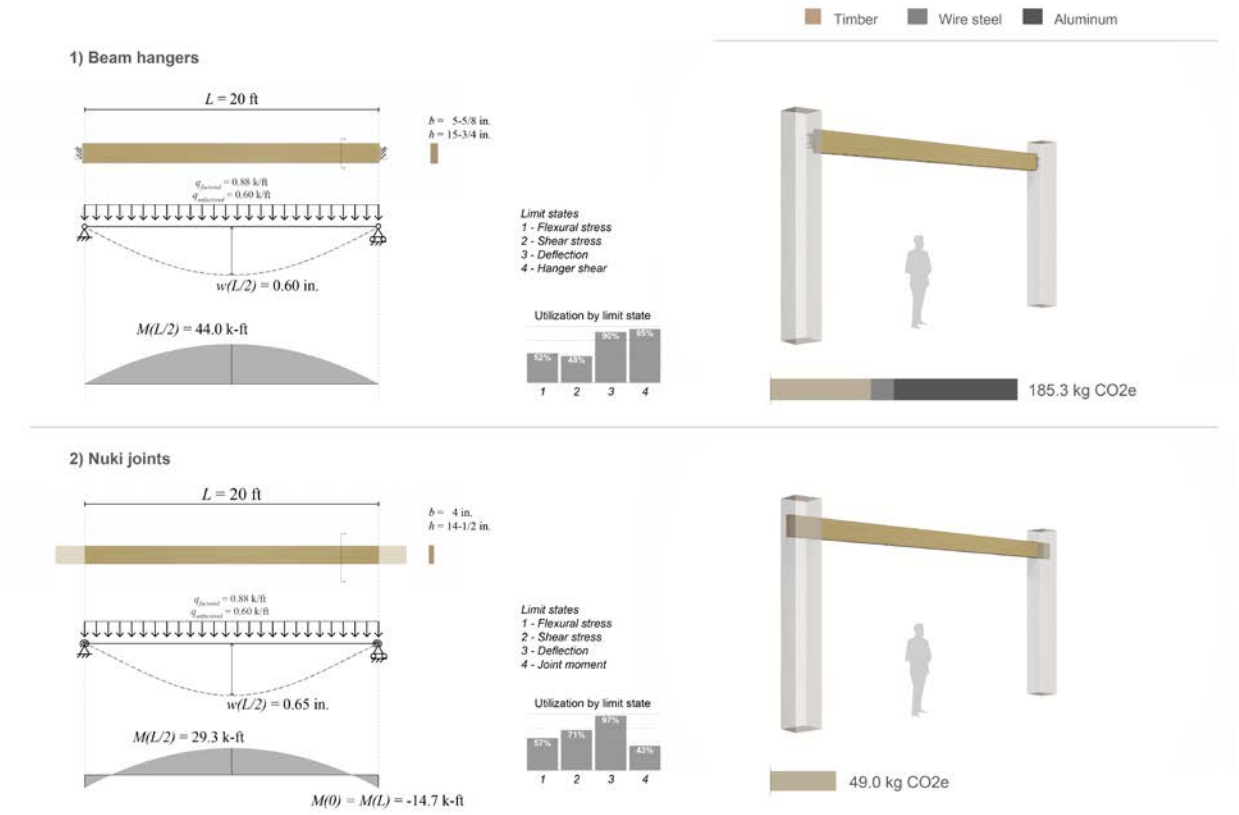

Figure 51. Summary of findings comparing the embodied carbon of a beam supported by conventional beam hangers to that of a beam supported by Nuki joints. In the 20 ft span pictured, embodied carbon savings of 76% are observed.

6.2 Potential impact

This thesis identifies joinery connections in modern timber construction as a potential opportunity for lower-carbon structures. Barriers to entry into modern timber structural systems may include the relative inaccessibility of joint characterization to structural designers, as well as an ambiguity around the benefits of selecting joinery connections over existing conventions in structural connections for timber elements. By presenting a methodology for characterizing the behavior of joinery connections and demonstrating the carbon savings achieved by selecting joinery over conventional connections, this thesis clarifies the incentives and benefits for using joinery connections in modern timber construction. If adapted at a larger scale, these applications of joinery connections have the potential to help reduce the carbon footprint of structural systems at large.

6.3 Limitations and future work

The difficulty of calibrating experimental methods with analytical and numerical methods suggests that much more experimental testing is needed due to variability in the wood (seen in both raw timber and engineered timber) and fabrication processes (seen in both hand carpentry and digital fabrication). The statistical analysis and scale of testing needed to recommend safety factors for design is beyond the scope of this thesis.

More work is also needed to apply these methods to joinery geometries that may be best adaptable by modern timber fabrication facilities. It is envisioned that a catalog of joinery connections with associated design values could be valuable for structural designers to apply these joints at a larger scale.

6.4 Concluding remarks

This thesis makes two major arguments related to timber joinery in modern timber construction: 1) timber joinery connections can be evaluated using modern engineering models for structural design, and 2) if re-introduced as structural connections, timber joinery can play a significant role in reducing the embodied carbon of structures. Along with other potential opportunities such as seismic performance, improved physiology of people inside an all-timber environment, and the longevity enabled by non-destructive assembly, it is clear that the use of timber joinery for structural connections are not to be overlooked in the current search for low-carbon strategies for structural design.

References

American Wood Council. 2017. "National Design Specification (NDS) for Wood Construction 2018 Edition." American Wood Council.

Architectural Institute of Japan (AIJ). 2010. *Fundamental Theory of Timber Engineering*. Tokyo, Japan: Maruzen.

"Architecture 2030." n.d. Accessed July 12, 2019. https://architecture2030.org/.

ASTM International. 2014. "ASTM Standard D143-14: Standard Test Methods for Small Clear Specimens of Timber." Standard. West Conshohocken, PA.

Benson, Tedd. 1997. *The Timber-Frame Home - Design, Construction, Finishing*. 2nd ed. Taunton Press.

Böhme, Luis Felipe González, Francisco Quitral Zapata, and Sandro Maino Ansaldo. 2017. "Roboticus Tignarius: Robotic Reproduction of Traditional Timber Joints for the Reconstruction of the Architectural Heritage of Valparaíso." *Construction Robotics*, July, 1–8. https://doi.org/10/gctrbq.

Brownell, Blaine. 2016. "T3 Becomes the First Modern Tall Wood Building in the U.S." Architect. November 8, 2016. https://www.architectmagazine.com/technology/t3-becomes-the-first-modern-tall-wood-building-in-the-us_o.

Browning, William, Cathering Ryan, and Joseph Clancy. 2014. "14 Patterns of Biophilic Design - Improving Health and Well-Being in the Built Environment." Terrapin Bright Green.

Brungraber, Robert Lyman. 1985. "Traditional Timber Joinery: A Modern Analysis." Stanford University. https://searchworks.stanford.edu/view/1177076.

Building Transparency. 2019. "Embodied Carbon in Construction Calculator (EC3)." October 8, 2019. https://www.buildingtransparency.org/en/.

Chang, Wen-Shao, and Min-Fu Hsu. 2007. "Rotational Performance of Traditional Nuki Joints with Gap II: The Behavior of Butted Nuki Joint and Its Comparison with Continuous Nuki Joint." *Journal of Wood Science* 53 (5): 401–7. https://doi.org/10.1007/s10086-007-0880-1.

Chang, Wen-Shao, Min-Fu Hsu, and Kohei Komatsu. 2006. "Rotational Performance of Traditional Nuki Joints with Gap I: Theory and Verification." *Journal of Wood Science* 52 (1): 58–62. https://doi.org/10.1007/s10086-005-0734-7.

Chang, Wen-Shao, Takehiro Wakita, Akihisa Kitamori, Kohei Komatsu, Yasuo Kataoka, Min-Fu Hsu, and web-support@bath.ac.uk. 2012. "Dynamic Properties of a Traditional Complex Bracket Sets in an Oriental Temple." In *World Conference on Timber Engineering 2012, WCTE 2012. Vol. 5.*, 460–63. University of Bath. http://www.conference.co.nz/wcte2012.

Chen, Jinyong, Tieying Li, Qingshan Yang, Xiwang Shi, and Yanxia Zhao. 2018. "Degradation Laws of Hysteretic Behaviour for Historical Timber Buildings Based on Pseudo-Static Tests." *Engineering Structures* 156 (February): 480–89. https://doi.org/10.1016/j.engstruct.2017.11.054.

Chen, Ling-kun, Sheng-cai Li, Yan-ting Wang, You-jun Zhao, Ming Zhang, Xing-yu Song, Xiao-wei Li, Teng Wu, and Li-zhong Jiang. 2017. "Experimental Study on the Seismic Behaviour of Mortise–Tenon Joints of the Ancient Timbers." *Structural Engineering International* 27 (4): 512–19. https://doi.org/10.2749/222137917X14881937844720.

Chen Zhiyong, Zhu Enchun, Pan Jinglong, and Wu Guofang. 2016. "Energy-Dissipation Performance of Typical Beam-Column Joints in Yingxian Wood Pagoda: Experimental Study." *Journal of Performance of Constructed Facilities* 30 (3): 04015028. https://doi.org/10.1061/(ASCE)CF.1943-5509.0000771.

CORE Studio. 2020. *Beacon*. https://core-studio.gitbook.io/beacon/.

Court, Brian. 2012. "Timber Framing at the Bullitt Center | Bullitt Center." March 19, 2012. https://bullittcenter.org/2012/03/19/timber-framing-at-the-bullitt-center/.

D'Ayala, Dina F., and Pin Hui Tsai. 2008. "Seismic Vulnerability of Historic Dieh–Dou Timber Structures in Taiwan." *Engineering Structures*, Seismic reliability, analysis, and protection of historic buildings and heritage sites, 30 (8): 2101–13. https://doi.org/10/fsrfxp.

De Wolf, Catherine Elvire Lieve. 2017. "Low Carbon Pathways for Structural Design : Embodied Life Cycle Impacts of Building Structures." Thesis, Massachusetts Institute of Technology. http://dspace.mit.edu/handle/1721.1/111491.

De Wolf, Catherine, Endrit Hoxha, Alexander Hollberg, Corentin Fivet, and John Ochsendorf. 2020. "Database of Embodied Quantity Outputs: Lowering Material Impacts Through Engineering." *Journal of Architectural Engineering* 26 (3): 04020016. https://doi.org/10.1061/(ASCE)AE.1943-5568.0000408.

Erdil, Y. Z., A. Kasal, and C. A. Eckelman. 2005. "Bending Moment Capacity of Rectangular Mortise and Tenon Furniture Joints." *Forest Products Journal* 55 (12): 209–13.

Erikson, Robert George. 2003. "Behavior of Traditional Timber Frame Structures Subjected to Lateral Load." Ph.D., United States -- Wyoming: University of Wyoming. https://search.proquest.com/pqdtglobal/docview/305285831/abstract/B8AB6DA83A9148EEPQ/1.

Fang, Demi, Julieta Moradei, Jan Brütting, Aliz Fischer, Daniel K Landez, Benshun Shao, Nick Sherrow-Groves, Corentin Fivet, and Caitlin Mueller. 2019. "Modern Timber Design Approaches for Traditional Japanese Architecture: Analytical, Experimental, and Numerical Approaches for the Nuki Joint." In *Proceedings of the International Association for Shell and Spatial Structures (IASS) Symposium*. Barcelona, Spain.

Fang, Demi, Caitlin Mueller, Jan Brütting, Corentin Fivet, and Julieta Moradei. 2019. "Rotational Stiffness in Timber Joinery Connections: Analytical and Experimental Characterizations of the Nuki Joint." In *Structures and Architecture: Bridging the Gap and Crossing Borders*, edited by Paulo J.S. Cruz, 229–36. Lisbon, Portugal: CRC Press. https://doi.org/10.1201/9781315229126-28.

Foliente, G. C. 2000. "History of Timber Construction." *ASTM International*, January. https://doi.org/10/drwj2b.

Forest Products Laboratory. 2010. "Wood Handbook: Wood as an Engineering Material." General Technical Report FPL-GTR-190. Madison, WI: U.S. Department of Agriculture, Forest Service, Forest Products Laboratory.

Fujita, Kaori, Isao Sakamoto, Yoshimitsu Ohashi, and Masahiko Kimura. 2000. "Static and Dynamic Loading Tests of Bracket Complexes Used in Traditional Timber Structures in Japan." In *Proceedings of the 12th World Conference on Earthquake Engineering*. Vol. 30. Auckland, New Zealand.

Guan, Z. W., A. Kitamori, and K. Komatsu. 2008. "Experimental Study and Finite Element Modelling of Japanese 'Nuki' Joints — Part Two: Racking Resistance Subjected to Different Wedge Configurations." *Engineering Structures* 30 (7): 2041–49. https://doi.org/10/b24n8p.

Gustavsson, Leif, Kim Pingoud, and Roger Sathre. 2006. "Carbon Dioxide Balance of Wood Substitution: Comparing Concrete- and Wood-Framed Buildings." *Mitigation and Adaptation Strategies for Global Change* 11 (3): 667–91. https://doi.org/10/fgfzcc.

Hanazato, Toshikazu, Kaori Fujita, Isao Sakamoto, Masahiro Inayama, and Yasuhiko Ohkura. 2004. "Analysis of Earthquake Resistance of Five-Storied Timber Pagoda." In . Vancouver, BC, Canada.

Hankinson, R. L. 1921. "Investigation of Crushing Strength of Spruce at Varying Angles of Grain." *Air Service Information Circular* 3 (259): 130.

Henrichsen, Christoph, and Roland Bauer. 2004. *Japan Culture of Wood: Buildings, Objects, Techniques*. 1 edition. Boston: Birkhauser.

Huixian, Liu, George W. Housner, Xie Lili, and He Duxin. 2002. "The Great Tangshan Earthquake of 1976." Report or Paper. California Institute of Technology. http://resolver.caltech.edu/CaltechEERL:EERL.2002.001.

Inayama, Masahiro. 1991. "Wooden embedment theory and its application." PhD, Tokyo, Japan: University of Tokyo.

———. 1993. "Study on compression perpendicular to the grain in wood Part 4: analytic functions for the relation between compression load and elastic deformation perpendicular to the grain in wood." In *Proceedings of AIJ*, 907–8. Tokyo.

International Energy Agency (IEA), and Global Alliance for Buildings and Construction (GlobalABC). 2018. "2018 Global Status Report: Towards a Zero-Emission, Efficient and Resilient Buildings and Construction Sector." United Nationals Environment Programme. https://www.globalabc.org/uploads/media/default/0001/01/0bf694744862cf96252d4a402e1255fb6b79225e.pdf.

Jones, Craig, and Geoffrey Hammond. 2019. "Inventory of Carbon & Energy v3.0." https://www.circularecology.com/embodied-energy-and-carbon-footprint-database.html.

Kellert, Stephen R., and Elizabeth F. Calabrese. 2015. "The Practice of Biophilic Design." London: Terrapin Bright LLC.

King, W. S., J. Y. Richard Yen, and Y. N. Alex Yen. 1996. "Joint Characteristics of Traditional Chinese Wooden Frames." *Engineering Structures* 18 (8): 635–44. https://doi.org/10.1016/0141-0296(96)00203-9.

Kitamori, A., T. Kataoka, and K. Komatsu. 2009. "Effect of Additional Length on Partial Compression Perpendicular to the Grain of Wood." *Journal of Structural and Construction Engineering* 74: 642.

Komatsu, Kohei, Akihisa Kitamori, Kiho Jung, and Takuro Mori. 2009. "Estimation of the Mechanical Properties of Mud Shear Walls Subjecting to Lateral Shear Force." In *Proceedings of the 11th International Conference on Non-Conventional Materials and Technologies*. Bath, UK.

KT Innovations, thinkstep, and Autodesk. 2019. *Tally(R) Life Cycle Assessment App*. https://choosetally.com/.

Lang, Elemer M., and Tamas Fodor. 2007. "Finite Element Analysis of Cross-Halved Joints for Structural Composites." *Wood and Fiber Science* 34 (2): 251–65.

Lenzen, M, and G Treloar. 2002. "Embodied Energy in Buildings: Wood versus Concrete—Reply to Börjesson and Gustavsson." *Energy Policy* 30 (3): 249–55. https://doi.org/10.1016/S0301-4215(01)00142-2.

Li, Xiaowei, Junhai Zhao, Guowei Ma, and Wei Chen. 2015. "Experimental Study on the Seismic Performance of a Double-Span Traditional Timber Frame." *Engineering Structures* 98 (September): 141–50. https://doi.org/10.1016/j.engstruct.2015.04.031.

Miller, Laura Marjorie. 2017. "Mass Timber: Inside the Graceful, Sustainable, and Breathtaking New Design Building." *The Magazine of the University of Massachusetts Amherst*, May 24, 2017. https://www.umass.edu/magazine/summer-2017/mass-timber.

MTC Solutions. 2020. "Beam Hanger Design Guide."

naturally:wood. 2016. "Design and Preconstruction of a Tall Wood Building, Brock Commons Phase 1: Overview."

Nordic Engineered Wood. 2013. "Nordic Lam Beams and Headers."

Ogawa, Keita, Yasutoshi Sasaki, and Mariko Yamasaki. 2015. "Theoretical Modeling and Experimental Study of Japanese 'Watari-Ago' Joints." *Journal of Wood Science* 61 (5): 481–91. https://doi.org/10/f7vdvj.

Page, Mitchell. 2017. "A Robotic Fabrication Methodology for Dovetail and Finger Jointing: An Accessible & Bespoke Digital Fabrication Process for Robotically-Milled Dovetail & Finger Joints." In *Proceedings of the 37th Annual Conference of the Association for Computer Aided Design in Architecture (ACADIA)*, 456–63. Cambridge, MA. http://papers.cumincad.org/cgi-bin/works/Show?acadia17_456.

Pomponi, Francesco, and Alice Moncaster. 2016. "Embodied Carbon Mitigation and Reduction in the Built Environment – What Does the Evidence Say?" *Journal of Environmental Management* 181 (October): 687–700. https://doi.org/10.1016/j.jenvman.2016.08.036.

Presinger, Clemens, and Bollinger+Grohmann. 2018. *Karamba* (version 1.2.2). Windows. http://www.karamba3d.com/.

Que, Ze-li, Zhe-rui Li, Xiao-lan Zhang, Zi-ye Yuan, and Biao Pan. 2017. "Traditional Wooden Buildings in China." In *Wood in Civil Engineering*, edited by Giovanna Concu. InTech. https://doi.org/10.5772/66145.

Roche, Stéphane Nicolas. 2017. "Semi-Rigid Moment-Resisting Behavior of Multiple Tab-and-Slot Joint for Freeform Timber Plate Structures." PhD, Lausanne, Switzerland: Ecole Polytechnique Federale de Lausanne. https://infoscience.epfl.ch/record/233607?ln=en.

Sathre, Roger, and Jennifer O'Connor. 2010. "Meta-Analysis of Greenhouse Gas Displacement Factors of Wood Product Substitution." *Environmental Science & Policy* 13 (2): 104–114.

Schmidt, Richard J., and Robert B. Mackay. 1997. "Timber Frame Tension Joinery." MSc thesis, Laramie, WY: University of Wyoming.

Schuchart. n.d. "The Bullitt Center." Schuchart. Accessed May 3, 2020. https://schuchart.com/project/bullitt-center-ground-up-construction-case-study/.

Sebera, Václav, and Milan Šimek. 2010. "Finite Element Analysis of Dovetail Joint Made with the Use of CNC Technology." *Acta Universitatis Agriculturae et Silviculturae Mendelianae Brunensis* 58 (5): 321–28. https://doi.org/10/gctrbt.

Shanks, Jonathan, and Peter Walker. 2009. "Strength and Stiffness of All-Timber Pegged Connections." *Journal of Materials in Civil Engineering* 21 (1): 10–18. https://doi.org/10/bg2rdf.

Shao, Benshun, Nicolette Lewis, Aliz Fischer, Yuli Huang, and Francois Lancelot. 2019. "Parameters Identification for Wood Material (*MAT_143) and Its Application on the Modeling of a Typical Timber Nuki Joint." In . Shanghai, China.

Shiping, Hu. 1991. "The Earthquake-Resistant Properties of Chinese Traditional Architecture." *Earthquake Spectra* 7 (3): 355–89. https://doi.org/10/fc5649.

Shope, Mitchell Grafton. 2016. "Strength Characterization of Wood to Wood Connections Using Stress Field Analysis." Thesis, Massachusetts Institute of Technology. http://dspace.mit.edu/handle/1721.1/104245.

Skidmore, Owings & Merrill, LLP. 2013. "Timber Tower Research Project: Initial Research Report." http://www.som.com/ideas/research/timber_tower_research_project.

Stern, Brenda G. 2018. "Minimizing Embodied Carbon in Multi-Material Structural Optimization of Planar Trusses." Thesis, Massachusetts Institute of Technology. https://dspace.mit.edu/handle/1721.1/119324.

"Structural Engineers 2050 Challenge." n.d. Carbon Leadership Forum. Accessed December 15, 2019. http://www.carbonleadershipforum.org/projects/se2050/.

Suzuki, Yoshiyuki, and Masaki Maeno. 2006. "Structural Mechanism of Traditional Wooden Frames by Dynamic and Static Tests." *Structural Control and Health Monitoring* 13 (1): 508–22. https://doi.org/10.1002/stc.153.

Takabayashi, Hiroki, Keita Kado, and Gakuhito Hirasawa. 2019. "Versatile Robotic Wood Processing Based on Analysis of Parts Processing of Japanese Traditional Wooden Buildings." In *Robotic Fabrication in Architecture, Art and Design 2018*, edited by Jan Willmann, Philippe Block, Marco Hutter, Kendra Byrne, and Tim Schork, 221–31. Springer International Publishing.

Tanabashi, Ryo. 1960. "Earthquake Resistance of Traditional Japanese Wooden Structures" 40 (December): 1–15.

Tanahashi, Hideaki, and Yoshiyuki Suzuki. 2020. "Review on the Mechanical Models and Formulations of Embedment of Traditional Timber Joints in Japan." *Japan Architectural Review* 3 (2): 148–64. https://doi.org/10.1002/2475-8876.12137.

Tannert, Thomas, Frank Lam, and Till Vallée. 2010. "Strength Prediction for Rounded Dovetail Connections Considering Size Effects." *Journal of Engineering Mechanics* 136 (3): 358–66. https://doi.org/10/fv7qpq.

"The Bed." n.d. Thuma. Accessed May 4, 2020. https://www.thuma.co/products/the-bed.

Trussoni, Matthew, Evan Simatic, Christopher H. Raebel, and H. Peter Huttelmaier. 2015. "Life-Cycle Assessment Comparison for Long-Span Cable and Truss Structural Systems: Case Study." *Journal of Architectural Engineering* 21 (1): 05014005. https://doi.org/10.1061/(ASCE)AE.1943-5568.0000154.

WoodWorks. n.d. "Promega Feynman Center, 'The Crossroads.'" WoodWorks. Accessed May 3, 2020. https://www.woodworks.org/project/promega-feynman-center-the-crossroads/.

Wu, Ya Jie, Xiao Bin Song, and Lie Luo. 2017. "Experimental Investigation on the Seismic Performance of a Chinese Traditional Wooden Pagoda." *Applied Mechanics and Materials*. https://doi.org/10.4028/www.scientific.net/AMM.858.119.

Wu, Yajie, Xiaobin Song, Xianglin Gu, and Lie Luo. 2018. "Dynamic Performance of a Multi-Story Traditional Timber Pagoda." *Engineering Structures* 159 (March): 277–85. https://doi.org/10.1016/j.engstruct.2018.01.003.

Wu, Yajie, Xiaobin Song, and Kai Li. 2018. "Compressive and Racking Performance of Eccentrically Aligned Dou-Gong Connections." *Engineering Structures* 175 (November): 743–52. https://doi.org/10.1016/j.engstruct.2018.08.054.

Wu, Yajie, Xiaobin Song, and Carlos E. Ventura. 2019. "Modal Properties of a Model of a Chinese Pagoda." In *Dynamics of Civil Structures, Volume 2*, edited by Shamim Pakzad, 359–65. Conference Proceedings of the Society for Experimental Mechanics Series. Springer International Publishing.

Xie, Qifang, Long Wang, Lipeng Zhang, Weibing Hu, and Tiegang Zhou. 2018. "Seismic Behaviour of a Traditional Timber Structure: Shaking Table Tests, Energy Dissipation Mechanism and Damage Assessment Model." *Bulletin of Earthquake Engineering*, October. https://doi.org/10.1007/s10518-018-0496-4.

Xue, Jianyang, Dan Xu, and Hailun Xia. 2018. "Experimental Study on Seismic Performance of Through-Tenon Joints with Looseness in Ancient Timber Structures." *International Journal of Architectural Heritage* 0 (0): 1–13. https://doi.org/10.1080/15583058.2018.1552996.

Yeo, Sok Yee, Min-Fu Hsu, Kohei Komatsu, Yu-Lin Chung, and Wen-Shao Chang. 2016. "Shaking Table Test of the Taiwanese Traditional Dieh-Dou Timber Frame." *International Journal of Architectural Heritage* 10 (5): 539–57. https://doi.org/10/gctq94.

Yeo, Sok-Yee, Kohei Komatsu, Min-Fu Hsu, and Zeli Que. 2016. "Mechanical Model for Complex Brackets System of the Taiwanese Traditional Dieh-Dou Timber Structures." *Advances in Structural Engineering* 19 (1): 65–85. https://doi.org/10/f8chfd.

Zwerger, Klaus. 2015. *Wood and Wood Joints*. 3rd ed. edition. Basel ; Boston: Birkhäuser.

Appendix 1: Analytical models for the Nuki joint

The code provided below was used to construct analytical models to match the Douglas fir prototypes using the Maple symbolic computing environment. The code is the same for the glulam prototypes but with different input parameters as detailed in Table 5. This code was further developed by the author but primarily originated from collaborator Jan Brütting.

Part 1: Set up parameters and definitions

Note: some input parameters vary between the Douglas fir and glulam prototypes. Check Table 4 and Table 5 for respective parameters.

Input code	Output
restart:	
E__0 := 1.57e6; #psi	$E_0 := 1.57 \times 10^6$
E__90 := 0.9 * 40550; #psi	$E_{90} := 36495.0$
yield_strain := 0.018;	$yield\_strain := 0.018$

mue := 0.2;	$mue := 0.2$
`R := 0.07;` # reduction in stiffness from elastic to plastic	$R := 0.07$
Cw := 3.25; #inches	$Cw := 3.25$
Cd := 3.25; #inches	$Cd := 3.25$
Bd := 3.25; #inches	$Bd := 3.25$

#l__e is the length of the short free end, which is 1" in all of our prototypes ; l__c is the length of the long end and in literature is taken as 1.5*Bd. The decay works across these lengths.
l__e := 1;
l__c := 1.5*Bd;
	$l_e := 1$
	$l_c := 4.875$

`L := (Cd/2)/cos(theta);` #length of beam that gets compressed (distance to neutral axis)	$L := \frac{1.625}{\cos(\theta)}$
delta := sin(theta)*L; #peak embedment length	$\delta := \frac{1.625\sin(\theta)}{\cos(\theta)}$
Z__theta := Bd*cos(theta); #new compressed beam depth	$Z_{theta} := 3.25\cos(\theta)$
strain := delta / Bd;	$strain := \frac{0.5\sin(\theta)}{\cos(\theta)}$
`delta_yield := yield_strain * Bd;` #delta at which the material yields (inches) theta_yield := arctan(delta_yield / (Cd/2)); #theta at which the material yields (radians)	$delta\_yield := 0.05850$ $theta\_yield := 0.03598446008$
#Hankinson's formula E__theta := E__0*E__90/(E__0*(sin(3.1415927/2-theta))^2 + E__90*(cos(3.1415927/2-theta))^2):	

Part 2: Calculate moment as a function of rotational displacement

This portion of code can be applied based on the input parameters defined in the previous segment of code.

Input code	Related equation in Section 3.2
#Embedments	
#decay coefficients decay__e := 6.5/Bd: decay__c := 6.5/Bd:	
#Ended embedment (short end) f__e := delta*exp(-decay__e*x):	(11)
#Continuous embedment (long end) f__c := delta*exp(-decay__c*x):	(11)
#ELASTIC Range	
#compute areas V1 := 0.5 * Cd/2 * delta:	(12)
Ve1 := int(f__e, x=0..l__e):	(13)
Vc1 := int(f__c, x=0..l__c):	(14)
#compute corresponding moment arms a1 := 2/3 * Cd/2:	(19)
`ae1 := Cd/2 + int(x*f__e, x=0..l__e)/Ve1:` #use integration to find centroid location for moment arm	(20)
ac1 := Cd/2 + int(x*f__c, x=0..l__c)/Vc1:	(21)
#compute resultant forces	

#N = volume * stiffness / shortened beam depth	
Ne1 := (Bw * Ve1) * E__theta / Z__theta:	(16)
Nc1 := (Bw * Vc1) * E__theta / Z__theta:	(17)
N1 := (Bw * V1) * E__theta / Z__theta:	(18)
M_el := 2*N1*a1 + Ne1*ae1 + Nc1*ac1:	(51)
`M_el := M_el + mue * N1 * Bd:` # the extended length embedments (exponential curves) do not contribute to friction	(48)(49)(51)
#PLASTIC Range delta_plastic := delta - delta_yield: #Embedment from direct contact Lp := Cd/2*(1 - delta_yield/delta):	(22)
#compute areas V2 := 0.5 * delta_yield * (Cd/2 - Lp):	(24)
V3 := delta_yield * Lp:	(25)
V4 := 0.5 * delta_plastic * Lp:	(26)
#compute corresponding moment arms a2 := (2/3)*(Cd/2 - Lp):	(39)
a3 := Cd/2 - Lp/2:	(40)
a4 := Cd/2 - Lp/3:	(41)
#compute resultant forces #N = volume * stiffness / shortened beam depth	
N2 := (Bw * V2) * E__theta / Z__theta:	(33)
N3 := (Bw * V3) * E__theta / Z__theta:	(33)
N4 := (Bw * V4) * E__theta / Z__theta:	(34)

M_dir_p := 2 * (N2*a2 + N3*a3 + R*N4*a4):	Part of (52)
M_dir_p := M_dir_p + mue*(N2 + N3 + N4)*Bd:	(48)(49)
#Embedment from indirect contact	
`Lpe := min(solve(f__e - delta_yield = 0, x), l__e):` # horizontal distances at which embedment stress = yield stress	(23)
Lpc := min(solve(f__c - delta_yield = 0, x), l__c):	(23)
#End side	
#compute areas	
Ve2 := Lpe * delta_yield:	(27)
Ve3 := int(f__e, x=Lpe..l__e):	(28)
Ve4 := int(f__e - delta_yield, x=0..Lpe):	(29)
#compute corresponding moment arms	
ae2 := Cd/2 + Lpe/2:	(42)
`ae3 := Cd/2 + int(x*f__e, x=Lpe..l__e)/Ve3:` #use integration to find centroid location for moment arm	(43)
ae4 := Cd/2 + int(x*(f__e - delta_yield), x=0..Lpe)/Ve4:	(44)
#Continuous side	
#compute areas	
Vc2 := Lpc * delta_yield:	(30)
Vc3 := int(f__c, x=Lpc..l__c):	(31)
Vc4 := int(f__c - delta_yield, x=0..Lpc):	(32)
#compute corresponding moment arms	
ac2 := Cd/2 + Lpc/2:	(45)
`ac3 := Cd/2 + int(x*f__c, x=Lpc..l__c)/Vc3:` #use integration to find centroid location for moment arm	(46)

ac4 := Cd/2 + int(x*(f__c - delta_yield), x=0..Lpc)/Vc4:	(47)
#compute resultant forces	
Ne2 := (Bw* Ve2) * E__theta / Z__theta:	(35)
Ne3 := (Bw* Ve3) * E__theta / Z__theta:	(35)
Ne4 := (Bw* Ve4) * E__theta / Z__theta:	(36)
Nc2 := (Bw* Vc2) * E__theta / Z__theta:	(37)
Nc3 := (Bw* Vc3) * E__theta / Z__theta:	(37)
Nc4 := (Bw* Vc4) * E__theta / Z__theta:	(38)
M_embed_plastic := Ne2*ae2 + Ne3*ae3 + R*Ne4*ae4 + Nc2*ac2 + Nc3*ac3 + R*Nc4*ac4: #friction effects do not apply for indirect embedment	Part of (52)
M_pl := M_dir_p + M_embed_plastic:	(52)
#compute rotational stiffnesses pd_el := diff(M_el, theta): pd_pl := diff(M_pl, theta):	

Part 3: Assemble M as a function of theta for some range of theta

This example code inputs a beam width B_w of 1", which can be substituted with 1.5" for the other beam width.

with(ArrayTools):	
M1 := Array([0]): rot1 := Array([0]): diff1 := Array([0]):	
#specify beam width Bw := 1; #inches	$Bw := 1$
#populate arrays of M and theta for a specified range of theta for theta from 0.01 by 0.01 to 0.2 do	

if delta <= delta_yield
then
Append(M1,M_el);
Append(rot1,theta);
Append(diff1,pd_el);
else
Append(M1,M_pl);
Append(rot1,theta);
Append(diff1,pd_pl);
end if;
end do:	

#compute elastic stiffness theta :=theta_yield/2: pd_el; #compute plastic stiffness theta := theta_yield*3: pd_pl;	76808.77400 25383.41518

Appendix 2: Scans of tested prototypes

Douglas fir prototypes

This section includes scans of the beam elements of the Douglas fir prototypes after rotational stiffness testing. The scans are oriented such that the ended end is at the top and the continuous end at the bottom. Embedment is visible on the left and right edges.

Figure 52. Specimen 1 of the Douglas fir Nuki joint of B_w = 1", scanned after rotational stiffness testing.

Figure 53. Specimen 2 of the Douglas fir Nuki joint of B_w = 1", scanned after rotational stiffness testing.

Figure 54. Specimen 3 of the Douglas fir Nuki joint of B_w = 1", scanned after rotational stiffness testing.

Figure 55. Specimen 1 of the Douglas fir Nuki joint of B_w = 1.5", scanned after rotational stiffness testing.

Figure 56. Specimen 2 of the Douglas fir Nuki joint of B_w = 1.5", scanned after rotational stiffness testing.

Figure 57. Specimen 3 of the Douglas fir Nuki joint of B_w = 1.5", scanned after rotational stiffness testing.

Glulam prototypes

This section includes scans of the beam elements of some of the glulam prototypes after rotational stiffness testing. Not all are shown because not all of the prototypes could be disassembled by hand, but none of those depicted here were discarded as outliers in Section 4.3.2. The scans are oriented such that the ended end is at the top and the continuous end at the bottom. Embedment is visible on the left and right edges.

Figure 58. Specimen 5 of the glulam Nuki joint of B_w = 1", scanned after rotational stiffness testing.

Figure 59. Specimen 6 of the glulam Nuki joint of B_w = 1", scanned after rotational stiffness testing.

Figure 60. Specimen 2 of the glulam Nuki joint of B_w = 1.5", scanned after rotational stiffness testing.

Appendix 3: Beam with partially rotational restrained supports

This section will show the derivation of an indeterminate beam supported on both ends with a support of a known partial rotational stiffness (intermediate between pin of 0 rotational stiffness and a fixed support of infinite rotational stiffness; see Figure 61). The aim is to determine the moment reactions at either end of the beam given the partial rotational stiffness at each support. The moment distribution and deflected shape follow.

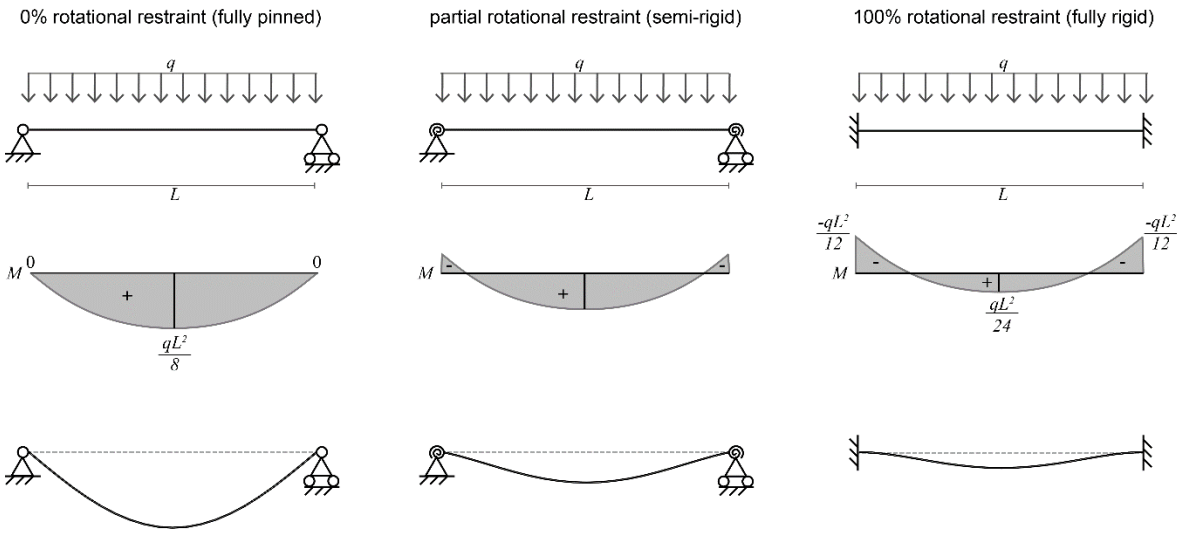

Figure 61. Comparison of uniformly loaded beam with varying boundary conditions.

Suppose a beam of length L experiences a uniformly distributed load of q. At each end is a support that provides upwards restraint and partial rotational stiffness of k (in units of moment per radians) in the elastic region.

Due to symmetry, the vertical reaction forces are each known to equal $\frac{qL}{2}$. The moment reactions at each support of magnitude M_R are also known to be equivalent, i.e. $-M_R = M(0) = M(L)$, but are still unknown. The free body diagram and internal force distributions are illustrated in Figure 62.

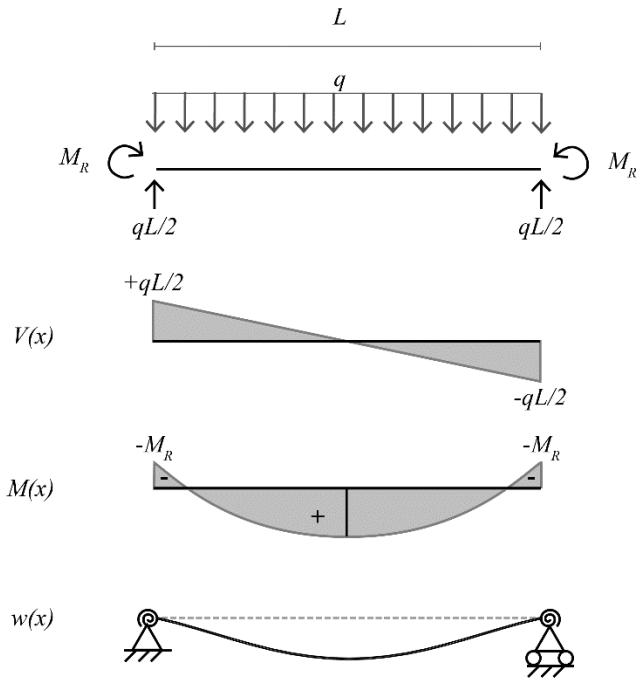

Figure 62. Free body diagram, shear V(x), moment M(x), and deflection w(x) diagrams for the beam supported with partial rotational restraint.

Let x represent the axis along the centroid of the beam. The internal shear within the beam $V(x)$ can be expressed as follows:

$$V(x) = \frac{qL}{2} - qx \tag{65}$$

It follows that the internal bending moment within the beam $M(x)$ is:

$$M(x) = \int V(x)dx = -M_R + \frac{qL}{2}x - \frac{q}{2}x^2 \tag{66}$$

To use differential equations to solve for the beams, boundary conditions must first be stated. Let $w(x)$ represent the deflection of the beam perpendicular to its axis (positive upwards), and $\varphi(x) = w'(x)$ represent the angle of deflection. The following boundary conditions arise out of the supports and out of symmetry:

$$w(0) = w(L) = 0 \tag{67}$$

$$w'(0) = w'(L) = -\frac{M_R}{k} \tag{68}$$

$$w'\left(\frac{L}{2}\right) = 0 \tag{69}$$

Assuming Euler-Bernoulli beam theory applies, we can set the expression for $M(x)$ equal to $EIw''(x)$:

$$EIw''(x) = -M_R + \frac{qL}{2}x - \frac{q}{2}x^2 \tag{70}$$

$$EIw'(x) = C - M_R x + \frac{qL}{4}x^2 - \frac{q}{6}x^3 \tag{71}$$

The two boundary conditions (68) and (69) can be substituted into (71) to solve for both the integration constant C and the reaction moment M_R.

$$EIw'(0) = -EI\frac{M_R}{k} = C \tag{72}$$

$$EIw'\left(\frac{L}{2}\right) = 0 = C - \frac{M_R L}{2} + \frac{qL}{4}\left(\frac{L}{2}\right)^2 - \frac{q}{6}\left(\frac{L}{2}\right)^3 \tag{73}$$

$$C = -EI\frac{M_R}{k} = \frac{M_R L}{2} - \frac{qL^3}{16} + \frac{qL^3}{48} = \frac{M_R L}{2} - \frac{qL^3}{24} \tag{74}$$

$$M_R\left(-\frac{EI}{k} - \frac{L}{2}\right) = -\frac{qL^3}{24}$$

$$M_R = \frac{qL^3}{24\left(\frac{EI}{k} + \frac{L}{2}\right)} \tag{75}$$

The expression for M_R in equation (75) is used in Section 5.3.3 to determine the moment distribution of a beam supported on both ends with a joint of known rotational stiffness k.

Another value of interest is the maximum deflection in the beam. Due to the symmetric nature of the loading and support conditions, the maximum deflection is known to occur at midspan. The value of $w\left(\frac{L}{2}\right)$ is thus the maximum deflection of interest. We can integrate equation (71), apply boundary conditions from equation (67), and substitute integration constant C from equation (74) to find $w(x)$:

$$EIw(x) = C_0 + Cx - \frac{M_R}{2}x^2 + \frac{qL}{12}x^3 - \frac{q}{24}x^4$$

$$EIw(0) = 0 = C_0$$

$$EIw(x) = Cx - \frac{M_R}{2}x^2 + \frac{qL}{12}x^3 - \frac{q}{24}x^4$$

$$EIw(x) = -EI\frac{M_R}{k}x - \frac{M_R}{2}x^2 + \frac{qL}{12}x^3 - \frac{q}{24}x^4$$

$$w(x) = \frac{1}{EI}\left(-EI\frac{M_R}{k}x - \frac{M_R}{2}x^2 + \frac{qL}{12}x^3 - \frac{q}{24}x^4\right) \tag{76}$$

where M_R is given by equation (75).

Finally, we can find midspan deflection:

$$w\left(\frac{L}{2}\right) = \frac{1}{EI}\left(-EI\frac{M_R}{k}\frac{L}{2} - \frac{M_R}{2}\frac{L^2}{4} + \frac{qL}{12}\frac{L^3}{8} - \frac{q}{24}\frac{L^4}{16}\right)$$

$$w\left(\frac{L}{2}\right) = \frac{L}{EI}\left(-EI\frac{M_R}{2k} - \frac{M_R L}{8} + \frac{qL^3}{128}\right) \tag{77}$$

where M_R is given by equation (75).

Appendix 4: Beam hanger volume estimates

In this section, details for selecting and calculating quantities for beam hanger products used in Section 5 are provided. The final volume quantities calculated in this appendix are used in Table 28, Table 29, Table 30, and Table 31.

Ricon S VS 140x60

The 10 ft span required a shear capacity of at least 2.2 k. Assuming SPF glulam, to provide a shear capacity of 2.44 k, a single Ricon S VS 140x60 beam hanger was used with 7 fasteners on the primary member and 7 fasteners on the secondary member. The volume calculation of this beam hanger design is presented in Table 33 and is input into the total quantities of the 10 ft span supported by beam hangers (Table 28).

Table 33. Quantities calculation for a Ricon S VS 140x60 beam hanger.

	Connector plate*		Fastener: VG CSK 5/16″ x 3-1/8″		Fastener: VG CSK 5/16″ x 6-1/4″		
	w	2-3/8 in.	d_{thread}	5/16 in.	d_{thread}	5/16 in.	
	h	5-1/2 in.	d_{head}	5/8 in.	d_{head}	5/8 in.	
	t	3/16 in.	L_{thread}	2-1/2 in.	L_{thread}	5-5/8 in.	
			L	3-1/8 in.	L	6-1/4 in.	
Volume steel plate	2.45 in.^{3}		0 in.^{3}		0 in.^{3}		
Volume steel wire rod**	0 in.^{3}		0.256 in.^{3}		0.495 in.^{3}		
Qty per connector	2		7		7		
Qty connectors per beam	2		2		2		
Total volume steel plate per beam	9.8 in.^{3}		0 in.^{3}		0 in.^{3}		9.8 in.^{3}
Total volume steel wire rod per beam	0 in.^{3}		3.58 in.^{3}		6.93 in.^{3}		10.5 in.^{3}

*Cutouts, fillets, and knob are approximated to cancel each other out and are omitted from volume calculation.

**Volume of fasteners estimated as $\pi \left(\frac{d_{thread}}{2}\right)^2 L_{thread} + \frac{1}{3}\pi \left(\frac{d_{head}}{2}\right)^2 (L - L_{thread})$.

Ricon S VS 200x80

The 15 ft span required a shear capacity of at least 4.95 k. Assuming SPF glulam, to provide a shear capacity of 6.89 k, a single Ricon S VS 200x80 beam hanger was used with 16 fasteners on the primary member and 16 fasteners on the secondary member. The volume calculation of this beam hanger design is presented in Table 34 and is input into the total quantities of the 15 ft span supported by beam hangers (Table 29).

Table 34. Quantities calculation for a Ricon S VS 200x80 beam hanger.

	Connector plate*		Fastener: VG CSK 3/8″ x 4″		Fastener: VG CSK 3/8″ x 7-7/8″		
	w	3-1/8 in.	d_{thread}	3/8 in.	d_{thread}	3/8 in.	
	h	7-7/8 in.	d_{head}	3/4 in.	d_{head}	3/4 in.	
	t	3/16 in.	L_{thread}	2-1/2 in.	L_{thread}	5-5/8 in.	
			L	4 in.	L	7-7/8 in.	
Volume steel plate	4.61 in.^{3}		0 in.^{3}		0 in.^{3}		
Volume steel wire rod**	0 in.^{3}		0.497 in.^{3}		0.953 in.^{3}		
Qty per connector	2		16		16		
Qty connectors per beam	2		2		2		
Total volume steel plate per beam	18.5 in.^{3}		0 in.^{3}		0 in.^{3}		18.5 in.^{3}
Total volume steel wire rod per beam	0 in.^{3}		15.9 in.^{3}		30.5 in.^{3}		46.4 in.^{3}

*Cutouts, fillets, and knob are approximated to cancel each other out and are omitted from volume calculation.

**Volume of fasteners estimated as $\pi \left(\frac{d_{thread}}{2}\right)^2 L_{thread} + \frac{1}{3}\pi \left(\frac{d_{head}}{2}\right)^2 (L - L_{thread})$

MEGANT 310x100

The 20 ft span required a shear capacity of at least 8.80 k. Assuming SPF glulam, to provide a shear capacity of 9.28 k, a MEGANT 310x100 beam hanger was used with 34 fasteners.

Compared to the Ricon S VS line, the MEGANT line has several more components. Aluminum components and steel wire rod components are separated out into Table 35 and Table 36, respectively. Hex nuts and washers were omitted from volume calculations. The final quantities are input into the total quantities of the 20 ft span supported by beam hangers (Table 30).

Table 35. Aluminum quantities calculation for a MEGANT 310x100 beam hanger.

	Connector plate*		Clamping jaws**		
	w	4 in.	w_j	4 in.	
	w_2	7/8 in.	h_j	2 in.	
	h_3	9-7/8 in.	t_j	1-9/16 in.	
	h_{offset}	3/4 in.	$h_{j,groove}$	3/4 in.	
	t	1/2 in.	$t_{j,groove}$	1 in.	
Volume aluminum per component		30.74 in.^{3}		9.50 in.^{3}	
Qty per connector		2		2	
Qty connectors per beam		2		2	
Total volume aluminum per beam		123.0 in.^{3}		38.0 in.^{3}	161.0 in.^{3}

*Volume approximated as $h_3wt + (h_3 - 2h_{offset})(3w_2)t$. Holes for fasteners omitted from calculation.

**Volume approximated as $h_j w_j t_j - h_{j,groove} w_j t_{j,groove}$.

Table 36. Steel wire rod quantities calculation for a MEGANT 310x100 beam hanger.

	Threaded rods		Fastener: VG CSK 5/16" x 6-1/4" *		
	d	3/4 in.	d_{thread}	5/16 in.	
	L	9-7/8 in.	d_{head}	5/8 in.	
			L_{thread}	5-5/8 in.	
			L	6-1/4 in.	
Volume steel wire rod per component		5.91 in.^{3}		0.495 in.^{3}	
Qty per connector		2		34	
Qty connectors per beam		2		2	
Total volume steel wire rod per beam		23.6 in.^{3}		33.7 in.^{3}	57.3 in.^{3}

*Volume of fasteners estimated as $\pi \left(\frac{d_{thread}}{2}\right)^2 L_{thread} + \frac{1}{3}\pi \left(\frac{d_{head}}{2}\right)^2 (L - L_{thread})$.

Ricon XL 390x80

The 25 ft span required a shear capacity of at least 13.75 k. Assuming SPF glulam, to provide a shear capacity of 15.5 k, a single Ricon XL 390x80 beam hanger was used with 30 fasteners on the primary member and 30 fasteners on the secondary member. The volume calculation of this beam hanger design is presented in Table 37 and is input into the total quantities of the 25 ft span supported by beam hangers (Table 31).

Table 37. Quantities calculation for a Ricon XL 390x80 beam hanger.

	Connector plate + block*		Fastener: VG CSK 3/8" x 4"		Fastener: VG CSK 3/8" x 7-7/8"		
	w	3-1/8 in.	d_{thread}	3/8 in.	d_{thread}	3/8 in.	
	h	13-3/8 in.	d_{head}	3/4 in.	d_{head}	3/4 in.	
	t	3/16 in.	L_{thread}	2-1/2 in.	L_{thread}	5-5/8 in.	
	w_{block}	3-1/8 in.	L	4 in.	L	7-7/8 in.	
	h_{block}	2 in.					
	t_{block}	1 in.					
Volume steel plate		14.09 in.^{3}		0 in.^{3}		0 in.^{3}	
Volume steel wire rod**		0 in.^{3}		0.497 in.^{3}		0.953 in.^{3}	
Qty per connector		2		30		30	
Qty connectors per beam		2		2		2	
Total volume steel plate per beam		56.3 in.^{3}		0 in.^{3}		0 in.^{3}	56.3 in.^{3}
Total volume steel wire rod per beam		0 in.^{3}		29.8 in.^{3}		57.2 in.^{3}	87.0 in.^{3}

*Cutouts, fillets, and knob are approximated to cancel each other out and are omitted from volume calculation. Volume of unit estimated as $wht + w_{block}h_{block}t_{block}$.

**Volume of fasteners estimated as $\pi\left(\frac{d_{thread}}{2}\right)^2 L_{thread} + \frac{1}{3}\pi\left(\frac{d_{head}}{2}\right)^2 (L - L_{thread})$